Hunting for the chiral magnetic effect

Jagd nach dem chiral magnetischen Effekt

Master-Thesis von Frédéric Kornas

April 2017

TECHNISCHE UNIVERSITÄT DARMSTADT

Fachbereich Physik
GSI Helmholtzzentrum für Schwerionenforschung GmbH
HADES collaboration

Hunting for the chiral magnetic effect
Jagd nach dem chiral magnetischen Effekt

Vorgelegte Master-Thesis von Frédéric Kornas

1. Gutachten: JProf. Dr. Tetyana Galatyuk
2. Gutachten: Dr. Ilya Selyuzhenkov

Tag der Einreichung:

Erklärung zur Master-Thesis

Hiermit versichere ich, die vorliegende Master-Thesis ohne Hilfe Dritter nur mit den angegebenen Quellen und Hilfsmitteln angefertigt zu haben. Alle Stellen, die aus Quellen entnommen wurden, sind als solche kenntlich gemacht. Diese Arbeit hat in gleicher oder ähnlicher Form noch keiner Prüfungsbehörde vorgelegen.

Darmstadt, den 5.04.2016

(Frédéric Kornas)

Abstract

In the hot and densed matter created in heavy-ion collisions the formation of parity-odd bubbles is expected. The topology of the QCD vacuum should manifest itself in the change in the chirality of the fermions. Due to the large amount of positive charge passing by the fireball there are very strong magnetic fields produced reaching values of about $B_{\mathrm{max}} \sim 10^{14}$ T. In the collision region the magnetic field is approximately homogeneous and due to its strength all particle spins are aligned in the direction of the magnetic field depending on the particle charge. A change in the chirality could therefore only occur by flipping the particle momentum. This would lead to a charge separation along the magnetic field. Since any parity-odd observable vanishes when averaged over many events, two-particle correlations are proposed as a quantity to measure a possible charge separation since they are parity-even.

The two-particle correlations have been measured with HADES. The analysis is based on the data recorded in April 2012 where Au+Au collisions at a center-of-mass energy of $\sqrt{s_{NN}} = 2.42$ GeV have been performed. $7.3 \cdot 10^9$ events corresponding to 140 TByte of data have been collected in a centrality range from $0-47\,\%$ of the total cross section. Since one of the drift chambers was not operating well during the whole beamtime, only 1/30 th of the statistic is analyzed where all six sectors were available.

The events have been selected according to a set of quality criterias. To identify the different particle types a procedure based on the measured time-of-flight and the specific energy loss is performed. On top of this, a $2\,\sigma$ cut in the β versus momentum distributions is applied resulting in a high purity of the sample. Protons and pions (both π^+ and π^-) are used in this analysis.

The analysis of azimuthal distributions require the translation of the azimuthal angle into the reaction plane frame. This frame is defined by the beam axis and the impact parameter of the collision. The event plane angle (as an estimation of the reaction plane angle) is reconstructed by the Forward Hodoscope Wall using primarily spectator particles. This allows to avoid autocorrelations. Then the particle flow, but also the two-particle correlations, are reconstructed with respect to the event plane. To account for the finite particle multiplicities, the data are corrected for the event plane resolution.

To remove possible contribution due to an asymmetry of the directed flow of these particles, the data are corrected for efficiency. The efficiency correction is based on data and accounts for the efficiency loss if the track density is high. Applying this correction the symmetry around midrapidity is recovered but only within a specific transverse momentum window: $p_t > 600$ MeV/c for protons and $150 < p_t < 600$ MeV/c for pions. The two-particle correlations are studied within this specific windows but also in the whole phase space. Various contributions from detector effects are considered. To further study the origin of possible background sources the mixed-event method has been used to estimate the background in a systematic way. Additionally, Monte-Carlo simulations using the UrQMD transport model have been performed.

Zusammenfassung

In der heißen und komprimierten Phase, die in Schwerionenkollisionen entsteht, wird die Entstehung von Regionen ungerader Parität vorausgesagt. Durch die Wechselwirkung der zugrundeliegenden Topologie des QCD Vakuums mit den Fermionen der heißen Phase soll eine Chiralitätsänderung einhergehen. Wegen der hohen Anzahl an positiven Ladungen der kollidierenden Schwerionen entstehen extrem starke Magnetfelder mit Feldstärken bis zu $B_{\mathrm{max}} \sim 10^{14}$ T. Das Magnetfeld im Inneren des Feuerballs ist nahezu homogen was verbunden mit der enormen Stärke dazu führt, dass sich die Teilchenspins entlang des Magnetfeldes ausrichten. Ob parallel oder antiparallel hängt dabei von der Ladung der Fermionen ab. Daher kann eine Chiralitätsänderung nur vonstatten gehen, wenn sich der Teilchenimpuls umkehrt, was im Endeffekt in einer Ladungsaufteilung entlang des Magnetfeldes resultiert.
Mögliche Observablen, um solch einen Effekt zu messen, müssen eine gerade Parität aufweisen, weil sie sonst einen Erwartungswert von Null haben, wenn über viele Kollisionen gemittelt wird. Daher reichen Einteilchenverteilungen nicht aus und es müssen Zweiteilchenkorrelationen betrachtet werden.
Diese wurden mit HADES gemessen. Die Analyse basiert auf den im April 2012 in Gold+Gold Kollisionen aufgenommenen Daten bei einer Kollisionsenergie im Schwerpunktsystem von $\sqrt{s_{NN}} = 2.42$ GeV. Insgesamt wurden $7.3 \cdot 10^9$ Events in einem Zentralitätsbereich von $0-47\,\%$ des totalen Wirkungsquerschnitts aufgenommen, was einer Datenmenge von 140 TBytes entspricht. In die Analyse geht lediglich 1/30 tel der Daten ein, da eine der Driftkammern zur Spurrekonstruktion nicht über die gesamte Beamzeit einwandtfrei operierte.
Die Selektion der Events wurde nach den standardmäßigen Qualitätskriterien durchgeführt. Die Teilchenidentifikation erfolgte anschließend mittels der gemessenen Flugzeit sowie dem Energieverlust der Teilchen. Zudem wurde ein $2\,\sigma$ Schnitt anhand der β-Impuls-Verteilung gemacht, um eine möglichst reine Teilchensammlung zu erhalten. Auf diese Weise wurden Protonen und Pionen beider Ladungszustände identifiziert.
Die Analyse der azimuthalen Verteilungen bedingt die Transformation des azimuthalen Winkels in das Referenzsystem der Reaktionsebene. Diese wird durch den Stoßparameter und die Beamrichtung aufgespannt. Die Reaktionsebene wird mittels der Zuschauerteilchen im Forward Wall rekonstruiert. Die so erhaltene Ebene wird als Eventebene bezeichnet, da sie nur eine Abschätzung der waren Reaktionsebene darstellt. Anschließend wurden die Teilchenverteilungen relativ zu der Eventebene betrachtet. Aufgrund der begrenzten Teilchenzahl müssen die Ergebnisse anhand der Eventebenenauflösung korrigiert werden. Zudem werden Effizienzkorrekturen benutzt, um die Symmetrie des Flows um die mittlere Rapidität bestmöglich zu gewährleisten und somit einen Flowbeitrag zu den Korrelationen zu unterbinden. Deshalb war es notwendig, zusätzlich Schnitte in Spektrum des transversalen Impulses durchzuführen: $p_t > 600$ MeV/c für Protonen und $150 < p_t < 600$ MeV/c für Pionen. Die Zweiteilchenkorrelationen wurden aber auch im gesamten Phasenraum betrachtet, genauso wie mögliche Beiträge durch Detektoreffekte. Zur Abschätzung weitere Untergrundquellen wurde die Mixed-Event Methode angewandt und Monte-Carlo Simulationen durchgeführt, wobei das UrQMD Modell verwendet wurde.

Contents

1 Introduction

1.1 Motivation

The science of physics has a very long history. The starting point was in the fifth century BC. From the philosophers in the ancient Greece it more and more developed the idea to describe nature in a mathematical way. Later on, this led to two fundamental topics in physics: the cosmology and particle physics. Today, we know that the fundamental effects at the level of the smallest particle we observed are crutial for what happens at the largest scales in the Universe.
In particle physics, the Standard Model (SM) is a well established theory and describes most of phenomena and experimental results originating from the fundamental particles and three of the four fundamental forces [1]. This theory is confirmed by large amount of experiments but it still does not provides the full picture.
In the SM matter is built up of elementary particles which can be seperated into two main cathegories: quarks and leptons. Both appear in three generations but stable matter is only made up of particles from the first generation since particles from higher generations are heavier and decay very quickly. An overview of all particles from the SM is shown in figure 1.1.

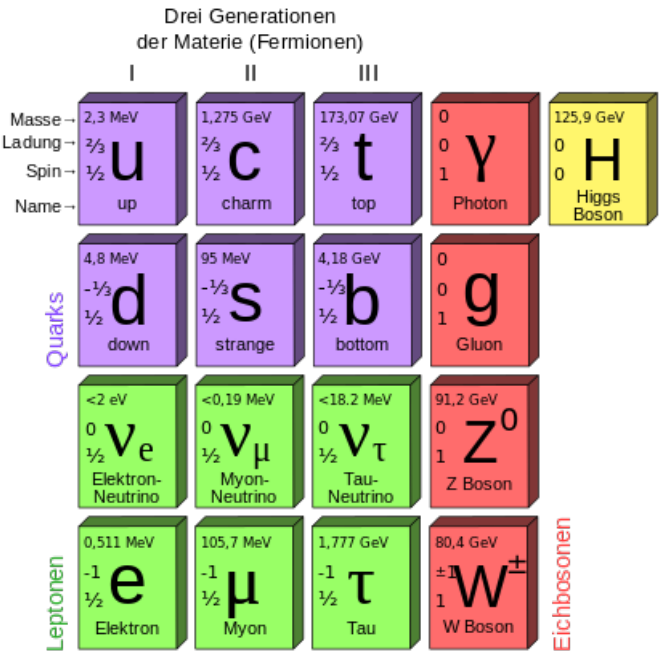

Figure 1.1: All particles of the SM: the quarks (purple), the leptons (green), the force carriers (red) and the Higgs-Boson (yellow) [2].

Quarks and leptons are fermions which means that they have spin $s = 1/2$. The characteristics of fermions is that they cannot occupy the same state which means that for two fermions there must be at least one quantum number by which they differ.
On the other hand, bosons have integer spin $s = 0, 1, 2, \ldots$. All the "red marked" particles and the "yellow" one in figure 1.1 are bosons. The "red marked" bosons are responsible for the transfer

of the fundamental interactions. Each boson corresponds to one of the fundamental forces. The Higgs-Boson (indicated in yellow) recently found in 2012 [3], [4] is responsible to give the rest mass to all other particles.
Even if we have very good theories in particles physics (SM) and in cosmology (General theory of relativity) a combined theory is still missing. The SM does not describe gravitation as the fourth fundamental interaction. Additionaly it does not answer the questions concerning dark matter and the imbalance between matter and anti-matter in the observed Universe. At the moment scientists cannot explain why our Universe is built up from matter. Hence, the answer could be in the initial state of the Universe. To do research in this field several accelerators are built all around the world to create matter in a phase comparable to the state of the universe $t \sim 10^{-30}$ s after the Big Bang. This is the time scale when the temperature became low enough that quarks and anti-quarks could decouple out of photons.
From the experiments, up to now there is no evidence for a mechanism that produces only matter (or only anti-matter). If new particles are formed they always come up in pairs of the created particle and its anti-particle, for example a photon decays into a electron-positron pair ($\gamma \rightarrow e^+e^-$).
Even if the field of particle physics is quite advanced there are still some open question and thus a good motivation to continue research to learn more about the nature.

1.2 QCD and the phase diagram

Quantum Chromodynamics (QCD) is the theory of the strong interaction. As a relativistic quantum field theory it is formulated in analogy to a well understood and proved theory: Quantum Electrodynamics (QED) which is used to describe the electromagnetic interaction. In contrast to QED where the photon is neutral (in the sense of electic charge), in QCD gluons carry charge[1]. This has a lot of consequences since gluons are able to interact among themselfs. As a consequence the coupling constant α_S of the strong interaction is dependent on the distance[2].
For small distances $r \to 0$ the coupling of the strong interaction gets low $\alpha_S \to 0$. This is called the asymptotic freedom of QCD and can be treated by perturbation theory.
For large distances the coupling is very strong, which leads to the so called confinement of the quarks into hadrons[3]. Since there are no free quarks the measurement of their properties becomes difficult. Therefore, a lot of experiments all around the world are built to investigate the different phases of QCD matter and are trying to provide a full picture of non-pertubative QCD which is summarized in the QCD phase diagram. A schematic sketch of the QCD phase diagram represented in terms of temperature T and baryochemical potential μ_B[4] is shown in figure 1.2.

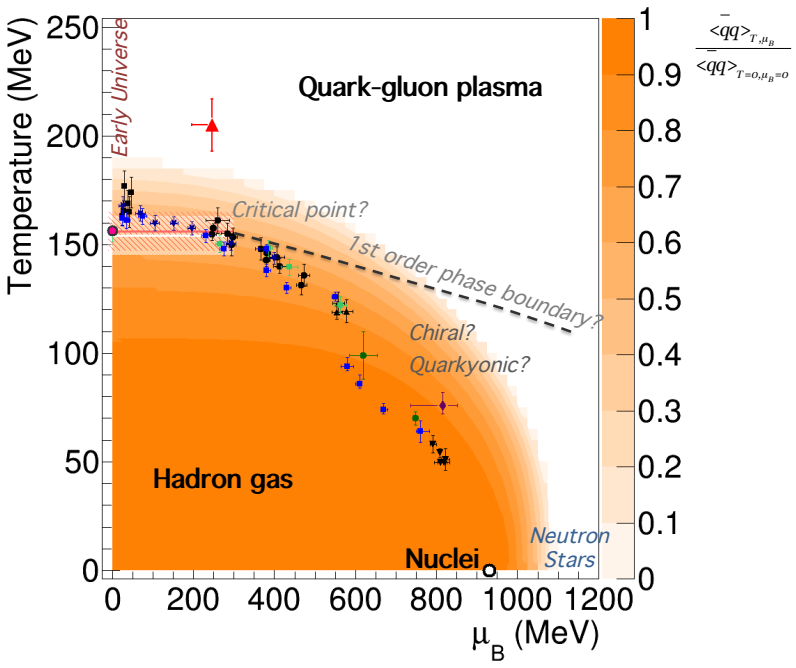

Figure 1.2: The phase diagram of QCD matter as a function of temperature T and baryochemical potential μ_B [6]. With their heavy-ion programs, LHC and RHIC are studying at low μ_B but high T in the region where the phase transition between the hadronic phase and the quark-gluon plasma (QGP) takes place.

1 The charge of QCD is called color. There exist six colors: red, green, blue and their anti-colors.
2 Considering the parton model [5], a dependence on the distance r is equivalent to a $1/Q^2$ dependence where Q^2 is the 4-momentum transfer.
3 Hadrons are particles which are built up of quarks. Since such objects have to be color neutral, there can be three-quark system called baryons or quark-anti-quark systems called mesons.
4 The baryochemical potential is defined by the energy which is needed to introduce a baryon to the system and characterizes the imbalance of matter and anti-matter.

The main partitions of the QCD phase diagram are determined by the asymptotic freedom and by the symmetries of QCD [7].
In the region of low temperature and baryochemical potential where the 4-momentum transfer is small, quarks are confined in color singlet hadrons and the masses of the hadrons are in the range of $\Lambda_{\mathrm{QCD}} \approx 200\,\mathrm{MeV}$ [5]. This is related to the large difference between the effective quark mass of $m_q \approx \Lambda_{\mathrm{QCD}}$ [6] and the bare quark mass of a few MeV [7].
In the same region quarks and anti-quarks form a vacuum condensate $\langle \bar{q}q \rangle \approx -\Lambda^3_{\mathrm{QCD}}$ which breaks the approximate chiral flavor symmetry of the QCD Lagrangian.
To explain the concept of chiral symmetry one can take a look to a more intuitive quantity: the helicity. The helicity of a particle is defined by the relative orientation of its spin with respect to its momentum. If they are parallel (antiparallel) the particle is called right-(left-)handed. For a particle with vanishing mass there is no reference frame which moves faster than this particle so the helicity is a conserved quantity in this case. If helicity would be a conserved quantity in QCD there would be no interaction that turns a left-handed into a right-handed quark or vice versa. In this case, the quark wave function could be splitted into a left- and a right-handed part which could be treated independently.
To use this concept in QCD the chirality is introduced since it can also be used if the particle has a finite rest mass. In this case, the chiral symmetry is explicitly broken and the QCD Lagrangian[8] can be writen as:

$$\mathscr{L}_{\mathrm{QCD}} = \bar{q}_R(i\gamma^\mu D_\mu)q_R + \bar{q}_L(i\gamma^\mu D_\mu)q_L - m_q\bar{q}_R q_L - m_q\bar{q}_L q_R. \tag{1.1}$$

For the quarks of the first generation with rest mass only about 1% of the nucleon mass the chirality is approximately conserved by the QCD Lagrangian. The ground state also called chiral condensate $\langle \bar{q}q \rangle = \langle \bar{q}_L q_R + \bar{q}_R q_L \rangle$ is a measure of the coupling between different chiralities and has a finite value as discussed above. This leads to a spontaneous breaking of the chiral symmetry[9].
The nuclear matter is characterized by a low T and $\mu_B \sim 900\,\mathrm{MeV}$. This is the matter we are built of and that is mainly surrounding us. Therefore, there is a special field of study called nuclear physics[10].
To achive a phase with high μ_B there are two possible ways [9]. The first way is to do a rapid squeeze which also leads to strong heating. This is done using heavy-ion collisions (HIC) at relativistic energies (see section 1.3). The second way is to do a slow squeeze to achieve cold matter with high μ_B but this cannot be done in the laboratory. This phase of QCD matter only exists in the inner core of a neutron star for a few seconds after its birth in a supernova explosion. Under such conditions the density of states near the quark Fermi surface is large which leads to color superconductivity and the formation of a $\langle qq \rangle$ condensate [7].

[5] Λ_{QCD} is the scale parameter of QCD. It appears in the formula for the strong coupling constant and is the only free parameter of the QCD [5].
[6] The mass of the proton is $m_P = 938\,\mathrm{MeV}$ [8]. Hence the effective quark mass is about $m_q \approx m_P/3 \approx \Lambda_{\mathrm{QCD}}$.
[7] Only up- and down-quarks are considered so far.
[8] The Lagrange density or Lagrangian is a useful tool to describe the fields in quantum field field theory. It enables to derive the equations of motion in a very simple way.
[9] If the Lagrangian has a symmetry which is not preserved by the ground state this is called spontaneous symmetry breaking.
[10] The aim of nuclear physics is to describe the behavior of the atomic nucleus. The nucleus consists of nucleons (protons and neutrons) which are kept together by the strong force that step outside the nucleon and result in an attractive potential between them.

At low μ_B but high T there exists a phase called quark-gluon plasma (QGP) which was also present at the early stages of the Universe. Since under such conditions the quarks have thermal momenta $p \sim T \ll \Lambda_{\mathrm{QCD}}$, the 4-momentum transfer in this phase is very high and the strong coupling gets weak leading to a free motion of the quarks within the QGP. This means that there is no confinement of the quarks to color neutral objects and no chiral symmetry breaking[11]. Therefore there must be a phase transition[12] from the hadronic phase to the QGP when the QCD matter is heated up. From calculations on a fixed lattice using realistic quark masses of $m_u \approx m_d \approx 10\,\mathrm{MeV}$ and $m_s \approx 120\,\mathrm{MeV}$ this phase transition turns out to be a rapid crossover [10]. The transition is located at a critical temperature in the range of $T_c \sim 150\,\mathrm{MeV}$ for $\mu_B \sim 0$. There are two facilities studying this region of the phase diagram using ultrarelativistic collisions: the Large Hadron Collider (LHC) at CERN and the Relativistic Heavy Ion Collider (RHIC) at Brookhaven National Laboratory. Both facilities use heavy-ions to do research also in the region of higher μ_B.
When increasing the baryochemical potential, the phase transition is expected to turn into a first order phase transition [11]. The critical end point where the order of phase transition is changing is of special interest because it manifest itself via a divergence of the correlation length [7]. In heavy ion collisions this leads to an enhancement of the fluctuations[13]. Hence changing the collision energy and the ion type, heavy-ion collisions are a good tool to scan the phase diagram in the region of high μ_B and high T, since for a lower collision energy more baryons are stopped and then contribute to the initial state of the collisions which means that the baryochemical potential is higher.
Therefore, the HADES detector has been installed at the GSI facility. With beam energies of a few GeV per nucleon the HADES detector is supposed to explore the region below the phase transition to the QGP. But it is still a question if the transition to the deconfined phase and the restoration of the chiral symmetry happens at the same time in this region of high μ_B. There are also arguments for another exotic state called quarkyonic matter [12]. In this phase the quarks are still confined but the chiral symmetry is restored. If the two transition lines are different HADES could also contribute to the study of quarkyonic matter.

[11] i.e. the chiral condensate vanish: $\langle \bar{q}q \rangle = 0$.

[12] Usually the chiral condensate is used as an order parameter for this phase transition. The evolution of $\langle \bar{q}q \rangle_{T,\mu_B} / \langle \bar{q}q \rangle_{T=0,\mu_B}$ for a certain μ_B as a function of temperature tells us about the order of the phase transition.

[13] For example the variance of the net proton number: $\langle (\Delta N_P)^2 \rangle = \langle (N_P - \langle N_P \rangle)^2 \rangle$ where N_P is the number of protons minus anti-protons.

1.3 Heavy-ion collisions

As mentioned before the only way to achieve strongly compressed and heated QCD matter in the laboratory is to use heavy-ion collisions. In principle, there are two types of experiments. One posibility is to accelerate the target particles in opposite directions and let them collide. This allows to achieve very high collision energies[14] but also requires a more complex accelerator and detectors covering the full space around the collision region. The other way is to use a fixed target setup where the accelerated particles are shouted on. This allows to build more compact detectors since the particles are emitted within a small polar range[15]. In addition, the interaction probability is higher in case of a fixed target experiment.
When two nuclei collide what is important first is the overlap region between the two nucleon distributions. The physical quantity to describe this is the impact parameter which is defined as the distance between the center of masses of both nuclei in the plane perpendicular to the beam direction. The impact parameter is not directly measurable but it can be estimated from the measured particles multiplicities. Since a collision is a statistical process, cross sections are used to desribe the possibility of two nuclei to collide. To make the connection of measured quantities (particles multiplicities, target thickness, ...) and the physics of the collision (impact parameter as a measure for the centrality of the collision) the Glauber model is used [13].
There are several different stages of a collision process which can be seen in figure 1.3.

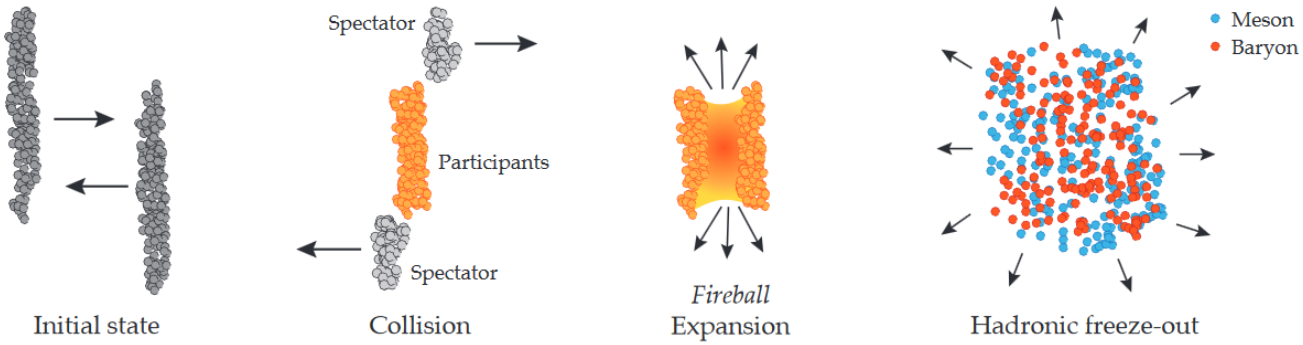

Figure 1.3: The different states of a heavy-ion collision. In the center of the collision a hot and dense fireball is built which expanse until its freeze-out [14].

In the initial state the two Lorentz-contracted nuclei are moving against each other[16]. Then the kinetic energy is transformed into thermal energy, compression energy and excited states.
When the collision takes place there are always some nucleons passing by which are not affected by any interaction[17]. They are called spectators and are used to calculate the reaction plane in HADES (see section 3.4). All the other particles are called participants. They form a hot and dense fireball[18] which expands driven by pressure gradients. In the fireball the maximum temperatures go up to $T_{\mathrm{MAX}} \sim 100\,\mathrm{MeV}$ and the density is about $\rho_{\mathrm{MAX}} \sim 3 \cdot \rho_0$ for HADES energies[19]

[14] The collision energy is the center-of-mass energy and it is higher for a collider than in a fixed target experiment.
[15] In case of HADES the polar range is $0° \leq \theta \leq 85°$ (see chapter 2).
[16] Note that this is ment in the center-of-mass frame, so its also the case in a fixed target experiment.
[17] For sure there will be some elastic scattering due to eletromagnetic field but with only very small 4-momentum transfer.
[18] The fireball is built about $\tau \sim 1\,\mathrm{fm/c}$ after the collision.
[19] The energies of HADES are in the range of a few GeV per nucleon.

where ρ_0 is the nuclear ground state density [15].
While expanding the fireball cools down until the freeze-out[20]. First there is the so called chemical freeze-out which means that there is no inelastic scattering and hence no production of new particles any longer[21]. The elastic scattering continues until the kinetic freeze-out. In this stage of the collision, the system is in equilibrium having a common temperature. Then the emitted particles fly in all directions and can be detected. The whole time from the initial state to the kinetic freeze-out is only about $t \sim 10^{-22}$ s. Therefore, its impossible to measure the collision process directly. One can only measure the end products of the collision and then try to reconstruct what has happened but one always relies on models.
One model used in this thesis is the UrQMD model [16], [17], [18]. As a microscopic transport model it combines the classical transport theory with quantum mechanical equations of motion. It contains the known hadronic interactions and their resonances in the low and intermediate energy range $\sqrt{s_{\mathrm{NN}}} < 5$ GeV. For higher energies the particle production in the UrQMD model is dominated by the excitation of color strings and their fragmentation into hadrons.
Another important point for the following analysis are the magnetic fields produced in a heavy-ion collision. Since the heavy ions carry large positive charges the electric vector current $\vec{j}_V$ is large leading to very strong magnetic fields (see table 1.1).

Magnetic field of the earth	Dipole magnet at LHC	Neutron star	Magnetar	HIC
$\sim 10^{-5}$ T	~ 10 T	$\sim 10^{8}$ T	$\sim 10^{11}$ T	$\sim 10^{14}$ T

Table 1.1: Comparison of the magnetic field values of different phenomena. The magnetic field in a heavy-ion collision is up to three orders of magnitude larger than of a magnetar.

Of particular interest in the magnetic field in the fireball. The strongest contribution to the magnetic field is originated from the spectators of the collision since their motion is nearly parallel and so their magnetic fields add up. Hence the magnetic fields produced by the spectators are very strong and also nearly homogeneous in the region of the fireball as it is illustrated in the right panel of 1.4.
To get a feeling of how much the different stages of the collision are affected by the magnetic field one has to look to the time evolution (left panel of figure 1.4). Taking a typical collision time of $\tau \sim 10$ fm/c the lifetime of the magnetic field is almost two orders of magnitude shorter in case of LHC or RHIC energies compared that at HADES. Hence for them the magnetic field affects only the very first stages of the collision but with a very strong maximum of the magnetic field strength.

[20] The timescale after the collision for the freeze-out is about $\tau \sim 10$ fm/c.
[21] But there are still decays.

	STAR ($\sqrt{s_{NN}} = 200\,\text{GeV}$)	HADES ($\sqrt{s_{NN}} = 2.42\,\text{GeV}$)
maximal $eB \propto \sqrt{s}$	$\sim 2 \cdot 10^{18}$ Gauss	$\sim 2.4 \cdot 10^{16}$ Gauss
maximum at $t_m \propto 1/\sqrt{s}$	~ 0.05 fm/c	~ 4.1 fm/c
lifetime $t_l \propto 1/\sqrt{s}$	~ 0.3 fm/c	~ 16 fm/c

Table 1.2: Comparison of the magnetic field evolution between STAR and HADES energies. For HADES energies the lifetime is much larger but the magnetic field strength decreased by two orders of magnitude.

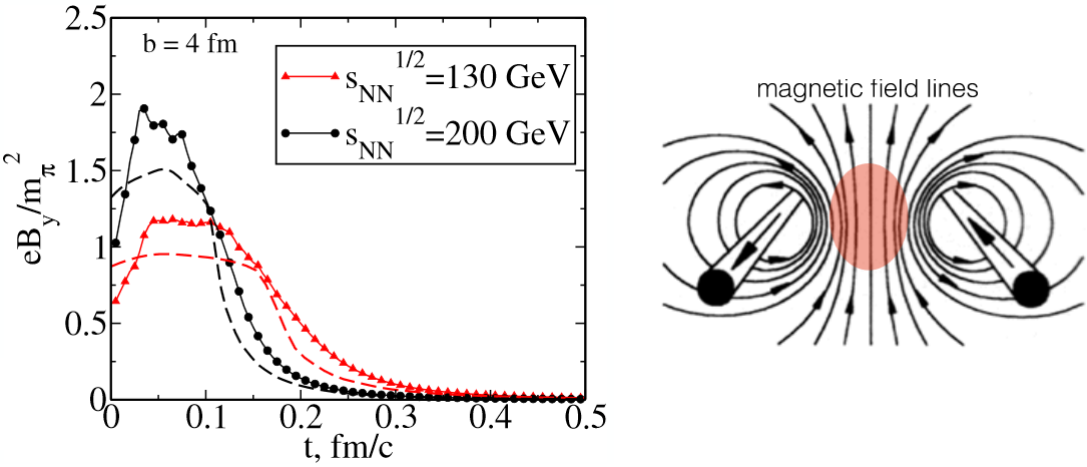

Figure 1.4: Left panel: Time evolution of the magnetic field strength in the center of the collision as calculated from the UrQMD model for typical RHIC energies [19]. Right panel: Illustration of the magnetic field created by the spectators in a heavy ion collision [20]. In the region of the fireball the magnetic field is nearly homogeneous.

For HADES energies the situation is different. Using the dependence on the collision energy $\sqrt{s}$ (see table 1.2) one can estimate the magnetic field evolution for the Au+Au beamtime at HADES with $\sqrt{s_{\text{NN}}} = 2.42.\,\text{GeV}$. The magnetic field is expected to have a lifetime comparable to the evolution of the fireball which could lead to different phenomena like a possible Hall-effect. The maximum value of the magnetic field strength is expected to be two orders of magnitude lower and hence its not fully clear how this will influence the possible occurence of the CME (see section 1.4).

1.4 The chiral magnetic effect

Starting from the SM it is not clear, why parity (*P*) and the combination of parity and charge conjugation (*CP*) are conserved by the strong interaction. Heavy-ion collisions could bring up the evidence for a local *P* and *CP* violation. It was proposed that in the vicinity of the deconfinement phase transition the QCD vacuum could form the so called "*P*-odd bubbles" meaning a metastable domain where *P* and *CP* are violated locally [21].
The origin of this idea is in the topological solitons. Solitons are exact solutions to the classical equations of motion for field theories due to their nonlinearity and describe the tunneling between different vacua states which can be characterized by the topological charge Q_W [22]. These "instantons" are strongly suppressed [23]. Due to the hot and dense matter created in heavy-ion collisions there could be thermal transitions[22] between vacua states, the so called "sphalerons". The typical energy of such a sphaleron is about $\Lambda_{\mathrm{QCD}} \approx 200\,\mathrm{MeV}$ and hence for high temperatures the transition rate Γ would increase since $\Gamma \propto T^4$ is expected [23].
If such a sphaleron transition occurs in heavy-ion collisions, this would mean that there is a non-zero topological charge. In the chiral limit[23] the topological charge is directly related to the net chirality:

$$2Q_W = N_L^f - N_R^f \,. \tag{1.2}$$

Here N_L^f and N_L^f are the number of left- and right-handed fermions, respectively and the index f denotes the different quark flavors. In other words, a non-zero topological charge generates a net chirality, i.e. an imbalance between left- and right-handed quarks. Thus, there is a creation of matter with a non-zero axial charge density μ_A which is a parity-odd quantity [24].
In order to measure this effect through a charge separation there are three points which have to be considered [23]. First there must be a symmetry axis along which the charges are separated. In a heavy-ion collision, the only symmetry axis is the angular momentum. As a second point, the effect should violate isospin in order to separate a π^+ from a π^-. Finally, the mechanism should conserve the charge conjugation *C* in order to break *P*- and *CP*-symmetry. Thus, it must depend on the electric charge of the ions. Following the arguments a possible charge separation should depend on the magnetic field $\vec{B}$ which satisfies all three requirements. As explained in section 1.3 magnetic fields occur in each heavy-ion collision. If on average in each event there is a finite amount of topological charge in addition[24], an electric current is created

$$\vec{j}_V \propto \mu_A \cdot \vec{B} \tag{1.3}$$

which separates the charges along the magnetic field lines [24].
To get a better feeling on the chiral magnetic effect let us consider this effect first in the presence of very large and homogeneous magnetic fields, i.e. $eB \gg p^2$, which in fact means that the collision energy is very large (see section 1.3). Due to the magnetic moment interaction all spins are aligned parallel (antiparallel) to the magnetic field in case of positively (negatively) charged particles. Additionaly, since the magnetic field is so strong, all fermions are situated in

[22] This means that the energy is high enough to pass over the barrier.
[23] In the chiral limit the quark masses vanish.
[24] This is a realistic assumption if the temperature of the created matter is high enough.

the lowest Landau level which means that they can only move along the magnetic field (first panel of figure 1.5). The fermions will interact with the underlying gauge field configuration such that some of them will flipp their momentum[25] depending on the topological charge of the domain. If according to equation 1.2 a net chirality is created this leads to a charge separation (see third panel of figure 1.5).

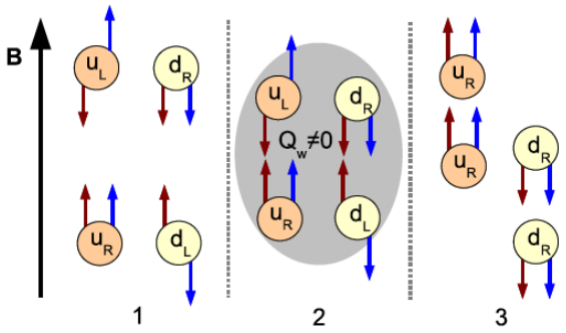

Figure 1.5: Illustration of how a parity-odd domain creates a chiral imbalance which results in a charge separation in the presence of an external magnetic field which is large (i.e. $eB \gg p^2$) and homogeneous [23].

The maximum amount of electric charge which can be separated is given by

$$|Q_{\max}| = 2|Q_W| \sum_f |q_f|, \tag{1.4}$$

where q_f is the electric charge of a certain quark flavor. $Q_{\max}$ has to be considered as an upper limit since it was obtained for the chiral limit and very large magnetic fields. Assuming that only u- and d-quarks are involved ($f = 2$) and the topological charge is $|Q_W| = 1$ the separated charge in units of the elementary electric charge e is $Q = 2$. This means that in this case, only two u- and d-quarks are involved. Therefore, an electric "back-reaction" caused by the repulsive electric force acting against the charge separation can be reasonably ignored [23]. A gluonic back-reaction which would be much stronger is not involved since the chiral magnetic effect is independend of the color charge.
In case of HADES energies the magnetic fields are not expected to be as strong. Therefore, one might look what happened to the chiral magnetic effect if the magnetic field strength decreases. In case of moderate magnetic fields, i.e. $eB \sim p^2$, not all particle spins are aligned any longer. Additionaly, quarks with momenta much larger than the inverse size ρ of the parity-odd domain will not be affected by a change in helicity. Of course this will reduce the amount of charge that is separated, but there is still a good chance that a reasonable amound of charge is separated. In [23] the authors estimated the separated charge to be

$$Q \approx 2Q_W \sum_f |q_f| \, \gamma\left(2|q_f eB\rho^2|\right) \tag{1.5}$$

with $\gamma(x) = 1$ for $x \geq 1$ and $\gamma(x) = x$ for $x \leq 1$. Hence, only in case $eB < \rho^2$ the separated charge is reduced by a factor $2eB\rho^2$.

[25] This means that these fermions change their chirality.

1.5 Azimuthal angular distribution

To simplify the calculations of different observables it is useful to change the reference frame such that the symmetry axis, i.e. the angular momentum of the fireball $\vec{L}$ (or the magnetic field $\vec{B}$) is along one of the frame axis. This reference frame is called the reaction plane frame. The reaction plane is defined by the beam axis and the direction of the impact parameter (see figure 1.6) and hence it has to be reconstructed for each collision (see section 3.4). Any effect depending on $\vec{L}$ (or $\vec{B}$) will show different behavior in-plane compared to the out-of-plane direction. Additionally, it allows to measure collective flow effects which contains informations about the fireball like thermalization, pressure gradient, time evolution, etc [25].

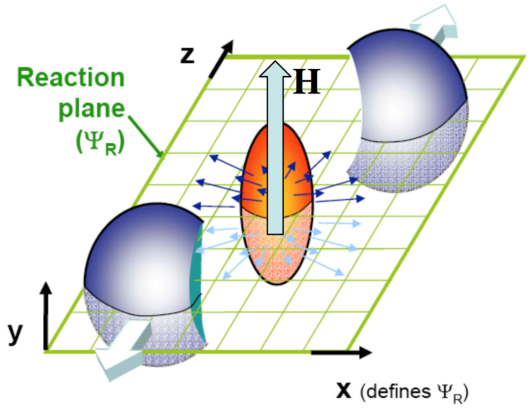

Figure 1.6: The reaction plane is spanned by the beam axis (z-direction) and the impact parameter (x-direction) [26]. The magnetic field is perpendicular to the reation plane.

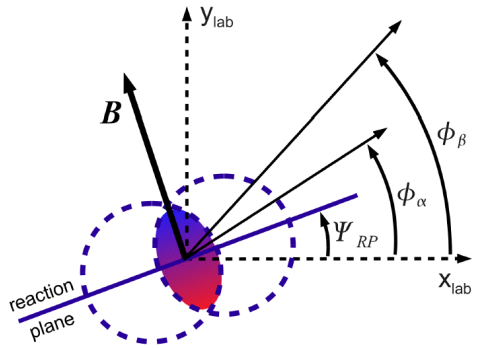

Figure 1.7: Sketch of the particle azimuthal angles ϕ_α and ϕ_β and the orientation of the reaction plane Ψ_{RP} [27].

All the particle azimuthal angles are translated to this reference frame to describe the particle production relative to the reaction plane (see figure 1.7):

$$\Phi = \phi - \Psi_{RP}, \tag{1.6}$$

where Ψ_{RP} is the reaction plane angle and ϕ is the particle angle both in the laboratory frame. Of interest is the study of azimuthal angular distributions with respect to the reaction plane. Its important that the particles used to reconstruct the signal are different from the ones used to reconstruct the reaction plane to avoid auto-correlations. Typically the particle distribution is given in the coordinate system of rapidity y, azimuthal angle ϕ and transvers momentum p_t. When talking about the azimuthal angular distribution this means that it is considered in bins of rapidity and transvers momentum or integrated over these variables.
The single particle distribution can be expressed in terms of a Fourier expansion [28]:

$$f_1(\Phi) = \frac{dN_\pm}{d\Phi} \propto 1 + 2v_{1,\pm}\cos(\Phi) + 2v_{2,\pm}\cos(2\Phi) + ... + 2a_{1,\pm}\sin(\Phi) + 2a_{2,\pm}\sin(2\Phi) + ... \tag{1.7}$$

Here v_1 and v_2 represent the flow coefficients for directed and elliptic flow, respectively. They are given by

$$v_k = \langle \cos(k\Phi) \rangle = \frac{\int d\Psi_{\mathrm{RP}} \int d\phi \, f_1(\phi - \Psi_{\mathrm{RP}}) \cos[k(\phi - \Psi_{\mathrm{RP}})]}{\int d\Psi_{\mathrm{RP}} \int d\phi \, f_1(\phi - \Psi_{\mathrm{RP}})} \tag{1.8}$$

and can be determined in the experiment[26] by

$$v_k = \frac{1}{N_{\mathrm{events}}} \sum_{\mathrm{event}\, i=1}^{N_{\mathrm{events}}} \left[\frac{1}{N(i)} \sum_{\mathrm{particle}\, j=1}^{N(i)} \cos[k(\phi_j - \Psi_{\mathrm{RP}}(i))] \right]. \tag{1.9}$$

So for each event, one first has to determine the reaction plane angle. Then the average moment in the intrinsic frame must by calculated for each event, denoted by the average over all particles. Afterwards, this has to be averaged over many events.
The same can be done for the sine terms in formula 1.7 in order to calculate the a_k. Since the sine terms are not symmetric for $\Phi \to -\Phi$, because $\sin(\Phi) \neq \sin(-\Phi)$, an $a_k \neq 0$ would mean a parity violation. Since parity is a globally conserved quantity, all a_k have to vanish when averaging over many events.
For the analysis in this thesis, the motion of two particles relative to each other will be investigated. Therefore, one has to analyze two-particle distributions. In general, they can be writen as a multiplication of their single particle distributions plus a term representing possible (true[27]) two-particle correlations [24]:

$$f_2(\Phi_1, \Phi_2) = f_1(\Phi_1) f_1(\Phi_2) + C(\Phi_1, \Phi_2). \tag{1.10}$$

From the multiplication of the single particle distributions, there will be terms which depend on the difference of the two angles $\sim (\Phi_1 - \Phi_2) = (\phi_1 - \phi_2)$ and are independent of the reaction plane orientation as well as reaction plane dependend terms $\sim (\Phi_1 + \Phi_2) = (\phi_1 + \phi_2 - 2\Psi_{\mathrm{RP}})$. This is important when we introduce possible observables for the CME in the following section. They will also contain contributions related to these terms arising from the single particle distribution and thus one has to find a way to disentangle the quantities to determine the true two-particle correlations.

[26] This is only true when all fluactuations and non-flow effects are under control.
[27] This is because the single particle distributions do also contribute to multi-particle correlations and have to be disentangled from multi-particle correlations.

1.6 How to measure the CME

The presence of the chiral magnetic effect lead to a charge separation along the magnetic field. Therefore, one has to study the particle motion relative to the reaction plane, i.e. the azimuthal angle in the reaction plane frame Φ.
No doubts about existance of parity-odd domains in a heavy-ion collision if the temperature is high enough. Each time a sphaleron transition takes places this results in an electric current along the magnetic field. In one single event this charge separation is so small that statistical fluctuations $\sim \sqrt{N}$ are much larger. Therefore, one has to consider a sample of events. Since the sign of the charge separation is randomly distributed, even in the reaction plane frame when averaging over many events it would disappear, i.e. $\langle a_n \rangle = 0$. Thus one has to construct observables which are sensitive to the variation a_n^2.
A very useful observable was proposed by Voloshin [29]:

$$\begin{aligned} \gamma_{\alpha\beta} = \langle \cos(\Phi_\alpha + \Phi_\beta) \rangle &= \langle \cos(\Phi_\alpha)\cos(\Phi_\beta) \rangle - \langle \sin(\Phi_\alpha)\sin(\Phi_\beta) \rangle \\ &= \left(\langle v_{1,\alpha} v_{1,\beta} \rangle + B_{\text{in}} \right) - \left(\langle a_\alpha a_\beta \rangle + B_{\text{out}} \right). \end{aligned} \tag{1.11}$$

The brackets $\langle ... \rangle$ denote the average over all particles in an event and then averaging over events (analog to equation 1.9). α and β denote the different particle types and B_{in}, B_{out} represent the in-plane and out-of-plane background, respectively. This background is related to jets or flowing charged cluster decays. Reaction plane independent contributions are of the same order $B_{\text{in}} \approx B_{\text{out}}$ which seams to be reasonable since investigations by the STAR collaboration summerized in [30] show that $B_{\text{in}} - B_{\text{out}}$ is much smaller than the observed signal.
Neglecting this background contribution related to the reaction plane orientation the correlator in equation 1.11 is completely background free since it removes by definition all other backgound. Contirubtions may only arise from directed flow and flow clusters. Since the directed flow is a rapidity-odd quantity the contribution vanishes when a symmetric rapidity window around mid-rapidity is chosen. This allows to get direct access to the strength of the parity violating effect by measuring $\gamma_{\alpha\beta}$.
Yet measuring only the correlator in equation 1.11 is not sufficient. For example a same-side out-of-plane correlation[28] and a back-to-back in-plane correlation[29] result is the same expression:

$$\cos\left(\Phi_\alpha + \Phi_\beta\right) = \cos\left(\frac{\pi}{2} + \frac{\pi}{2}\right) = \cos\left(0 + \pi\right) = -1. \tag{1.12}$$

To distinguish between these two scenarios another observable has been introduced:

$$\begin{aligned} \delta_{\alpha\beta} = \langle \cos(\Phi_\alpha - \Phi_\beta) \rangle &= \langle \cos(\Phi_\alpha)\cos(\Phi_\beta) \rangle + \langle \sin(\Phi_\alpha)\sin(\Phi_\beta) \rangle \\ &= \left(\langle v_{1,\alpha} v_{1,\beta} \rangle + B_{\text{in}} \right) + \left(\langle a_\alpha a_\beta \rangle + B_{\text{out}} \right). \end{aligned} \tag{1.13}$$

[28] This means that the two particle, which are considered are travelling in the same direction along the magnetic field which would indicade the occurance of the CME.
[29] This would mean the two particles are flying in opposite directions within the reaction plane which is not in agreement to the CME.

This correlator is independent of the reaction plane orientation which brings additional difficulties. With the assumption from above $B_{\text{in}} \approx B_{\text{out}}$, the correlator in equation 1.13 depends strongly on the background since the in- and out-of-plane contributions sum up. In addition, the correlator is sensitive to contributions not related to the reaction plane orientation. Therefore, an excellent knowlegde of all background contributions is inevitable to measure a possible charge separation.
Assuming that all background contributions are well known and can be subtracted[30] one can make predictions for both correlators in the presense of the CME.
Since the charge separation happens only along the magnetic field positively charged particles have to travel into the same direction $(\Phi_+, \Phi_+) = (\pi/2, \pi/2)$ or $(3\pi/2, 3\pi/2)$. The same effect one would expect when both particles carry negative charges. If the two particles which are considered carry opposite charges one would expect them to fly into opposite directions $(\Phi_+, \Phi_-) = (\pi/2, 3\pi/2)$ or $(3\pi/2, \pi/2)$. Following this argumentation one can conclude the sign of both correlators $\gamma_{\alpha\beta}$ and $\delta_{\alpha\beta}$ as summerized in table 1.3.

	$(\Phi_\alpha, \Phi_\beta)$	$\gamma_{\alpha\beta}$	$\delta_{\alpha\beta}$
Same charged pairs $(++, --)$	$\left(\frac{\pi}{2}, \frac{\pi}{2}\right)$ or $\left(\frac{3\pi}{2}, \frac{3\pi}{2}\right)$	$\cos(\Phi_\alpha + \Phi_\beta) = -1 < \mathbf{0}$	$\cos(\Phi_\alpha - \Phi_\beta) = 1 > \mathbf{0}$
Opposite charged pairs $(+-, -+)$	$\left(\frac{\pi}{2}, \frac{3\pi}{2}\right)$ or $\left(\frac{3\pi}{2}, \frac{\pi}{2}\right)$	$\cos(\Phi_\alpha + \Phi_\beta) = 1 > \mathbf{0}$	$\cos(\Phi_\alpha - \Phi_\beta) = -1 < \mathbf{0}$

Table 1.3: Predictions from the chiral magnetic effect for the sign of the correlators $\gamma_{\alpha\beta}$ and $\delta_{\alpha\beta}$ if all background contributions are negligible.

If the CME happens in the center of the fireball due to the interactions with the medium there will be no possibility to measure the charge separation. Only if the transition happens near the surface the quarks emitted out of the fireball will hadronize and propagate freely towards the detector. In the most peripheral events the size of the fireball is small enough that also the quarks emitted in the medium can hadronize without many interactions and so the azimuthal angles of the positively and negatively charged fermions are still correlated. This is not the case when the size of the fireball is large, i.e. in the more central events and the argumentation is the same as for transitions in the center of the medium. Therefore one would expect that $\gamma_{\text{same}} \gg \gamma_{\text{opposite}}$ while the difference $|\gamma_{\text{same}} - \gamma_{\text{opposite}}|$ should be the largest in the most central collisions and decreases towards more peripheral collisions.
On the other hand, the magnetic field is mainly created by the spectators. In the most peripheral collision the strongest magnetic field is created and thus the strength of the measured charge separation is at maximum. The more central the collision the stronger the strength of the measured charge separation decreases. In case of a head-on collision all particles participate in the reaction and hence the magnetic field is small and of course not homogeneous. Therefore, in the most central collision the correlators should vanish.
Another important question is the beam energy dependence of the CME. In the following section results from the beam energy scan at RHIC will be shown. Obviously the possibility of a sphaleron transition increases with temperature. The temperature on the other hand depends on the collision energy. At some point when the temperature will be too low, transitions between different vacua states are possible only via tunneling effect. The transition rate should drop markedly and a measurement of the local parity violation gets very difficult (if possible at all). In addition, the CME occurs at the quark level and assumed to take place in a deconfined

[30] In reality this is not satisfied and the understanding of the background is still part of the ongoing work.

quark-gluon plasma in the chiral limit. Hence for lower beam energies at some point the CME cannot appear. Yet the time integral over the magnetic field gets larger when the beam energy is reduced. Assuming to be still above the critical energy such that probability for sphaleron transitions is significant, the CME should be even stronger at low energies.

1.7 Observation of the CME sensitive observables

Measurements of the two-particle correlators in equation 1.11 and 1.13 have been performed by several collaborations. In this section the focus is on the results from the ALICE[31] and the STAR[32] collaborations.
The first results were presented by the STAR collaboration [33] and [34]. In this two papers the results obtained in Cu+Cu and Au+Au collisions with a center-of-mass energy of $\sqrt{s_{\mathrm{NN}}} = 62\,\mathrm{GeV}$ and $\sqrt{s_{\mathrm{NN}}} = 200\,\mathrm{GeV}$ are discussed. The results are shown in figure 1.8.
The corralator is calculated using three-particle correlations while the third particle is used for the reaction plane:

$$\gamma_{\alpha\beta} = \langle \cos(\phi_\alpha + \phi_\beta - 2\Psi_{\mathrm{RP}}) \rangle \approx \langle \cos(\phi_\alpha + \phi_\beta - 2\phi_c) \rangle / v_{2,c}. \tag{1.14}$$

Hence the elliptic flow of the third particle needs to be known precisely. In the results the shaded bands indicate the uncertainty due to the determination of the elliptic flow estimated using different methods [35].
Within statistical errors the correlations $(+,+)$ and $(-,-)$ are found to be the same thus they are combined together as same-charge correlations. First of all, the centrality dependence seams to be consistent with the predictions. For the most central events the correlator converge to zero while it gets most pronounced for the peripheral events.

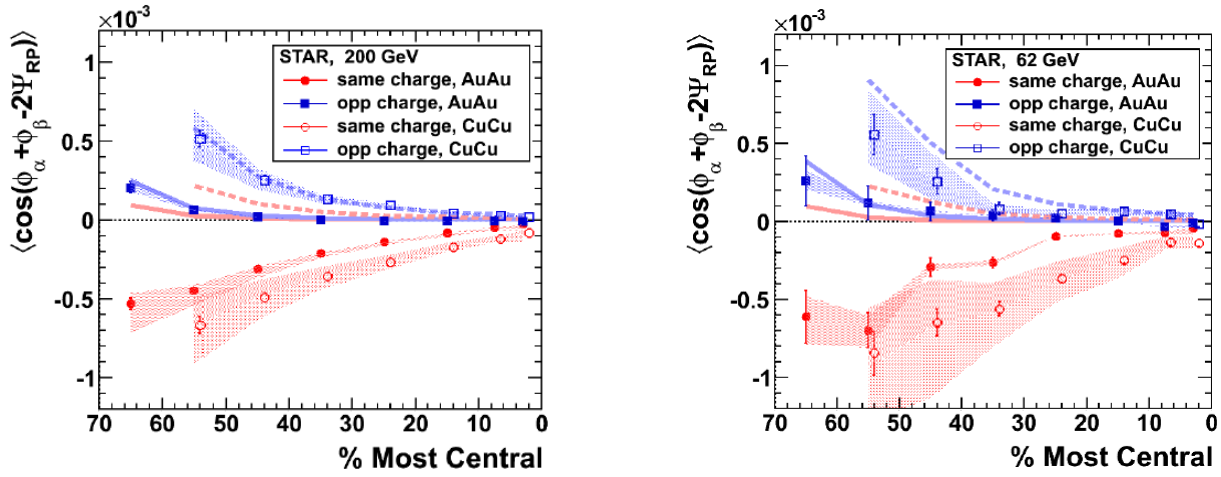

Figure 1.8: $\gamma_{\alpha\beta}$ as a function of centrality for Cu+Cu and Au+Au collisions at $\sqrt{s_{NN}} = 200\,\mathrm{GeV}$ (left panel) and $\sqrt{s_{NN}} = 62\,\mathrm{GeV}$ (right panel). The error bars denote only statistical errors.

As expected from the medium interaction, the opposite-charge correlations are smaller compared to the same-charge ones. When comparing the different systems (i.e. Cu and Au) the value is larger for the lighter system Cu+Cu. This is consistent with the expectation that the correlator depends on $1/N$ where N is the multiplicity. For the same centrality the multiplicity for the Cu+Cu system is smaller since there are less participants. This would also explain why

[31] The **A** **L**arge **H**adron **C**ollider **E**xperiment is situated at CERN (Genf, Switzerland) and uses the beams provided by the **L**arge **H**adron **C**ollider. For more informations see for example [31].

[32] The **S**olenoidal **T**racker **A**t **R**HIC is situated at the **R**elativistic **H**eavy-**I**on **C**ollider in Brookhaven National Laboratory (USA). For more informations see for example [32].

the difference is smaller for opposite-charged pairs since less participants would also mean less medium interactions.
Comparing the two different beam energies the signal seams to be of the same order. Yet the opposite-charge correlators are stronger in case of $\sqrt{s_{\mathrm{NN}}} = 62\,\mathrm{GeV}$. Since the medium is less dense for this lower energy their are less medium interactions and therefore the suppression of opposite-charge correlations is reduced.
Figure 1.9 shows the dependence on the transverse momentum in Au+Au collisions at $\sqrt{s_{NN}} = 200\,\mathrm{GeV}$ for two different centralities ($10-30\,\%$ and $30-50\,\%$ centrality). For the sum of the transverse momentum (left panel) there is no enhancement of the signal in the low p_t range as naively expected by the CME. For the difference in p_t the measured signal doesn't seem to have any dependency. Thus effects from short range correlations and Coulomb interactions can be excluded as a possible source for the signal [34].

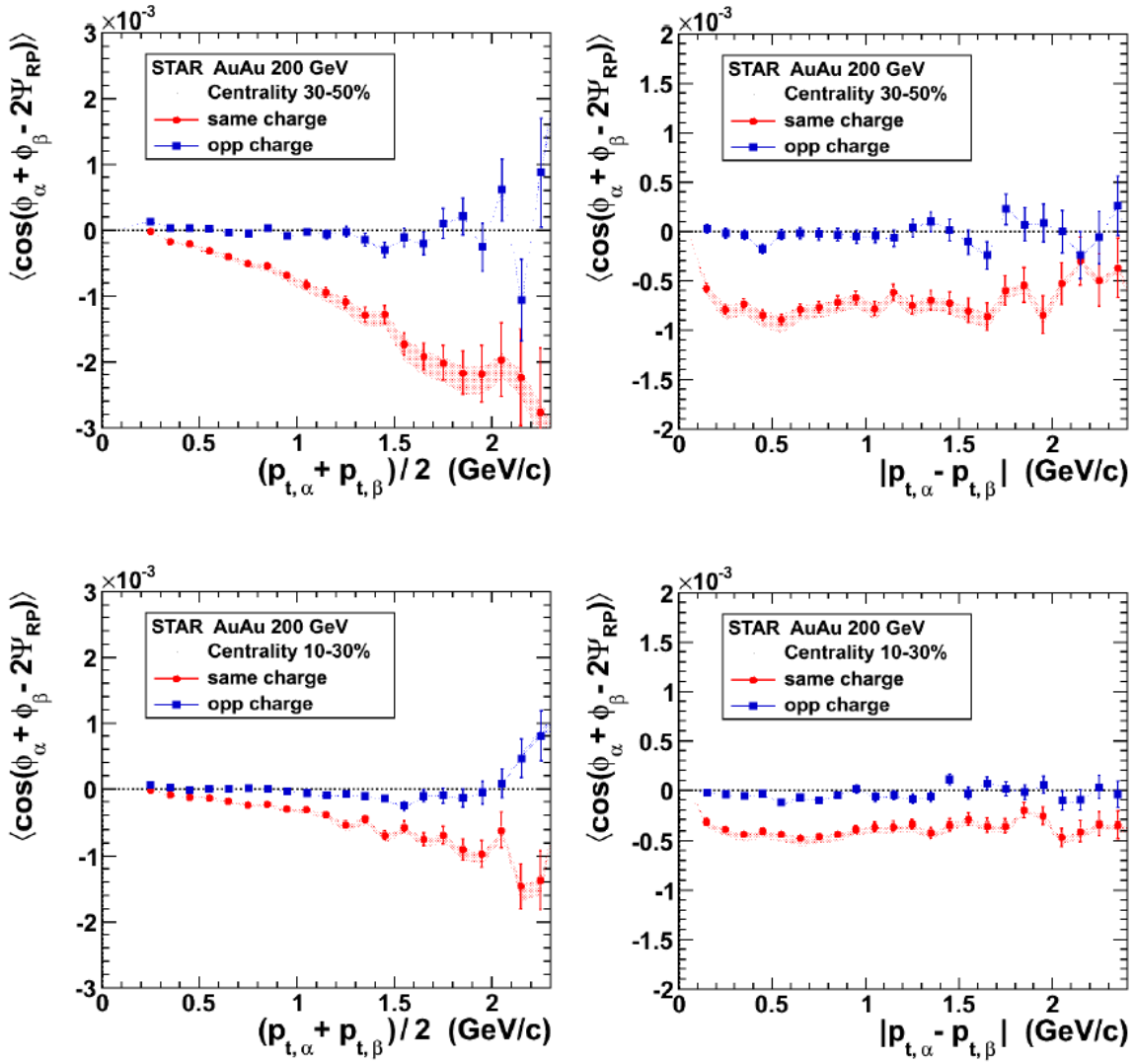

Figure 1.9: The correlator $\gamma_{\alpha\beta}$ as a function of the transverse momentum in Au+Au collisions at $\sqrt{s_{NN}} = 200\,\mathrm{GeV}$ for two different centralities [34].

In [24] the authors decompose the measured signal into the in-plane and out-of-plane components. Therefore, they also used the results for the correlator $\delta_{\alpha\beta}$ (discussed later in this

section). The decomposition can be easely calculated using the formulas for the definition 1.13 and 1.11:

$$\langle a_\alpha a_\beta \rangle = \langle \sin(\phi_\alpha)\sin(\phi_\beta)\rangle = \frac{1}{2}\left(\delta_{\alpha\beta} - \gamma_{\alpha\beta}\right) \tag{1.15}$$

$$\langle v_{1,\alpha} v_{1,\beta} \rangle = \langle \cos(\phi_\alpha)\cos(\phi_\beta)\rangle = \frac{1}{2}\left(\delta_{\alpha\beta} + \gamma_{\alpha\beta}\right). \tag{1.16}$$

The results of the decomposition are shown in figure 1.10. They show exactly the opposite behaviour as predicted by the CME: same-charged particles move mostly in-plane and back-to-back while the opposite-charged particles are likely to move both in-plane as well as in the out-of-plane direction. The latter one can be explained by resonance/cluster decays [36] or local charge conservation [37]. Yet the decomposition is strongly dependent on the results of the correlator $\delta_{\alpha\beta}$. As shown in the previous section this correlator has large contribution due to various background effect and further investigations are needed.

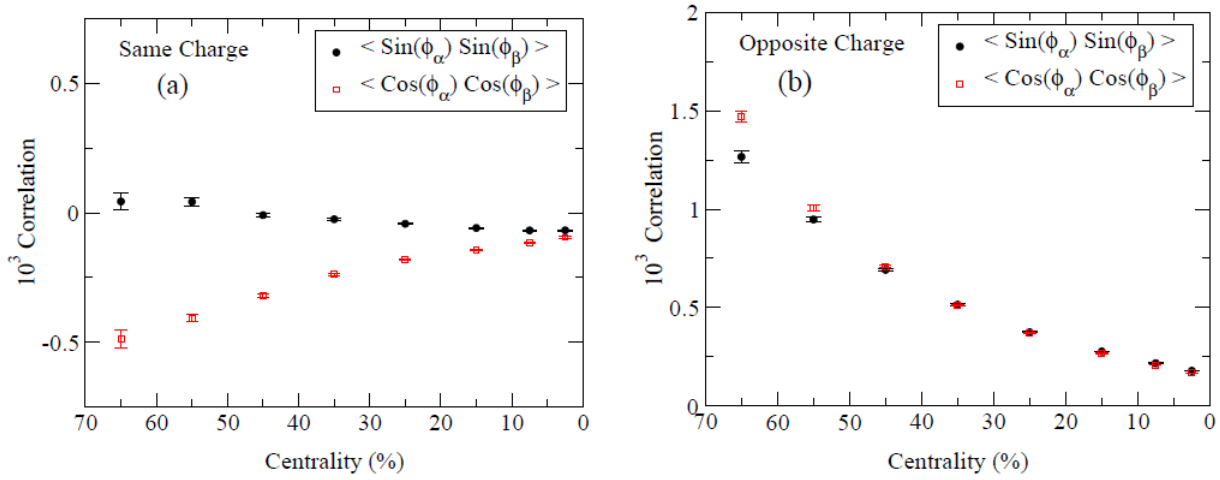

Figure 1.10: The decomposition of the STAR results in Au+Au collisions at $\sqrt{s_{NN}} = 200\,\text{GeV}$. The in-plane components are denote with the red points while the black points denote the out-of-plane components [24].

There are also results measured by the ALICE collaboration [38]. ALICE measured Pb+Pb collisions at mid-rapidity and an energy of $\sqrt{s_{NN}} = 2.76\,\text{TeV}$ which is about one order of magnitude higher compared to the STAR center-of-mass energy. To remove off-vertex tracks the authors required dca $< 2\,\text{cm}$ [33]. The correlators obtained are shown in figure 1.11 as a function of centrality in comparison to the previous results by the STAR collaboration.
The correlators $\gamma_{\alpha\beta}$ are in a very good agreement with each other which leads to the conclusion of no significant dependence on the collision energy observed. We will discuss this in more detail in this section when looking to the beam energy scan done by the STAR collaboration.
The ALICE collaboration used several different methods to calculate the reaction plane. All results are in a very good agreement which leads to the fact that the background contribution due to effects not related to the reaction plane orientation can be neglected.

[33] The **D**istance of **C**losest **A**pproach is the minimum distance between the projection of the particle track and the global event vertex.

For the correlator $\delta_{\alpha\beta}$ the results differ. ALICE obtained both correlators for same- and opposite-charged pairs to be positive. In magnitude the observed correlator is smaller for same-charged pairs which was also found by the STAR collaboration. Yet this only leads to small changes for the decomposition of the signal, i.e. for $\langle \sin(\phi_\alpha)\sin(\phi_\beta)\rangle$ and $\langle \cos(\phi_\alpha)\cos(\phi_\beta)\rangle$. Opposite charges are still likely to move in-plane as well as out-of-plane. For the same charged-pairs the change in sign of the correlator $\delta_{\alpha\beta}$ results in a large $\langle \sin(\phi_\alpha)\sin(\phi_\beta)\rangle$ compared to the $\langle \cos(\phi_\alpha)\cos(\phi_\beta)\rangle$. This means that there is also a large motion in the out-of-plane direction for same-charged particles. But due to the significant non-flow contributions the interpretation of the results is complicated.

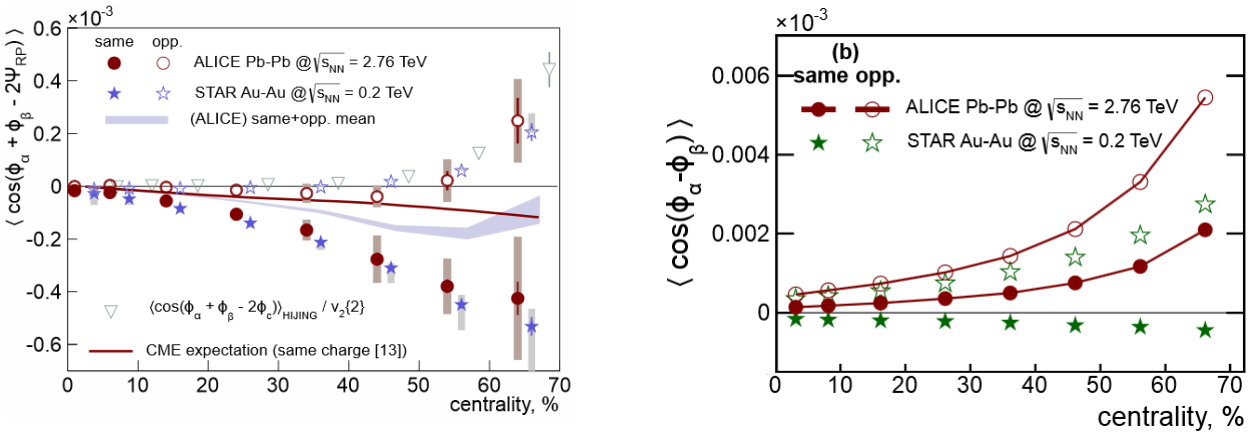

Figure 1.11: Results of the correlator $\gamma_{\alpha\beta}$ (left) and $\delta_{\alpha\beta}$ (right) obtained by the ALICE collaboration compared to the STAR data [38].

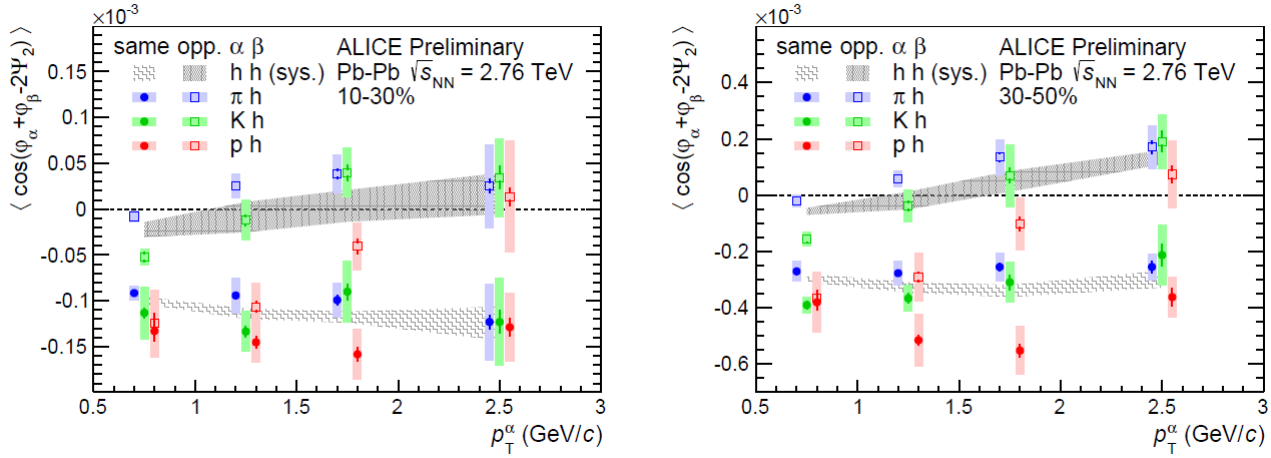

Figure 1.12: Results for the two-particle correlator γ as a function of transverse momentum as measured by the ALICE collaboration [39]. Shown are correlations of protons, kaons, pions with an unidentified hadron for two different centrality bins (left panel: $10-30\,\%$ centrality; right panel: $30-50\,\%$ centrality).

The ALICE collarobration also measured the transverse momentum dependence of the correlator $\gamma_{\alpha\beta}$. For the same-charge correlator the results are similar to the results obtained by STAR. The situation is a bit different for opposite-charged pairs. In case of the p_t difference, the signal strongly increases towards larger values which was not observed by STAR. Additionaly, the sig-

nal depends only weakly on the average transverse momentum. All this does not seem to agree with predictions from the CME since it should only occur in the lower p_t range. Yet there are no realistic models including the CME and possible background contributions which does not allow for any final conclusion.
Two years later ALICE also released the correlator for different particle types [39]. The results are shown as a function of the transverse momentum of the identified particle (see figure 1.12). For the more peripheral collisions the signal is around ~ 3 times stronger than in the more central collisions. In case of the same-charge correlator there is no significant dependence on the particle transvers momentum. Generally, there is also an ordering of the particles, while the signal is smallest for pions, then comes the kaons and the largest signal is observed for the protons. For opposite-charged pairs this difference is large.
Concerning the beam energy dependence of a possible CME towards lower energies there was a beam energy scan performed at RHIC where the STAR collaboration measured the correlators from $\sqrt{s_{NN}} = 62.4\,\text{GeV}$ down to $\sqrt{s_{NN}} = 7.7\,\text{GeV}$ in Au+Au collisions [40]. They choose the transverse momentum range to be $0.15 \leq p_t \leq 2\,\text{GeV/c}$ and applied a DCA cut of $\text{dca} < 2\,\text{cm}$. The results are shown in figure 1.13.
The magnitude of the correlator $\gamma_{\alpha\beta}$ increases in peripheral collisions when the beam energy decreases. Additionaly, the total momentum conservation dominates in peripheral collisions even more with lower beam energies and contributes to the measured signal [41]. Both contributions are calculated with a model and also shown in figure 1.13 by the gray curves. Considering the difference of the same-charge and opposite-charge correlator, i.e. $\gamma_{OS} - \gamma_{SS}$ this difference stays rather constant down to an energy of $\sqrt{s_{NN}} = 19.6\,\text{GeV}$. It has the expected increase towards peripheral collisions due to the change of the magnetic field. At the two lowest beam energies it reaches almost zero ($\gamma_{OS} - \gamma_{SS} \sim 0$). This is exactly what should happened when the QGP is not likely to be formed any longer, especially in the peripheral collisions where the number of participants is the lowest.
From the measurements of the correlator $\delta_{\alpha\beta}$, one can conclude that there are strong background sources, larger than any CME effect (because δ_{OS} is mostly above δ_{SS} which should be opposite in case of CME). These background sources may couple with collective flow which then also leads to contributions to the correlator $\gamma_{\alpha\beta}$.
Summarizing all the previous measurement of the CME observables, there are some indication for the existence of the CME but the situation is not clear since the background sources are not understood yet. Additionaly, the influence of several variables has to be scrutinized. Therefore, a calculation of the two correlators at even lower energies could be helpfull even if the CME does not occur in this energy regime. The possible absence of the CME could be also an advantage to study various background sources in more details which then will help to solve the puzzling situation of a possible local parity violation of the strong interaction. In addition, it is possible that there are other effects ongoing like for example the **C**hiral **V**ortical **E**ffect (for a review see [42]). This effect might be more prominent at lower collision energies.

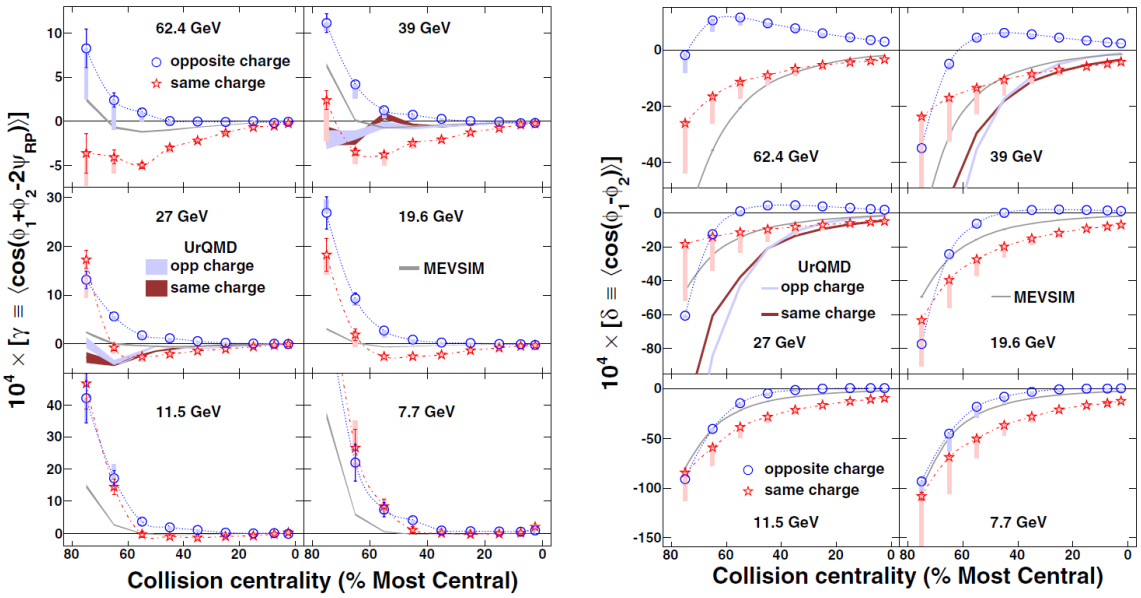

Figure 1.13: The two-particle correlators as a function of centrality for Au+Au collisions at a beam energy $\sqrt{s_{NN}} = 7.7 - 62.4\,\text{GeV}$ measured by the STAR collaboration [40]. Note that the scale on the ordinate is different in each row.

2 High Acceptance Dielectron Spectrometer

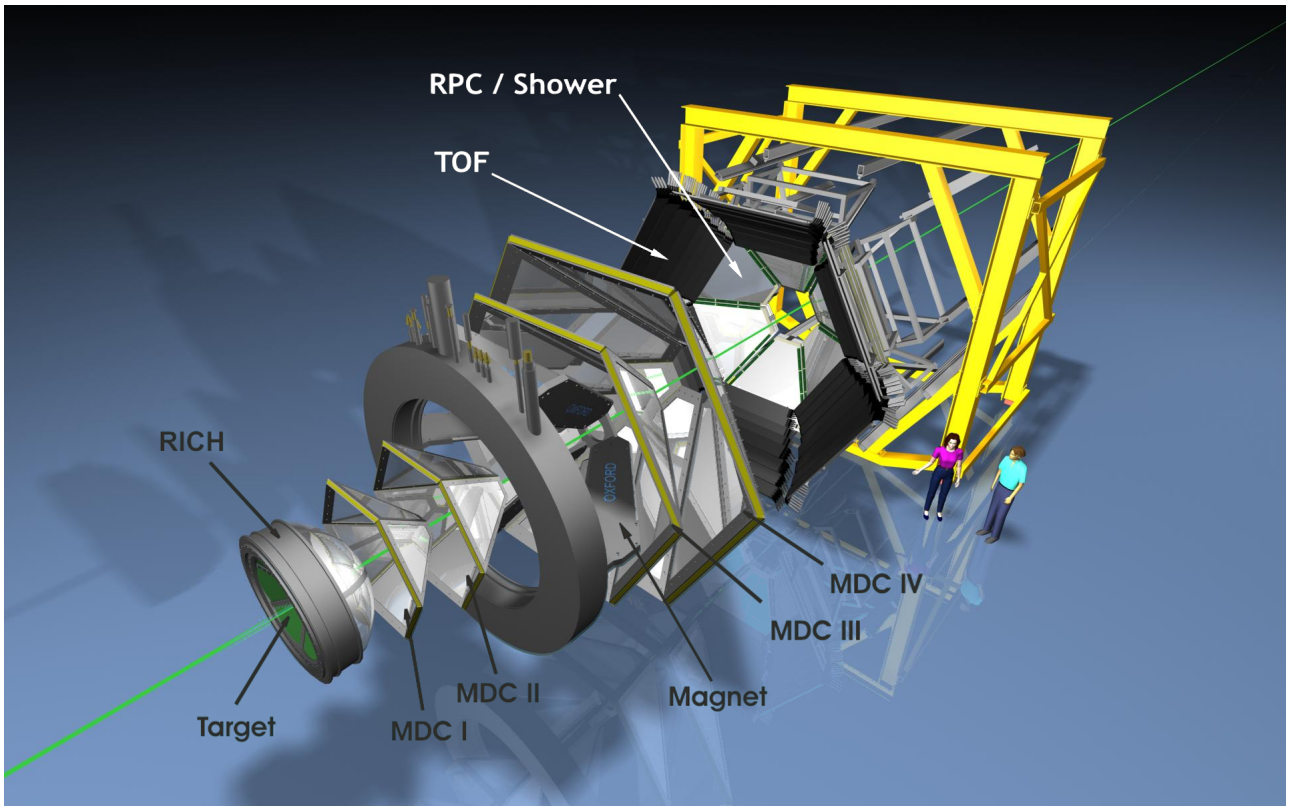

Figure 2.1: Sketch of the HADES spectrometer expanded in z direction. From left to right: RICH detector, two inner MDCs, the magnet, two outer MDCs, the time-of-flight detectors TOF and RPC, Pre-Shower detector.

The **H**igh **A**cceptance **DiE**lectron **S**pectrometer [43] is a fixed target experiment situated at the GSI Helmholtzzentrum für Schwerionenforschung GmbH in Darmstadt (see figure 2.1, 2.2). The intention to built this spectrometer was to measure the light vector mesons ρ, ω and ϕ at low energies of $\sqrt{s} \approx 2-3\,\mathrm{GeV}$ [44]. Having a very short lifetime, the light vector mesons decay inside the fireball into lepton pairs. These dileptons can leave the fireball without strong interaction and thus provide rich information about the medium at various stages of the collisions.
To be able to measure the light vector mesons this results in some essential detector requirements. First of all, the detectors must be fast due to the high intensities delivered by the heavy-ion syncrotron SIS18 up to 10^8 ions/s. These high intensities are needed in order to get enough statistic to measure the decay of the light vector mesons (suppressed by an additional power of α). A high geometrical acceptance is also an advantage, needed because of the large opening angle between e^+e^--pairs especially at low masses ($\leq 1\,\mathrm{GeV}/c^2$). Additionaly, a high mass resolution of $\Delta M/M \approx 1\,\%$ is required in order to measure in-medium modifications of the vector mesons. In addition, the leptons have to be identified with highest possible purity to separate them from the hadronic background. At the end, this results in a very good particle identification for almost all different particle types.
The detector material has to be considered as well. Since one has to deal with high energetic

particles inside the detector they will interact and produce a lot of energetic photons. The photons themself will then convert further to e^+e^--pairs and produce a large background. Hence the detector material has to be chosen in a way to minimize this effects, i.e. to use low budget material. The effect of multiple scattering is minimized aswell.
Therefore, HADES was build with an angular coverage from 18° to 85° in the polar angle θ and almost the full azimuthal angle ϕ. For the dilepton identification the **R**ing **I**manging **CH**erenkov and the Pre-Shower detectors are used. The particle tracks are recontructed using four **M**ultiwire **D**rift-**C**hambers while two of them are placed in front of and two behind the superconducting magnet. For the time-of-flight measurement there where two detectors installed: the **T**ime-**O**f-**F**light detector for large polar angles ($45° < \theta < 85°$) and the **R**esistive **P**late **C**hamber for the inner part ($18° < \theta < 45°$). Having a high geometrical acceptance, a high momentum resolution, precise time-of-flight measurement and specific energy loss in MDC and TOF allows accurate identification of hadrons.

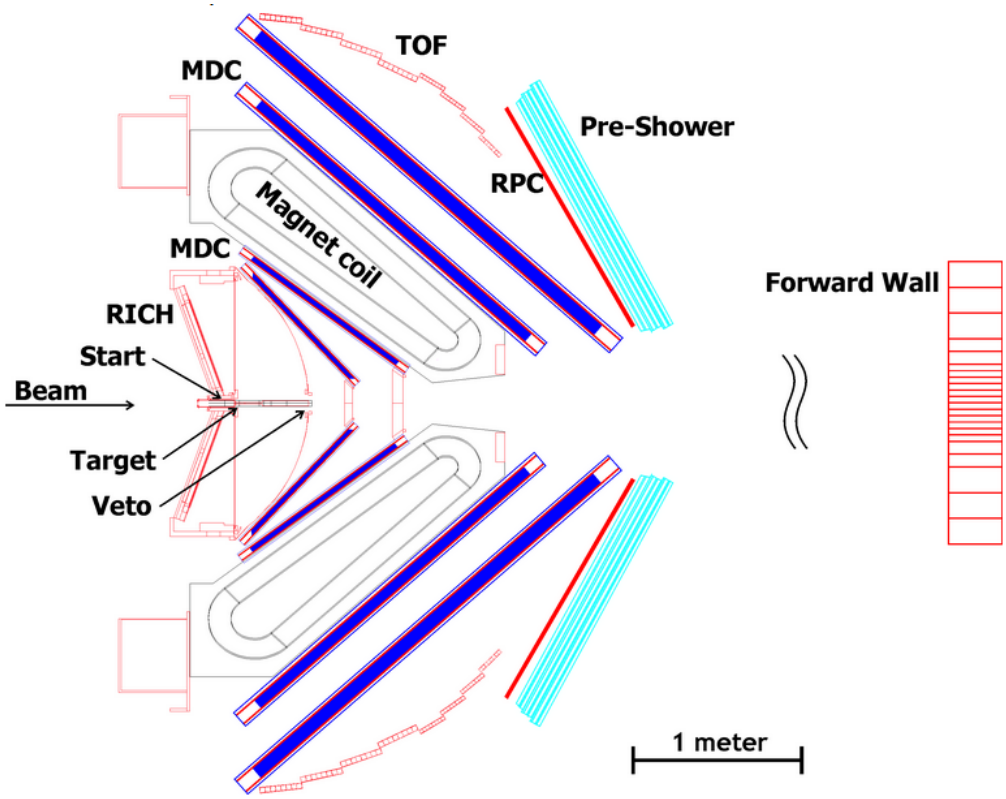

Figure 2.2: Overview of the subsystems of the HADES detector [43].

2.1 START- and VETO-detector

The START- and the VETO-dectector are both diamond based detectors. Since both are placed within the beam line they need to have a very high radiation hardness [45]. The START-detector is the first HADES detector for the beam counting. It is used to measure the time t_0 at which the collision takes place. Additionaly, it monitores the beam quality and can be used as an event-trigger. To use this START detector for the entire beam time, there are 9 segments where the beam can be focused on (see left panel of figure 2.3). The detector or beam could be moved in order to change the current working segment.
The VETO-detector is placed downstream the target and is used in an anti-coincidence measurement with the multiplicity trigger array to exclude collisions which have not taken place inside the target. It allows to remove the most peripheral events and hence can reduce the deadtime for the data taking. For more informations see [46].

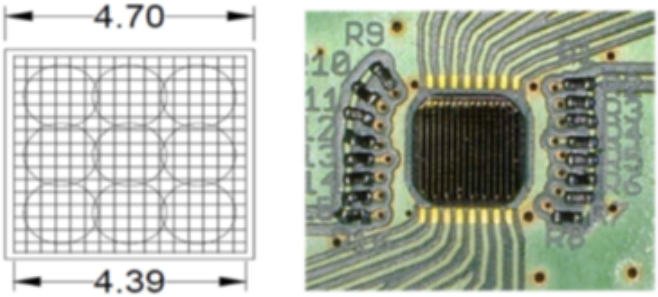

Figure 2.3: The START detector consisting of 16 diamond strips in two planes (right panel). It can be used in 9 different segments into the beam line (left panel) to guarantee the detector to work within the hole beamtime [46].

2.2 The RICH detector

The **R**ing **I**maging **CH**erenkov is the innermost part of HADES used to identify relativistic electrons with momenta $0.1 \leq p \leq 1.5\,\mathrm{GeV/c}$ [43]. A schematic draft of the RICH detector is shown in figure 2.4.
The RICH allows the signals from electrons and positrons to be separated from the hadronic ones. This is done using the Cherenkov effect. When particles travel with very high velocities v trough a medium it could be that their velocities are higher than the speed of light within the medium, i.e. $v > c/n$ where n is the refraction index of the medium. These particles will emit high energetic photons, the so called Cherenkov light. For HADES energies the hadrons are too slow to produce Cherenkov light. Only for a momentum $p > 1.8\,\mathrm{GeV/c}$ there might be muonic background.
The Cherenkov light is emitted in a cone around the particle track. These cones are reflected by a spherical VUV (vacuum ultraviolet) mirror to a photon detector which is placed upstream the target to avoid background from charged particle tracks. The electrons and positrons can then be identified by the rings they produce in the photon detector. Since in this analysis the focus is on hadrons, the RICH does not play a big role. For more informations about the RICH detector see [43], [47], [48].

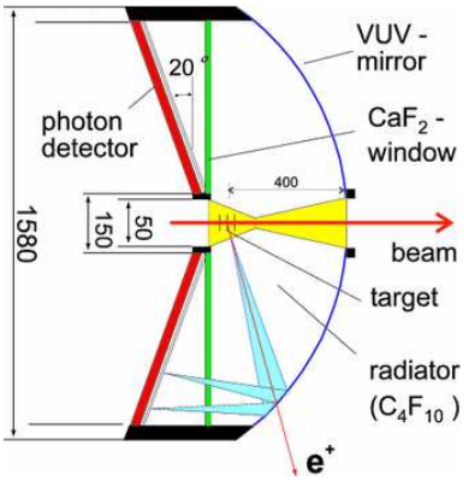

Figure 2.4: Schematic draft of the RICH detector. To illustrate the functioning a positron track is shown along which the Cherenkov light produced along its way. All distances are given in mm [43].

2.3 The tracking system

The HADES tracking system is composed of four planes of **M**ultiwire **D**rift **C**hambers and a superconducting magnet. Two MDCs (MDC I and MDC II) are located in front of the magnet and the other two (MDC III and MDC IV) are placed behind. This allows to reconstruct not only the particle tracks but also observables like momentum and energy loss in the MDC. In general the tracking system must be constructed in a way to guarantee a high spatial resolution of $\sigma < 150\,\mu$m. Therefore, multiple scattering in the detector material but also in between the differents parts must be reduced. Again, a high efficiency is needed as well as a large acceptance.
The MDCs are separated into six sectors[1] and covers an azimuthal angle of 85 %. The polar angle coverage is from 18° to 85°. Each MDC consists of another six chambers. Each chamber has 1100 drift cells starting from $5x5\,\mathrm{m}^2$ for MDC I and increasing to $14x10\mathrm{m}^2$ for MDC IV. The different chambers composed of six layers orientated in different direction by $\pm 0°, \pm 20°, \pm 40°$ to guarantee a maximal spatial resolution in the polar angle θ which is also the direction of the momentum kick (see figure 2.5). The thickness of the inner part of each MDC is only about 3 cm which reduces multiple scattering a lot.
Requiring the full track which means a fitted inner and outer segment and a good momentum reconstruction the efficiency to reconstruct a proton is about 86% [43]. Using a 2.1 GeV/c proton beam a spatial resolution of $\sigma = 68 \pm 5\,\mu$m was gained over $70 - 80$% of the drift cell [49]. The energy loss measurement is performed by the width of the drift time signal (**T**ime **o**ver **T**hreshold) since the MDC does not have analoge-to-digital converters to measure the deposite charge directly.

[1] The separation into six sectors is necessary due to the specific hanger of the superconducting magnet.

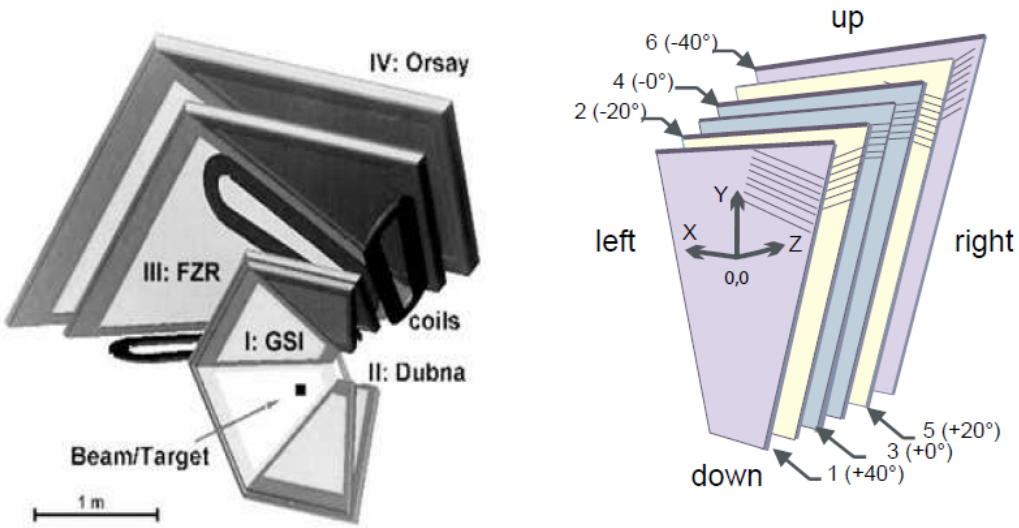

Figure 2.5: Schematic draw of the HADES tracking system. In the left panel the four MDCs are shown with the magnet coils inbetween. In the right panel the six layers per MDC are shown with their different wire orientation [43].

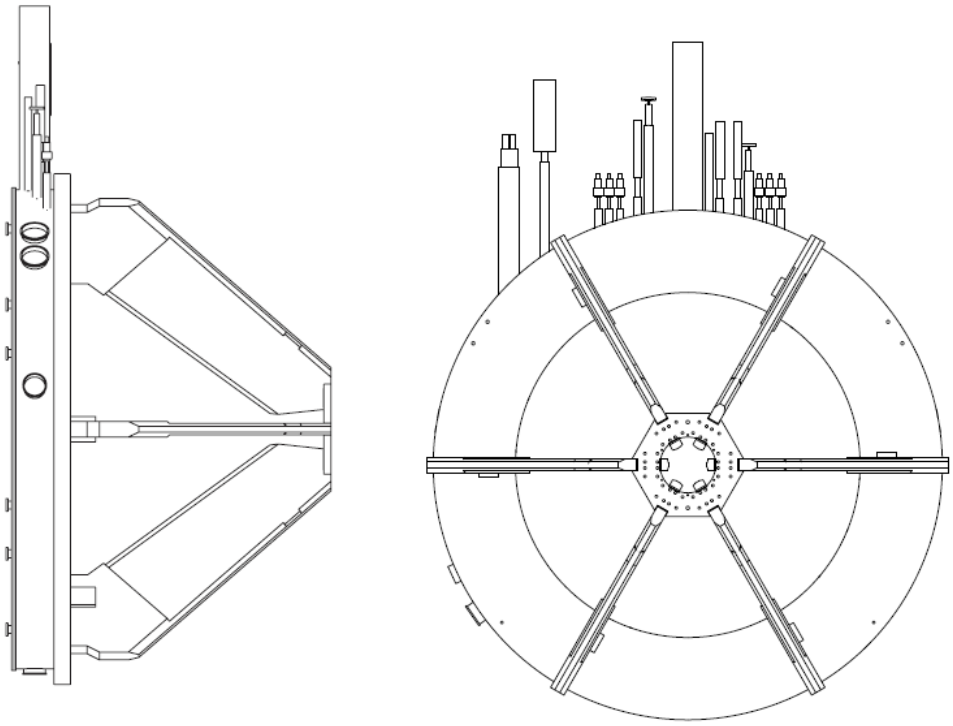

Figure 2.6: Draft of the superconducting magnet with all the hambers. A hexogonal plate with a hole for the beam pipe of 7° and a support ring are needed to compensate the magnetic forces up to $4 \cdot 10^4$ N acting on the coils [43].

The superconducting magnet between the inner and outer MDCs is required to give a kick[2] to the charged particles in order to obtain their momenta. Additional requirements to the magnet are to keep the full spectrometer acceptance which means that all particles should be bended such that they also hit the detectors behind the magnet. In order to not disturb the measurement by the other detectors the magnetic field should be localized and be zero in the area of other detectors (especially for the RICH in order to measure the electron rings without pertubation and to keep the angle between e^+e^- from γ-conversion small).
The choise of a toroidal field geometry provides a field free region in the active region of the RICH detector and also in the target region. The superconducted coils are necessary in order to achieve a compact construction and no furhter loss due to the hambers. The magnet is cooled by a helium gas down to a temperature of 4.7 K. The maximum field strength is about $B_{\max} = 3.6\,\mathrm{T}$ at the sector edges while it drops down to $B = 0.8\,\mathrm{T}$ in the middle of the sectors. A draft of the magnet is shown in figure 2.6.

2.4 Multiplicity trigger array

The multiplicity trigger array (META) consists of the time-of-flight walls and a Pre-Shower detector. It is placed behind the tracking system and provides fast trigger information about the charged particle multiplicity and is also used for particle identification.
In the θ region $45° \leq \theta \leq 85°$ the scintillator time-of-flight wall TOF is placed. Like the tracking system its segmented into six sectors. Each sector consists of eight modules which again consist of eight scintillator rods enclosed in a carbon fiver case [43]. Each rod is made out of plastic scintillator material to guarantee a good light attenuation length, a high scintillation efficiency and a fast response time.
A charged particle with flies through the detector excites atoms and molecules of the detector material which emit photons when they fall back to the ground state. The photons travel with a specific group velocity v_g to both ends of a rod where photomultiplier read out the signal. The arrival times to both ends are given by $t_{\mathrm{left}}, t_{\mathrm{right}}$ (calibrated to the START time) and the amplitudes by $a_{\mathrm{left}}, a_{\mathrm{right}}$. From this observables the time-of-flight t_{tof}, the position along the rod x and the deposited energy ΔE of a particle can be calculated:

$$t_{\mathrm{tof}} = \frac{1}{2}\left(t_{\mathrm{right}} + t_{\mathrm{left}} - \frac{L}{v_g}\right), \tag{2.1}$$

$$x = \frac{1}{2}\left(t_{\mathrm{right}} - t_{\mathrm{right}}\right) v_g, \tag{2.2}$$

$$\Delta E = k\sqrt{a_{\mathrm{right}} a_{\mathrm{left}} e^{L/\lambda_{at}}}. \tag{2.3}$$

Here L is the length of the rod, k is a constant and λ_{at} is the attenuation length. The time-of-flight and the deposite energy can be used for the particle identification. In order to separate electrons from pions up to 0.5 GeV/c and from protons up to 2 GeV/c the TOF has a time resolution of $\sigma_t \approx 150\,\mathrm{ps}$ and a spatial resolution $\sigma_x \approx 25\,\mathrm{mm}$ [50]. The spatial resolution is

[2] The "kick" is not really a kick but a bending of the particles tracks within the magnetic field by the lorentz force $\vec{F}_L = q\vec{v}x\vec{B}$. Its is called "kick" because the particle track is measured as a straight line before and after the particles enters the magnetic field and hence it can be considered as a kick.

determined by the reconstructed track in the MDC projected onto the TOF and comparing this to the measured hit position. The distribution of $x_{\mathrm{TOF}} - x_{\mathrm{MDC}}$ can then be fitted by a Gaussian to obtain σ_x as a parameter from the fit.
The same tasks in the forward direction from 18° to 45° polar angle is realized by the Resistive Plate Chambers. The RPC is segmeted into six sectors of trapezoidal shape (see figure 2.7) and covers a total area of $8\,\mathrm{m}^2$. The RPC is required for measuring a heavy systems like Au+Au since only the high granularity of the RPC allows to measure with sufficient spatial and time resolution ($\sigma_t < 70\,\mathrm{ps}$ [51]).
The RPC consists of two planes with partially overlapping layers of individual shielded RPC cells. A charged particle crossing a cell will ionize the gas mixture between the aluminium electrodes (high voltage of $\sim 5\,\mathrm{kV}$). The free electrons will be accelarated towards the electrode and ionize further atoms causing an electron shower. This electrical signal is measured on both sides of the cell and allows to achieve a particle detection efficiency of $> 95\%$ [51].

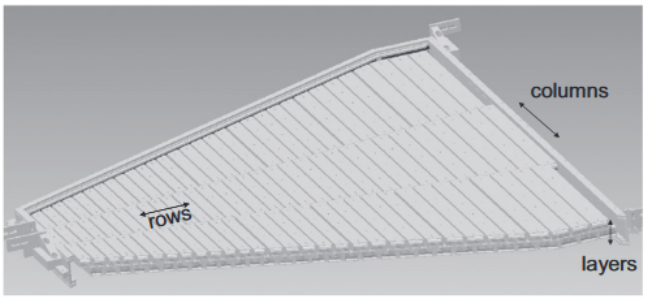

Figure 2.7: Internal structure of the RPC detector [51].

The last part of the META system is the Pre-Shower detector. It is placed directly behing the RPC in the forward direction to improve electron identification. It consists of two lead converters surrounded by three drift-chambers as shown in figure 2.8. To distinguish an electron from a hadron the charge is measured three times within the detector: ones before both converters (pre) and once behind each of them (post1, post2). Since a light particle like an electron has much more interactions with the lead in the converter it produces much more electrons through Bremsstrahlung and pair production processes. Thus the charge difference $Q_{\mathrm{signal}} = Q_{\mathrm{post1}} + Q_{\mathrm{post2}} - Q_{\mathrm{pre}}$ is much larger compare to the one of hadrons.

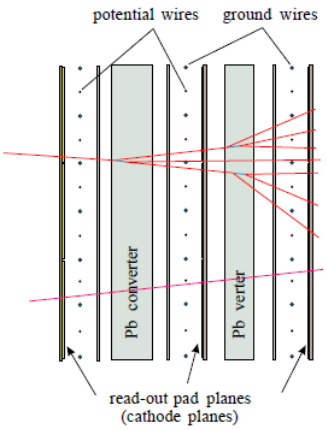

Figure 2.8: Side view of the Pre-Shower detector [52]. The discrimination of a hadron (straight line) compared to an electron (shower) is shown.

2.5 Forward Wall detector

Seven meters downstream the target the Forward Hodoscope Wall (FW) is placed. It is used to measure the spectators of the collision which propagate at the small polar angles $\theta < 7°$.
The FW consists of 288 quadratic scintillators starting from $4 \times 4\,\mathrm{cm}^2$ in the inner most part to an area of $8 \times 8\,\mathrm{cm}^2$ in between and $16 \times 16\,\mathrm{cm}^2$ in the outer part following the track density of the spectators. The cells are connected to photomultiplier tubes to measure the deposite energy of the spectators in each cell. This allows to achieve a resonable angle and position determination of the spectators which is mainly used to reconstruct the reaction plane but can also be used to measure the centrality of a collision. In order to separate the spectators from participants flying to the FW the time-of-flight is also measured. This allows to apply a cut around the spectator particles which fly approximately with the same speed as the incoming ion.

3 Event and track reconstruction

In the following chapters the data collected in April 2012 by HADES is analyzed. In this beam time Au+Au collisions at a kinematic energy of $E_{\text{Beam}} = 1.23\,\text{AGeV}$ [1] were performed. Over 557 hours with a beam intensity of $1.2-1.5 \cdot 10^6$ ions/s a raw data of about 140 TByte has been recorded which corresponds to a total amount of $7.3 \cdot 10^9$ events. The collected data and the amount of days per beam time is shown in figure 3.1 in comparison to the previous beam times of HADES.

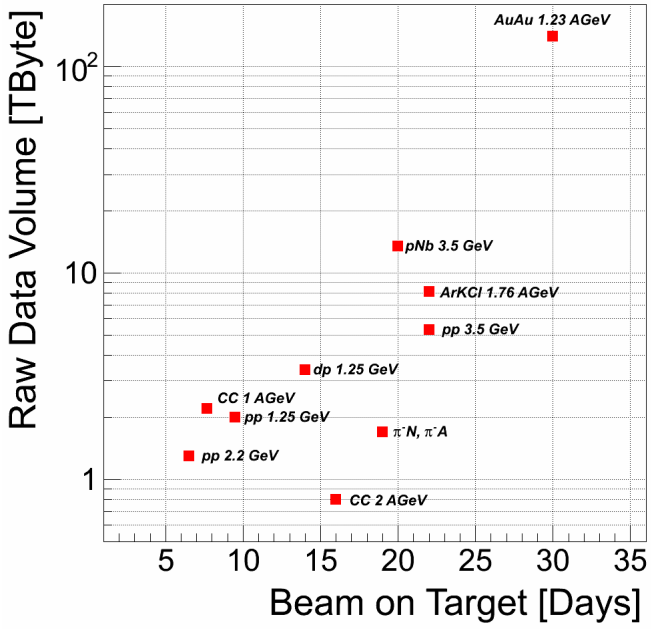

Figure 3.1: Compilation of the raw data collected in the different beam times measured with HADES [53].

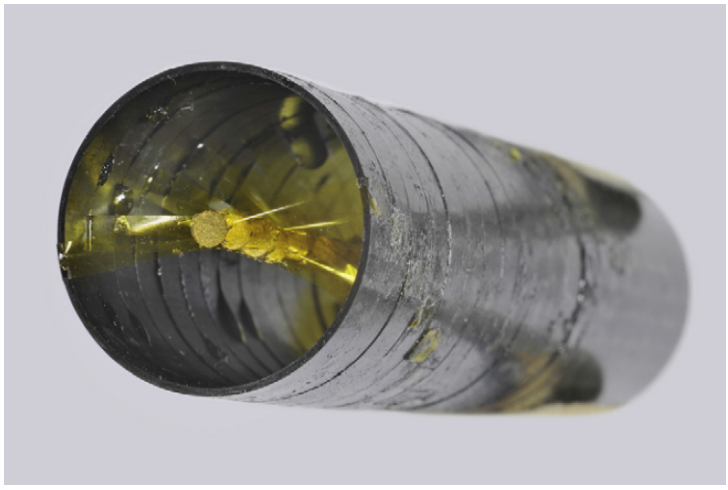

Figure 3.2: Front view of the 15-fold segmented gold target and the carbon target holder tube [54].

The target used during beam time consists of 15 gold foils with a diameter of 2.2 mm and a thickness of 25 μm per gold disk [54]. The distance between two foils is about 4 mm which leads to an overall target length of 54.5 mm (see figure 3.2). The special design of the target is necessary in order to keep the γ-conversion probability as low as possible.

3.1 Event recording

Considering the very high multiplicities in heavy-ion collisions a trigger system is needed in order to do a fast online event selection and directly remove non-physical events to reduce the detector dead time and keep data storage as low as possible. Therefore, a minimum multiplicity of 5 hits in the TOF detector[2] is required. The choise to store an event or to skip it is taken in

[1] This corresponds to a center-of-mass energy of $\sqrt{s_{NN}} = 2.42\,\text{GeV}$ and a center-of-mass rapidity of $y_{\text{mid}} = 0.74$.

[2] These events are only stored when the TOF signal is in coincidence with the START detector.

$\sim$ 100 ns time window which is much less than the mean time between two collisions [55]. The most peripheral events with 5−20 hits in TOF are stored with the **P**hysical **T**rigger 2 (PT2) while events with $>$ 20 TOF hits are stored with PT3. Since the amount of PT2 events is large and the focus is on the more central events (PT3) only each eighth PT2 event is stored. The selected events are then written into **H**ades **L**ist **D**ata files (HDL). From these HDL files information provided by each detector is unpacked. Once physical information of each hit is available a tracking algorithm reconstructs the informations provided by the single detectors to possible particle tracks, called particle candidate. The parameters for the quality of the reconstruction but also the physical observables of this track are then stored in a **D**ata **S**ummary **T**ape (DST). Informations about the parameters of all detectors are stored in the Oracle data base in order to be able to check for detector performance and calibration afterwards.

3.2 Track reconstruction

In order to come from events to single particle tracks the informations of different detectors have to be combined together (for more details see [43]). The reconstruction of the particle trajectories is done with the tracking system. First of all, the hit position in each MDC plane has to be found. A single particle crossing the wires will induce an electrical signal. This drift cell is called fired. For the track candidate search all fired drift cells are projected onto a common projection plane to find the position of the maxima. The projection planes for the inner and outer part of the MDC are shown in figure 3.3.

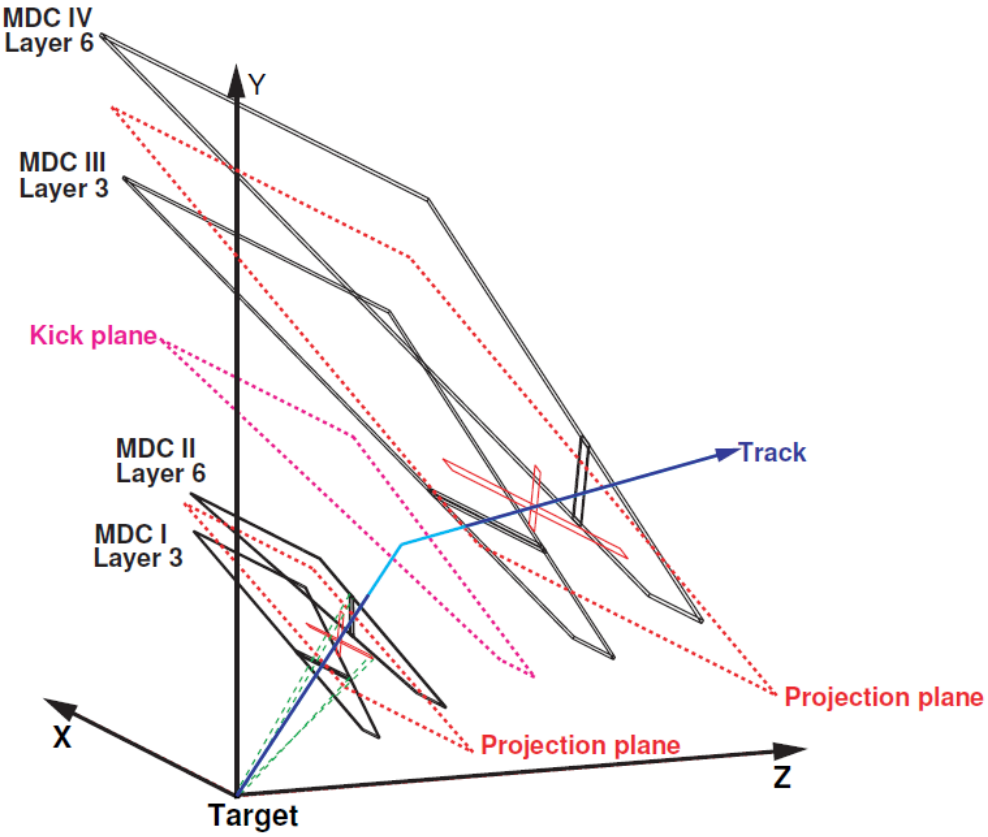

Figure 3.3: Sketch of how the search for the track candidates is done. For simplicity, only one layer of each MDC is shown [43].

The result of this projection is a two-dimensional histogram showing a local maximum where the particle crosses the drift chamber (see figure 3.4). This maximum is called wire cluster and all clusters of one event are projected simuntaneously onto one plane. With this, the amount of fake tracks in each event can be reduced by setting a certain threshold of fired wires which changes dynamically with respect to the total amount of fired wires. The remaining wire clusters are combined with respect to the event vertex by a χ^2-minimization method resulting in straight lines for the inner segment of the MDC (for a detailed describtion of the procedure see [43]). The value of χ^2_{inner} can be used in the analysis to choose the best track candidates.
From the inner segment track one has to describe the particle deflection in the magnetic field in order to combine this track to the corresponding one in the outer MDCs. This deflection is considered to be momentum kick in a certain kick plane (see figure 3.3). Hence, from the inner track one has to calculate the intersection point with the kick plane. Then the same procedure is performed for the outer MDCs but replacing the target position by the kick plane point and taking into account the directive change through the momentum kick. This gives again a χ^2_{outer} as a measure of the track segment quality. This inherent matching of inner and outer track segment results in the so called track candidate. To get a complete particle track the track candidates have to be combined with the META hits. Therefore, the calculated trajectories from the Runge-Kutta method (see next section) are extrapolated to the META detector. The distance of the extrapolated hit points to the matches META hit are given by dx, dy. The META match quality metaQA is used as a measure of how good a track is matched to TOF or RPC:

$$\text{metaQa} = \frac{dx}{\sigma_x}, \tag{3.1}$$

where σ_x is the error of the measurement. The y-direction is not used since a diviation in y would lead to a hit in a different rod/cell in the TOF/RPC detector.

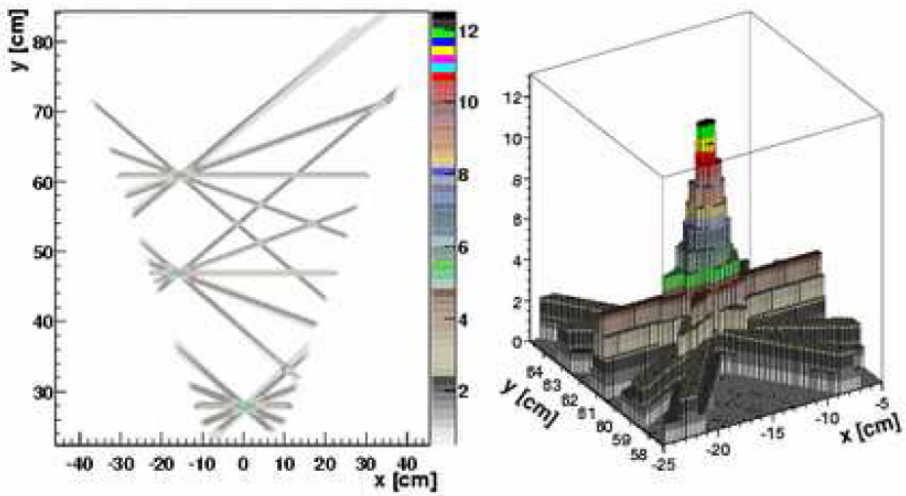

Figure 3.4: Principle of the wire cluster finding procedure [43]. In the left panel, the projection plane is shown with several wire cluster. By eye they can be easely separated from the cluster which are not corresponding to real tracks (by the amount of wires crossing). In the right panel, one local maximum is shown having 12 hit layers. By setting a certain threshold fake tracks can be removed.

3.3 Momentum reconstruction

In order to get a fast estimate for the charged particle deflection inside the magnetic field the kick plane method is used. A charged particle travelling through the magnetic field will be deflected by the Lorentz force $\vec{F}_L = q\,\vec{v} \times \vec{B}$. In the kick plane method this deflection is assumed to be a single kick in a two-dimensional virtual plane combining two straight track segments from the inner and outer MDCs. The momentum kick $|\Delta\vec{p}_k|$ can then be calculated from the deflection angle $\Delta\theta_k$ by

$$|\Delta\vec{p}_k| = |\vec{p}_{\text{in}} - \vec{p}_{\text{out}}| = 2p\sin(\Delta\theta_k/2), \tag{3.2}$$

where $p = |\vec{p}_{\text{in}}| = |\vec{p}_{\text{out}}|$ is the magnitude of the momentum. Using the fact that the momentum deflection is described by the time intergral over the Lorentz force and performing a Taylor expansion (for details see [43]) the particle momentum is determined by

$$p \approx \frac{1}{2}\frac{p_{k0}}{\sin(\Delta\theta_k)} + p_{k1} + 2p_{k2}\sin(\Delta\theta_k), \tag{3.3}$$

where all parameters p_{k0}, p_{k1}, p_{k2} depend only on the entry and exit points of the particle track inside the magnetic field. This method gives a fast estimate of the particle momentum but since the precision of the kick plane method is not sufficient this method is not used for data production.
For the data production the Runge-Kutta method is used. Yet for a successfull operation resonable starting values are required. Therefore, the spline method is applied first to get a good estimation for the particle momentum and polarity.
In the spline method the particle trajectory inside the magnetic field is approximated by a cubic spline. Hence, the deflection is no longer a "kick" but a smooth curve as shown in figure 3.5. The interpolation is starting from the hit in MDC II and ends exactly at the hit point in MDC III. Thus the method needs the track candidates as an input. The interpolation is done by setting 50 equally-spaced points and calculating the momentum in each point using also the HADES magnetic field map. The particle momentum is obtained by averaging over all points. This yields already to a relative momentum resolution σ_p/p of a few percent.
To further improve the momentum determination the Runge-Kutta method is used [43]. The best momentum reconstruction is achieved when solving directly the equations of motion. In the RK method this is done numerically. The solution for the starting point is extrapolated to the following track point and so on. The quality of the trajectory is given by χ^2_{RK}. Energy loss and multiple scattering of the particle are not taken into account by this method but for the low material budget the typical error is below 0.5 % radiation length.

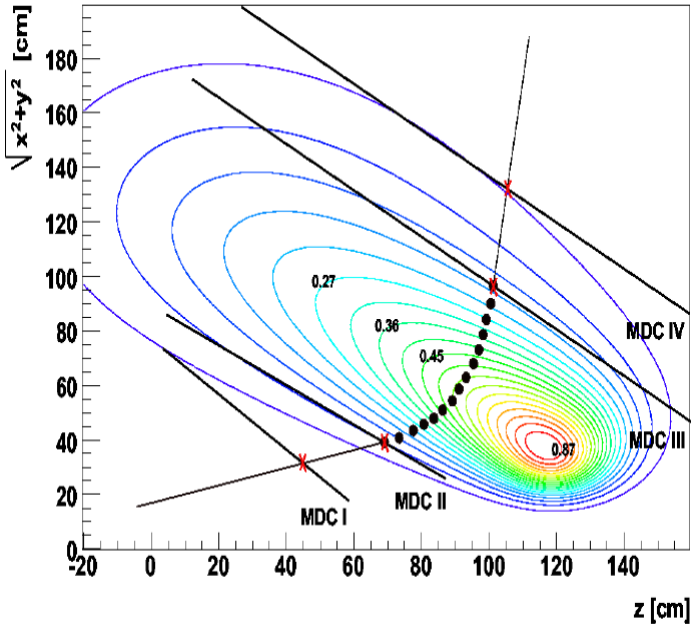

Figure 3.5: Example of how the spline method interpolates the particle trajectory between the inner and outer track segment. The contour plot shows the main component of the magnetic field at an azimuthal angle of $\phi = 90°$ [43].

3.4 Reaction Plane reconstruction

As pointed out in section 1.5 it is necessary to know the reaction plane of each collision in order to be able to study the relative particle motion. The reaction plane of a collision is estimated by the so called **E**vent **P**lane (EP) which is reconstructed in experiment. In HADES this reconstruction is done with the Forward Hodoscope Wall by a **Q**-vector analysis [56].
In each collisions there are the so called spectators which are not participating in the collision. Hence, they fly relatively undisturbed towards the FW. The spectators have a certain transverse momentum distribution in the plane perpendicular to the beam axis. Therefore, they will hit a given FW cells corresponding to their transverse momentum. As a results they deposite a specific amount of energy in this particular FW cell depending on their energy and particle type. The **Q**-vector is then defined by the sum of the unit vectors from the beamline to the FW hit position by

$$\vec{Q} = \sum_{i=1}^{N_{sp}} w_i \frac{\vec{r}_i}{|\vec{r}_i|}, \tag{3.4}$$

where N_{sp} is the number of spectators and $\vec{r}_i$ is the position vector of the cell with a hit of particle i. To acount for the different particle types the sum is weighted by a factor w_i which is set to the particle charge $|Z|$ of the spectator. Additionaly the weights are chosen to be $w_i > 0$ for forward flying while $w_i < 0$ in case of backward flying particles[3].
Due to acceptance correlations from an imperfect detector the distribution of Ψ_{EP} is anisotropic.

[3] Forward flying particles means that their rapidity is larger than the midrapidity, i.e. $y_{\text{spectator}} > y_{\text{mid}}$ and the other way around for particles flying in backward rapidity.

Therefore, the event plane angles have to be reweighted in order to get a flat distribution. To do so, the Ψ_{EP}-distribution for different multiplicities is fitted by

$$\frac{1}{N}\frac{dN}{d\Psi_{EP}} \approx 1 + 2c_1\cos(\Psi_{EP}) + 2\cos(2\Psi_{EP}) + c_3\sin(\Psi_{EP}). \tag{3.5}$$

Then the event plane angles are weighted by the correction factor obtained from the fit in order to get an isotropic distribution.
As a measure for the quality of the reconstructed event plane each event is randomly devided into two subevents A and B of equal size. For both subevents the event plane is reconstructed seperately. The distribution of $\Psi_A - \Psi_B$ can then be used to calculate the event plane resolution. Afterwords the observables depending on the EP are corrected for the finite resolution as described in section 5.1.

4 Event and particle selection

For the analysis the **H**ADES s**y**stem for **d**ata **r**eduction and **a**nalysis (HYDRA) is used [57]. It is based on the object orientated software ROOT [58] developped at CERN to deal with the analysis of large scale data. Concerning the HADES data, the analysis is based on the eighth generation of data production. For the simulations, the UrQMD transport model is used [16], [17], [18]. The physical processes from the collision to the kinematical freeze-out are included. Afterwards, the particle propagation through the detector is simulated by the package **H**ADES **GE**ometry **AN**d **T**racking (HGEANT). HGEANT is based on the software GEANT 3.21 [59] also developped at CERN. This allows to study detector performance based on the simulated data by comparing both informations, the real (simulated) particles and the reconstructed ones.

4.1 Event selection

The selection of the events used in the analysis is crutial. The informations from different detectors have to be combined to remove non-physical events. First of all, one has to make sure that the event vertex is inside the target. Collisions of the beam ions with the START detector or the target holder have to be removed. When two events happened in a too narrow time window there will be more particles registered leading to bias on collision time, centrality determination and on the observables based on these quantities, i.e. the time-of-flight. Those events are called pile-up events.
In this analysis only one day of the beam time is analyzed. This is due to the fact that not all six sectors of the MDC have been working properly during the whole beam time. Since the azimuthal particle distribution is studied a missing sector would have a large impact on the results which one would have to correct for. This is not done yet. Therefore, only data files are used where all six sectors are working properly.
As a first step of the analysis, the so called "standard event selection" is applied. This includes the following requirements:

- **GoodTrigger**: the number of hits in the TOF detector is above 20 which is equivalent to the multiplicity trigger PT3 (see previous section).
- **GoodStart**: there is a hit in the START detector to allow for time-of-flight measurement.
- **NoPileUpStart**: within a time window of from -5 to 15 ns around the collision time there is only one hit in the START detector. This removes the pile-up events discussed before.
- **GoodVertexClust**: the reconstruction of the event vertex can be done by at least one track and the χ^2 of the vertex reconstruction is greater than zero. The vertex position is $r_{\text{vertex}} \leq 4\,\text{mm}$ in the xy-plane, while r_{vertex} is the distance from the beamline, and $-65 < z < 0\,\text{mm}$ along the beam axis.
- **GoodVertexCand**: the same requirements for the event vertex as for GoodVertexClust are applied but the reconstruction is done by at least two identified particles.

- **NoVeto**: there is no hit in the VETO detector in a time window of ±10 ns around the START signal, since if there is a reaction inside the target, there should be no VETO hit at all.

- **GoodStartVeto**: from 15 to 350 ns after the START hit there is no second START hit which is uncorrelated to the VETO detector. This is to avoid detector bias from a second event.

- **GoodStartMeta**: no second START hit from 80 to 350 ns which is correlated to the META detectors. This is to avoid wrong multiplicities by particles from the second event having un-physical time-of-flight measurements.

To determine the centrality of a collision the Glauber model is used [13]. The measured charged particle multiplicity by the META detector is fitted by the Glauber model to obtain the percentile of the total cross section. Therefore, it is assumed that there is a monotonic behavior between the charged particle multiplicity N_{charged} and the number of participants N_{part}. This assumption was tested in [14] and is fullfilled with good precision. From the fit of the charged particle multiplicity this can be translated into the impact parameter b. From this distribution the percentile of the total cross section is calculated. The results are summarized in table 4.1.

Multiplicity bin	b_{max}[fm]	META hits	Centrality [%]
0	4.6	160 – 250	0-10
1	6.5	121 – 159	10-20
2	7.95	88 – 120	20-30
3	9.18	60 – 87	30-40
4	18	0 – 59	40-100

Table 4.1: Definition of the different centrality classes as a function of the hits in the META detector and the corresponding maximum impact parameter.

The multiplicity distributions as a function of the number of META hits and also as a function of the reconstructed particle candidates are shown in figure 4.1. The black curve shows the raw spectrum, while the red curve is after the standard event selection and the blue curve after the full event selection. Clearly visible peak structure at ∼ 20 META hits is due to PT2 trigger events. These are removed by requirering the PT3 trigger condition. Further event selection does only a small change to the shape of the distribution. Comparing the red and the blue curve, the difference in the lower part comes from the requirement that only events within the centrality range of 0 – 40 % are analyzed. The little loss of events with high multiplicity comes from the requirement of at least 3 hits in each subsystem in the FW. This cut has to be applied in order to remove events where the reconstruction of the reaction plane has a bad resolution. In the most central collisions most of the particles are flying through the tracking system and hit the META detector afterwards. This means that if the multiplicity in the META detector or the number of reconstructed particle candidates is high, only a small amount of particles travel towards the FW. Hence the number of particles to recontruct the reaction plane is small leading to bad event plane resolutions.

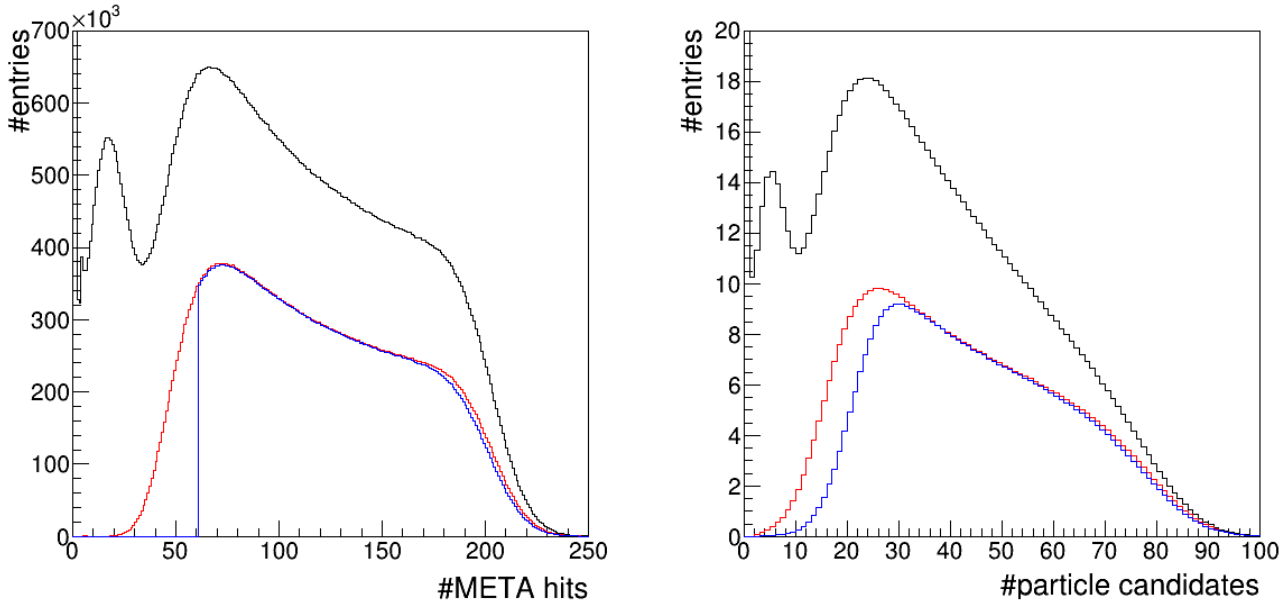

Figure 4.1: Multiplicity distributions for different event selection: The raw distribution directly from the DSTs (black), the distribution with the standard event selection of the eighth generation (red) and the final distribution after the full event selection (blue) are shown. Left panel: Multiplicity distribution as a function of the hits in the META detectors. Right panel: Multiplicity distribution as a function of the reconstructed particle candidates.

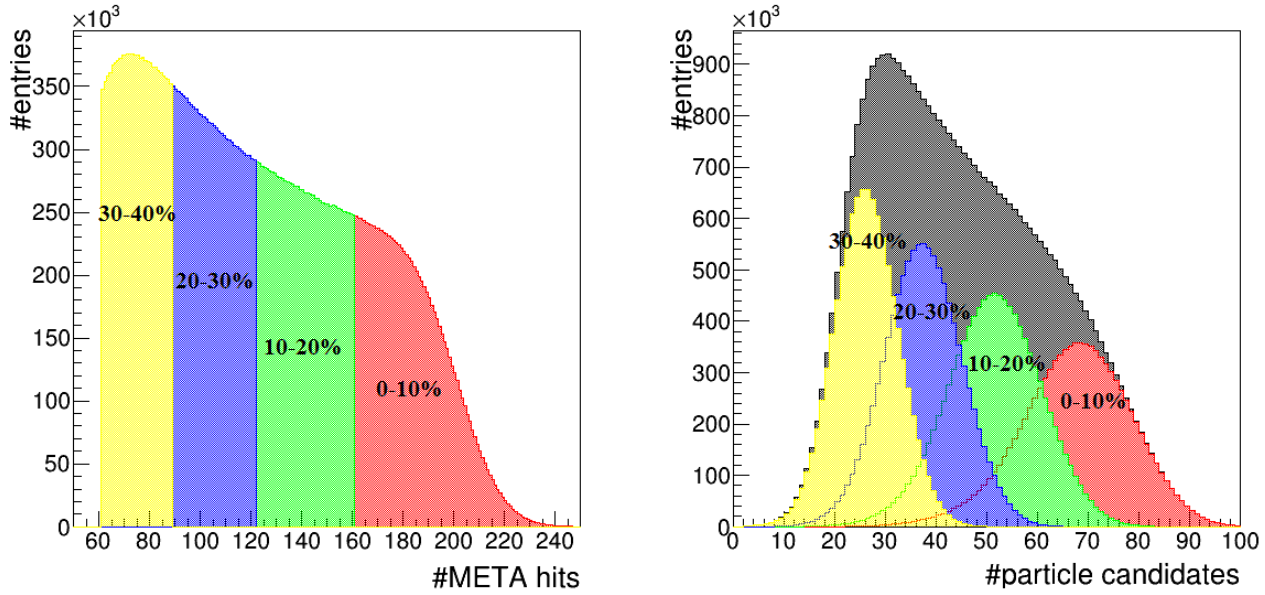

Figure 4.2: Contribution from the different centrality bins to the total multiplicity distribution after full event selection. Left panel: Multiplicity distribution as a function of the hits in the META detectors. Right panel: Multiplicity distribution as a function of the reconstructed particle candidates.

In figure 4.2 the final multiplicity distributions after the full event selection are shown. Additionally, the single contributions from the 10 % centrality bins are shown. Since the centrality is defined by the multiplicity distribution of the META hits the different centrality bins are clearly separated from each other (left panel). Looking to the distribution of the particle candidates the contributions long tails and overlap. For example there are central events where only 40 particle candidates are reconstructed while the number of META hits is at least 160 for this centrality bin. A reason for that could be the efficiency loss in the reconstruction procedure if most of the particles fly close together leading to an overshouting in the wires of the MDCs.
Another cut on the vertex position has been applied: $-60 < z_{\text{vertex}}[\text{mm}] < 0$. The distribution of the reconstructed event vertex in the direction of the beamline and in the XY-plane perpendicular to the beam are shown in figure 4.3 (left panel). In the vertex-z-distribution the 15 segmented target can be seen by the 15 peaks in the area from $z_{\text{vertex}} = -60\,\text{mm}$ to $z_{\text{vertex}} = 0\,\text{mm}$ (see figure 4.3, right panel). From the initial distribution (black) the large contribution of reconstructed events not coming from the target is clearly visible. Especially the peak at around $z_{\text{vertex}} \approx -80\,\text{mm}$. These are mainly gold on carbon reactions happening in the START detector. By the standard event selection these events are removed as can be seen by the red curve. The loss of events in the target region can be explained by collisions with the target holder. The additional cut on the distribution is included in the blue curve. Mainly events are removed which are not originated in one of the targets. Even if there are events removed from each peak of the target, it is good to see that the tails between them decrease substantialy.

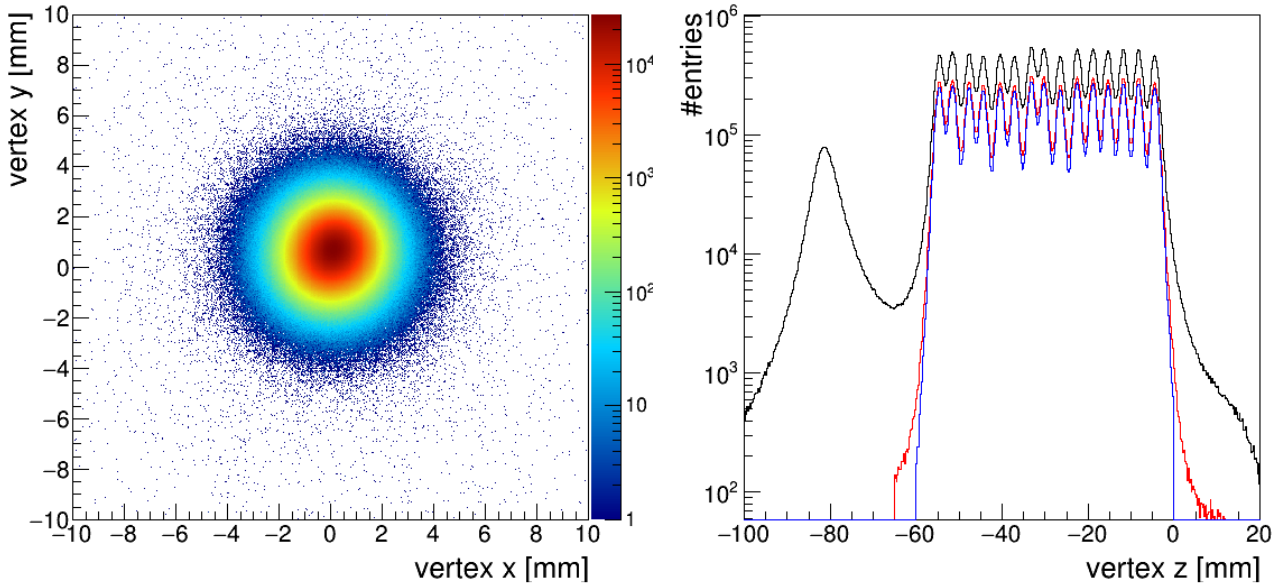

Figure 4.3: Distribution of the reconstructed event vertex. Left panel: The final distribution in the XY-plane perpendicular to the beam axis. Right panel: As a function of the position along the beamline. The raw measured spectra (black), the spectra with the standard event selection of the eighth generation (red) and the final spectra with the full event selection (blue) are shown.

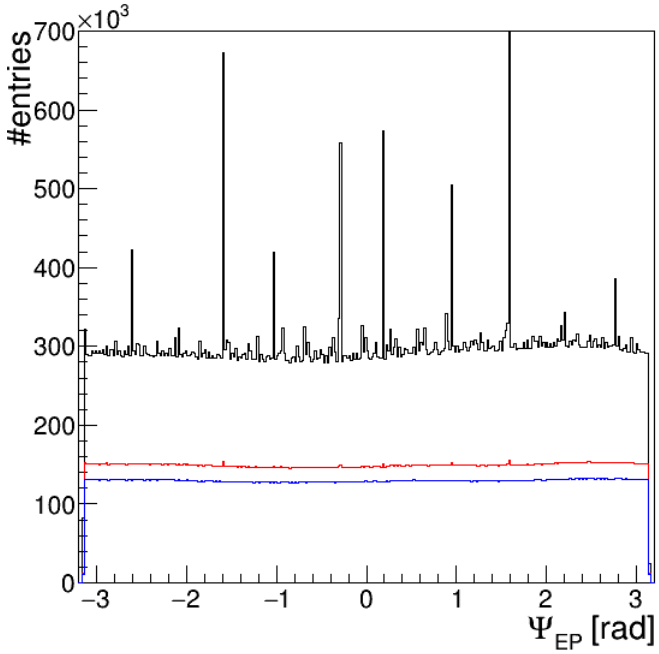

Figure 4.4: Distribution of the reconstructed event plane. The raw distribution directly from the DSTs (black) has large peaks corresponding to pile-up events. They are removed by the standard event selection (red curve). The requirement of a resonable event plane resolution also removes the remaining peaks leading to a flat distribution with less than 5 % of variation (blue curve).

The distribution of the reconstructed event plane (figure 4.4) has a peaky shape when no event selection is applied. The pile-up events are removed by the standard event selection resulting in a flattened distribution with $\Delta N_{\mathrm{EP}} = (N_{\mathrm{EP,max}} - N_{\mathrm{EP,min}})/\langle N_{\mathrm{EP}}\rangle < 7\,\%$ of variation (red curve). But there are still peaks remain originating from events with bad EP resolution. By the requirement of at least 3 hits in each subsystem in the FW these events are also removed. Finally the distribution is flat with a variation $\Delta N_{\mathrm{EP}} < 5\,\%$.
The profiles[1] of the event plane angles as a function of the total charge deposite in the FW are shown in figure 4.5, the result shows a clear multiplicity dependence. The central events are situated where only little charge is deposite in the FW. Towards more peripheral events there is a bump in the distribution. For very high charges the fragmentation is visible where more and more heavy fragments hit the FW consisting of a lot of protons. Yet compared to single protons the charge deposite by a heavy fragment is much less and so the reconstruction of the event plane angle gets worse.
Starting from the events passing through the trigger condition PT3 (100 %) the full event selection reduces the number of events by 53 %. The contribution from each criteria to this number is shown in figure 4.6. The standard event selection of generation eigth removes already 44 % of the events. Since only one day of the beam time is used the requirement of six sectors operating only removes a few files and has not that much influence. This would be completely different when running the whole statistics but to save computational resources this is not useful to do. Interesting is that after all these cuts there are still around 7 % of events which have a centrality

[1] A profile of a function f(x) simply means the average over all particles P and over all events E: $\langle f(x)\rangle = \langle\langle f(x)\rangle_P\rangle_E$.

$> 40\,\%$. This is remarkable, since the PT3 requires already 20 hits in the TOF detector which covers the large polar angles. Looking to table 4.1 this means that there can only be $59-20 = 39$ additional hits in the META system. This is quite unlikely if one takes into account the typical particle distribution with respect to the polar angle θ. Nevertheless, after the centrality cut these events are removed.
The latter two cuts remove only little statistics but as discussed before especially the FW selection criteria improves the quality of the data a lot. Finally, $N_{\text{sel}} \approx 4.08 \cdot 10^7$events go to the analysis which is enough statistics to get a first look to the two-particle correlations.

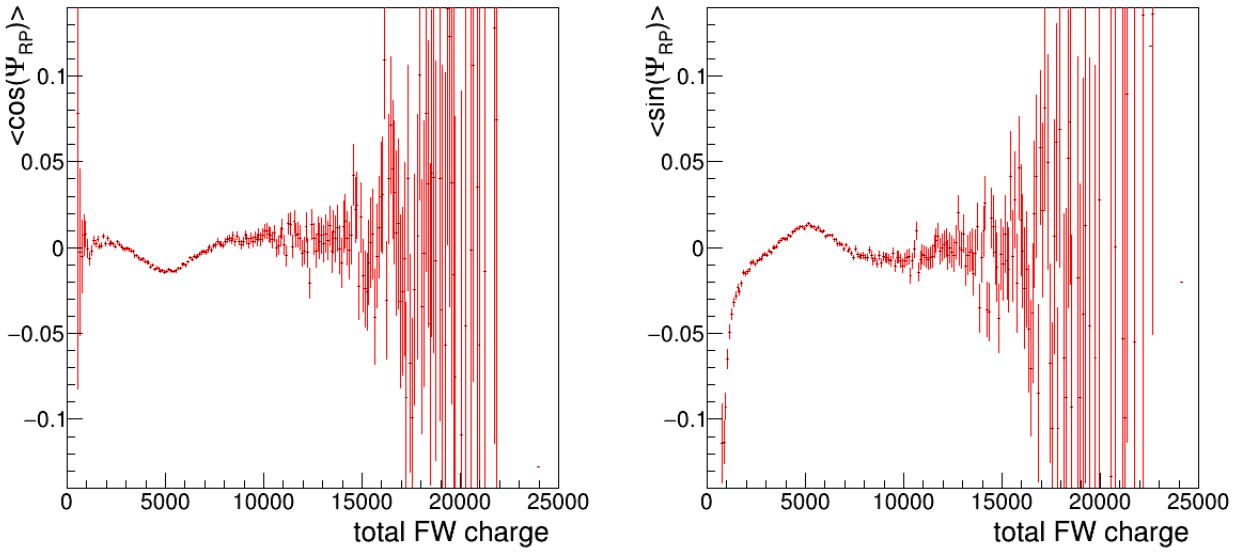

Figure 4.5: Profile of $\cos(\Psi_{EP})$ (left panel) and $\sin(\Psi_{EP})$ (right panel) as a function of the total charge deposite in the FW. The reconstructed event plane has a multiplicity dependence since the shape is not constantly lying at zero.

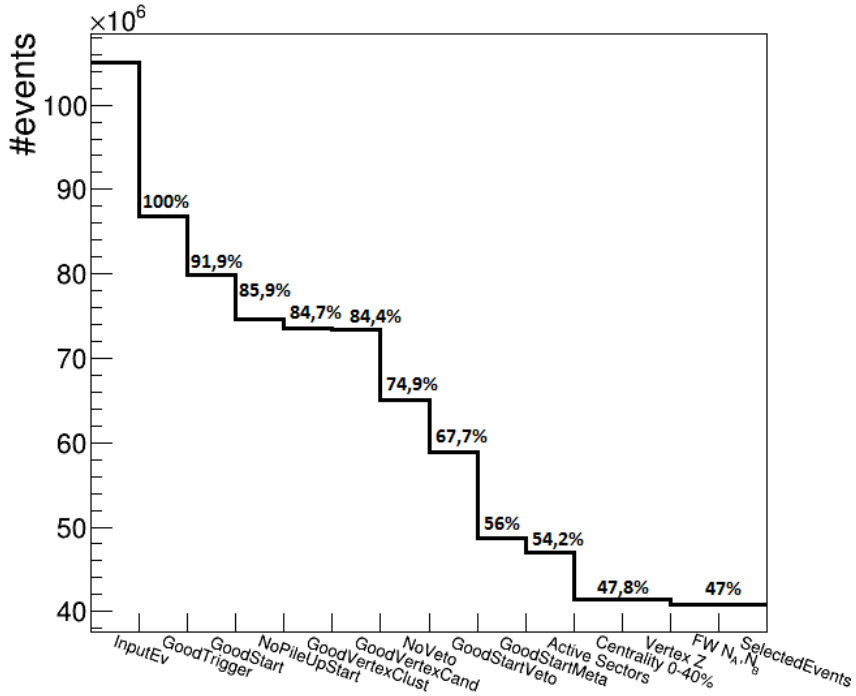

Figure 4.6: Number of events after each criteria of the event selection. Starting from the events within the PT3 trigger (GoodTrigger); the requirement of a START hit (GoodStart); no second START hit within -5 to 15 ns (NoPileUpStart); a good reconstruction of the event vertex (GoodVertexClust, GoodVertexCand); no VETO hit ± 10 ns around the START signal (NoVeto); no second START hit $15-350$ ns after start time with no VETO hit (GoodStartVeto); no second START hit after $80-350$ ns correlated with META hits (GoodStartMeta); all 6 sectors operating under good conditions (Active Sectors); only the most central event $0-40\,\%$ (Centrality $0-40\,\%$); event vertex within $-60 < z_{\text{vertex}}[\text{mm}] < 0$ (Vertex Z); at least three hits in each subsystem of the FW (FW N_A, N_B); the number of events entering the analysis.

4.2 Particle Candidate Selection

The matching of the track candidates to the META hits results in a large amount of possible particles candidates. Each track after candidate selection procedure must have a fitted inner and outer segment but also a META hit. First of all the track quality should be resonable, this is achieved by the cut on $\chi^2_{\text{inner}} > 0$ and $\chi^2_{\text{RK}} < 1000$. Than the deviation of the extrapolated track and a META hit must be < 4 mm in the y-direction and $< 3\,\sigma$ in the x-direction. Tracks where the momentum reconstruction failed , i.e. $p < 0$, are also removed. Another selection is done by the measured time-of-flight in the META detector. It is required that the time-of-flight $t_{\text{TOF}} < 60$ ns and the calculated velocity β of the particle is greater than zero too.
These are the general requirements which have to be fullfilled by a track in order to be considered as a particle candidate. Nevertheless, the combination of inner segment, outer segment and META hit is not unique. It can be that two tracks share the same META hit and so on. For sure the amount of wrongly matched tracks is highest in the most central collisions where most tracks are measured. There can be a lot of possible combinations leading to wrong time-of-flight

measurements, wrong momentum reconstruction and so on, while the error is largest when the track segments of two different particle types are combined. Therefore, the set of tracks in each event has been chosen in a way that the probability of the best track matching is at maximum. This procedure is called track sorting and the sorting of tracks sharing segments or META hits is done by χ^2_{RK}. To ensure that each track is unique only the best track quality is used. All other tracks, which share part of the track that has been chosen are removed from the analysis.
A comparison by the number of intersection points of reconstructed track between data and simulation showed a large difference at the edges of all four MDC planes [60]. In data there are less tracks reconstructed in this region pointing to a systematic efficiency loss. Therefore, these crutial regions of the MDC are discarded from the analysis as can be seen in figure 4.7.

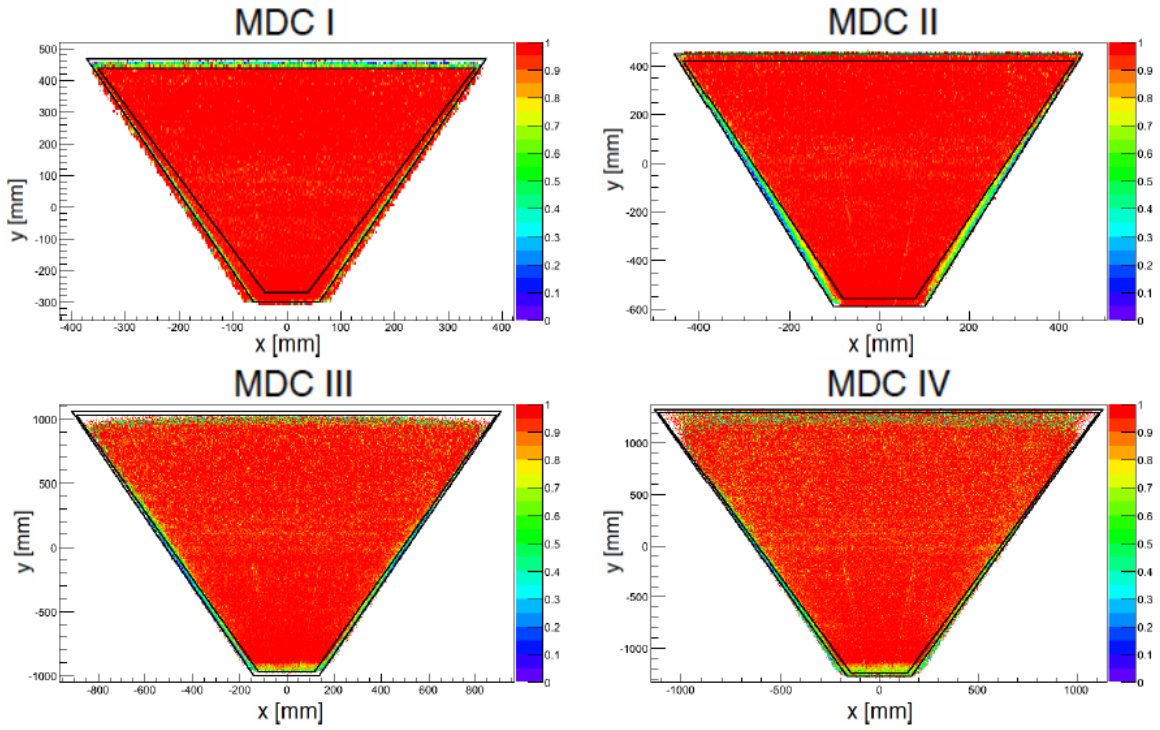

Figure 4.7: In the xy-plane the MDC drift chambers having the layer orientation of 40° for all four MDCs. The histogram is filled in the z-dimension by the number of intersection points of reconstructed tracks in data divided by the simulations. Due to the disagreement between data and simulation at the edges of the MDCs, these tracks are removed from the analysis (black boxes) [60].

4.3 Particle Identification

The main observables used for the identification of the particles are the velocity β, the momentum p, the charge q and the energy loss in the drift chamber dE/dx_{MDC}. The momentum and the particle charge are obtained from the deflection of the reconstructed track inside the magnetic field. The energy loss can be estimated from the signal induced to the wires of the drift chambers. The velocity is obtained from the time-of-flight measurement: beginning with the START hit at t_{START} the particle travels a well known distance Δs [2] until it hits the META

[2] The distance can be directly calculated from the reconstructed particle track.

detector at t_{META}. Hence, the particle needs the time $\Delta t = t_{\mathrm{META}} - t_{\mathrm{START}}$ to travel the distance Δs. And thus the velocity $\beta = v/c$ can be calculated by

$$\beta = \frac{\Delta s}{c\Delta t}. \tag{4.1}$$

On the other hand the particle velocity is directly linked to its momentum through

$$\beta(p) = \frac{p}{\sqrt{p^2 + m^2}}, \tag{4.2}$$

with m being the particle mass. Equation 4.2 gives for each momentum the corresponding theoretical value of β. Thus, by looking to the two-dimensional distribution of β versus momentum this gives a possibility to identify the different particle types (see figure 4.8). This procedure is very efficient since the two quantities used for identification are measured by two different detectors. For a particle candidate which has been wrongly matched the results are uncorrelated which allows to further remove mismatched tracks.

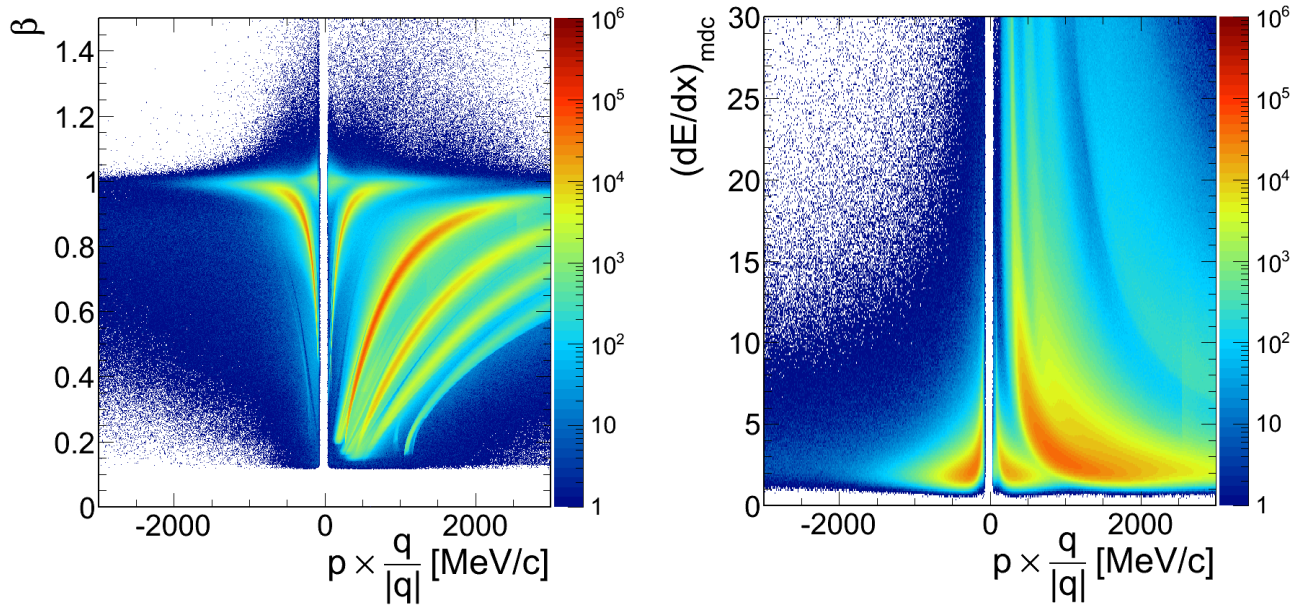

Figure 4.8: Original distributions after event and track selection. Left panel: β versus momentum times polarity spectrum. Right panel: Energy loss in the MDCs versus momentum times polarity spectrum.

The measured mass of each particle is also calculated using the equation for the momemtum $p = \gamma m \beta c$ where γ is the Lorentz factor. This gives also the possibility to identify the particles by their measured masses. The measured mass spectrum with the identified particles is shown in figure 4.9.
Another possibility to identify the particle type is to use the energy loss measured in the MDC dE/dx_{MDC}. When a particle is traveling through matter it will loose energy by the electromagnetic interaction with the atomic electrons of the matter. The energy loss on the one hand will depend on the particle properties like its velocity, its charge and its energy but also on properties

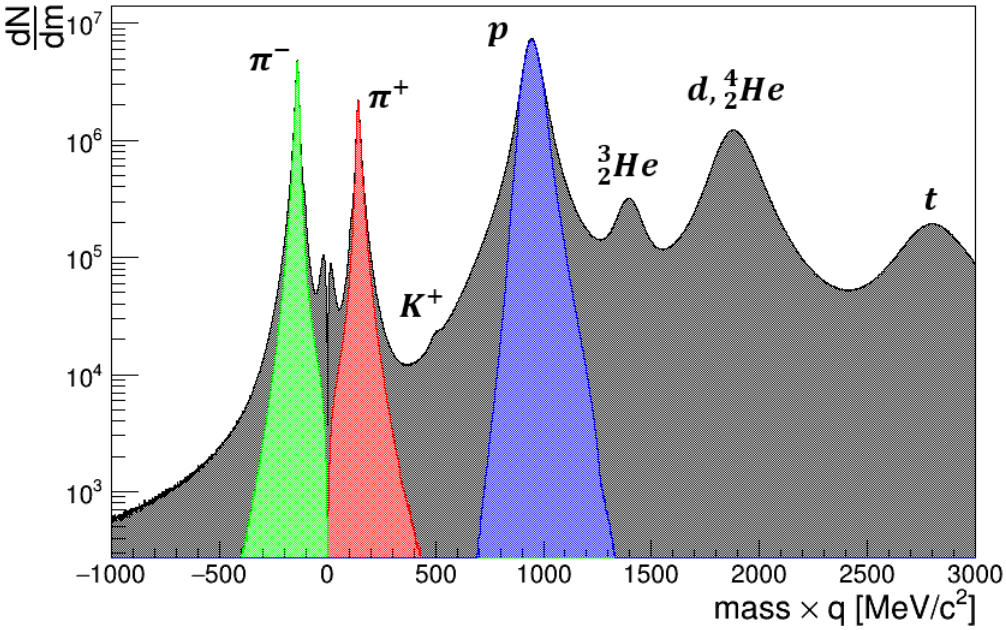

Figure 4.9: Distribution of the measured masses. The different particle types are separated by there $m \cdot q$ value. The colored peaks are the distributions after the full particle identification procedure which go into the analysis.

of the matter. The energy loss, meaning the energy dE which a particle loose when traveling a distance dx through matter, can be estimated by the Bethe-Bloch formula [61]:

$$-\frac{dE}{dx} = 4\pi N_A r_e^2 m_e c^2 z^2 \frac{Z}{A}\frac{1}{\beta^2}\left(\frac{1}{2}\ln\left[\frac{2m_e c^2\beta^2\gamma^2 W_{\max}}{I^2}\right] - \beta^2 - \frac{\delta(\beta\gamma)}{2}\right). \tag{4.3}$$

$N_A = 6.022 \cdot 10^{23}\,\mathrm{mol}^{-1}$ is the Avogadro number, $r_e = 2.8\,\mathrm{fm}$ and $m_e = 0.511\,\mathrm{MeV}$ are the classical radius of the electron and its mass respectively, z is the charge of the incident particle, Z is the charge of the absorber and A its atomic mass, $W_{\max}$ is the maximum possible energy transfer to the electron in a single collision, I is the mean excitation energy and $\delta(\beta\gamma)$ is a correction term for the density effect. This formula holds in the intermediate energy range in which HADES measuring, meaning a momentum range from 0.1 to 1 GeV/c.
Therefore, this formula can also be used to identify the particles. The distribution of the energy loss in the MDC as a function of the momentum is displayed in the right panel of figure 4.8.
In the hydra framework there is an automatic particle identification procedure included [62]. The starting point is the recalculation algorithm of the collision start time t_0 for each reconstructed track. Assuming stables particles the following mass hypothesis are used: $e^\pm$, $\mu^\pm$, $\pi^\pm$, $K^\pm$, p, d, t, ^{3}He and $^4_2$He. After testing all hypothesis, only the best one is chosen. The testing itself is done using both, the velocity and the energy loss measured in the MDC. The deviations of the measured to the theoretical value normalized by their uncertainties are used. For optimum results these quality parameters are weighted by 75 % for the velocity and 25 % in case of the energy loss. The uncertainties are obtained from simulation and experimental data. From a detailed study of Monte-Carlo simulations in GEANT3 the uncertainty arising from the resolution of the momentum reconstruction and track length are obtained. For both time-of-flight walls the

intrinsic uncertainties are obtained from the data. The theoretical values are calculated including the specific energy loss, multiple scattering and the material budget of the spectrometer as a function of zenith angle. The hypothesis are restricted to a $4.5\,\sigma$ window around the theoretical values otherwise the particle candidate is directly discarded. Finally, the **P**article **ID**entidy is chosen to be the hypothesis having the minimal normalized error.
The result of this identification procedure in the β-momentum spectrum can be seen in figure 4.10. Shown are only the particles used in this analysis, i.e. positively charged pions, negatively charged pions and protons TOF and RPC separately.

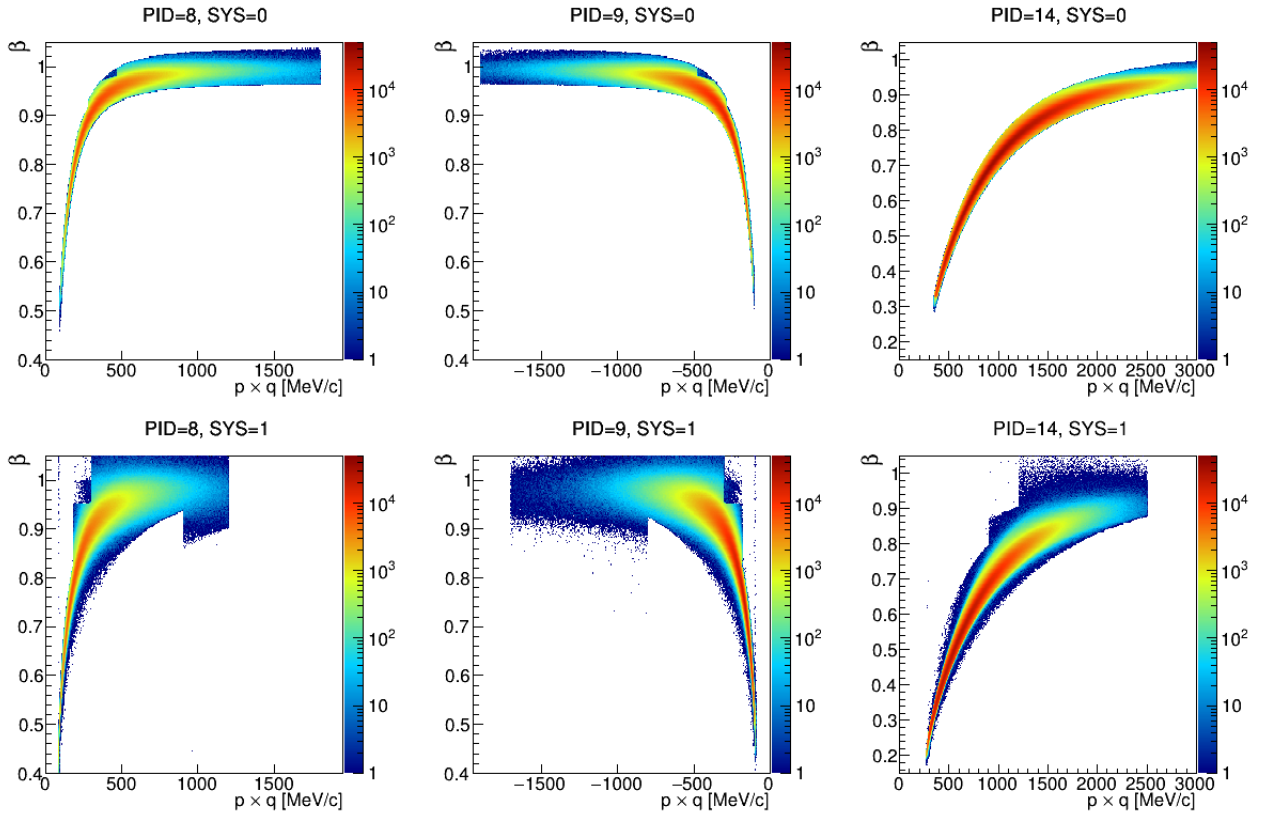

Figure 4.10: β versus momentum distributions after particle identification by the procedure included in generation eight. In the upper row distributions are shown for SYS $= 0$ which is RPC while in the lower row this is in case of SYS $= 1$ which is the TOF detector. From the left to the right, positively charged pions (pid $= 8$), negatively charged pions (pid $= 9$) and protons (pid $= 14$) are shown.

The main part of the distributions around the theoretical value is kept. Only at the edges of the distributions, especially in the TOF region the particle identification shows small systematics. In order to not get affected by this, an additional cut has been applied to further remove particles far away from the theoretical value.
This procedure is based on the spectra shown in figure 4.10. Hence, the procedure is done for each particle type and each system[3] individually.
Starting for the β versus momentum distribution, for each momentum bin of size $\Delta p = 1\,\mathrm{MeV/c}$ the spectra is projected resulting in a one-dimensional β distribution. Then this distribution is fitted two times by a gaussian function while the mean value μ and the standard deviation σ are

[3] With "system" the two time-of-flight detectors are ment: RPC (SYS $= 0$) and TOF (SYS $= 1$).

stored for each momentum bin. As a starting value the theoretical β value is used. Afterwards, the distribution of μ is fitted as a function of the momentum p by the function

$$\mu(p) = k_1 \frac{(k_2 p - k_3)\text{sign}(q)}{\sqrt{(k_2 p - k_3)^2 + m^2}} + k_4. \tag{4.4}$$

This function is based on equation 4.2 with additional free parameters k_i in order to give enough degrees of freedom to fit the measured distribution. The fit was restricted to a certain range in order to not get affcted too much by the edges of the fitted mean values. Then the fit function was extrapolated over the whole momentum range. The fit ranges are summarized in table 4.2.

Fit variable	π^+	π^-	p
μ	150-600 (RPC) 100-700 (TOF)	100-600 (RPC) 100-600 (TOF)	300-2000 (RPC) 400-1500 (TOF)
σ	200-700 (RPC) 200-500 (TOF)	200-1200 (RPC) 200-600 (TOF)	500-2500(RPC) 380-1400 (TOF)

Table 4.2: Fit ranges for the momentum p [MeV/c] for the different particle types in the two time-of-flight detectors of HADES. The fit ranges are tuned such that the extrapolation is describing the measured distribution as good as possible.

The same procedure is also done for the fitted deviations σ while the fit function was chosen to be a linear function, i.e. $\sigma(p) = k_1 x + k_2$. Finally, the particle identification is done by cutting in a $2\,\sigma$ window around the fitted mean values in each momentum bin. The results of this procedure are shown in figure 4.11 and 4.12. Basically most of the systematics are removed. In the TOF region some systematics enter the $2\,\sigma$ range but only at the momentum range $p > 2000\,\text{MeV/c}$ this is only very little statistics involved which is negligible. The deviations of the extrapolation from the measured shape in the low momentum range is not important to the analysis at the moment, due to an additional cut on the transverse momentum which is applied for different reason and removes the particles populating this momentum region.

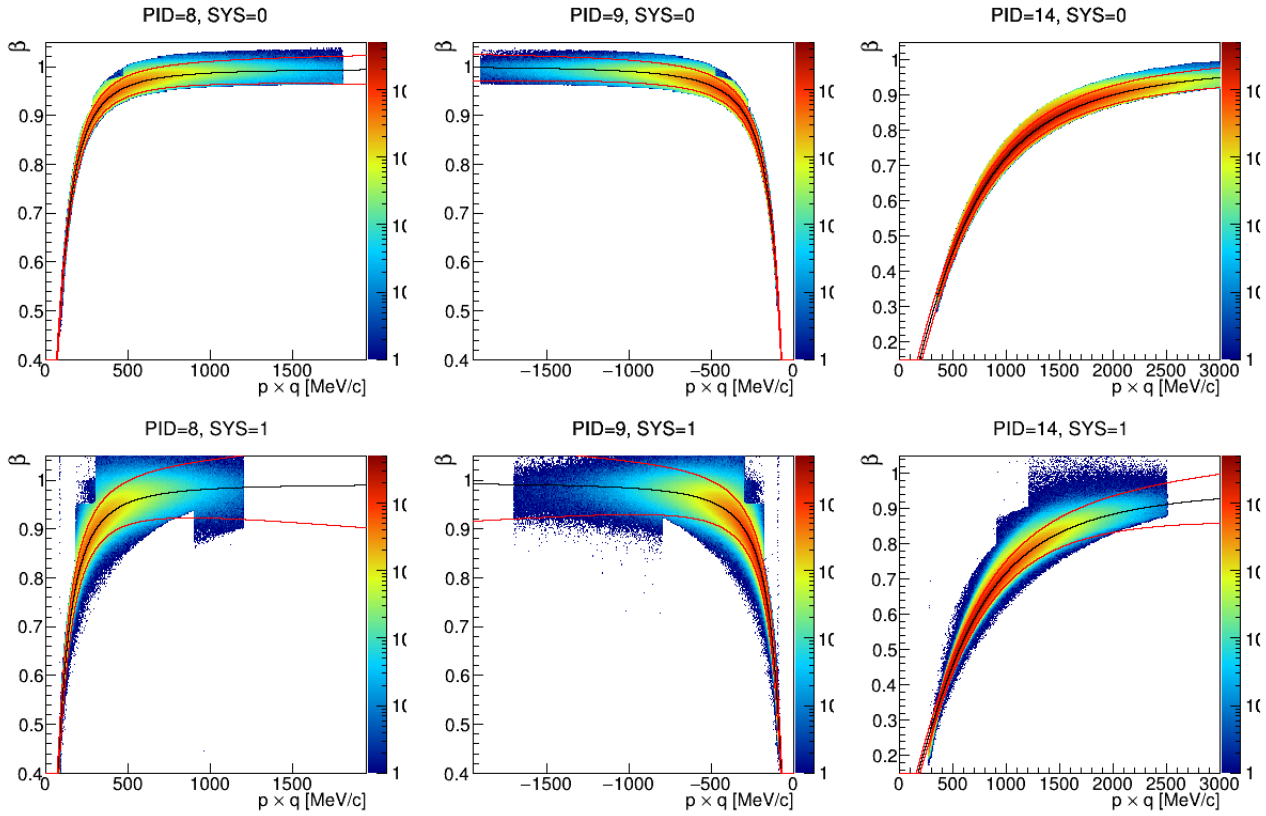

Figure 4.11: β versus momentum distributions after particle identification as discussed in the text. In the upper row distributions are is shown for SYS $= 0$ which is RPC while in the lower row this is in case of SYS $= 1$ which is the TOF detector. From the left to the right, positively charged pions (pid $= 8$), negatively charged pions (pid $= 9$) and protons (pid $= 14$) are shown. In addition, the extrapolated function of the fitted mean values is shown in black including a 2σ range indicated by the red lines.

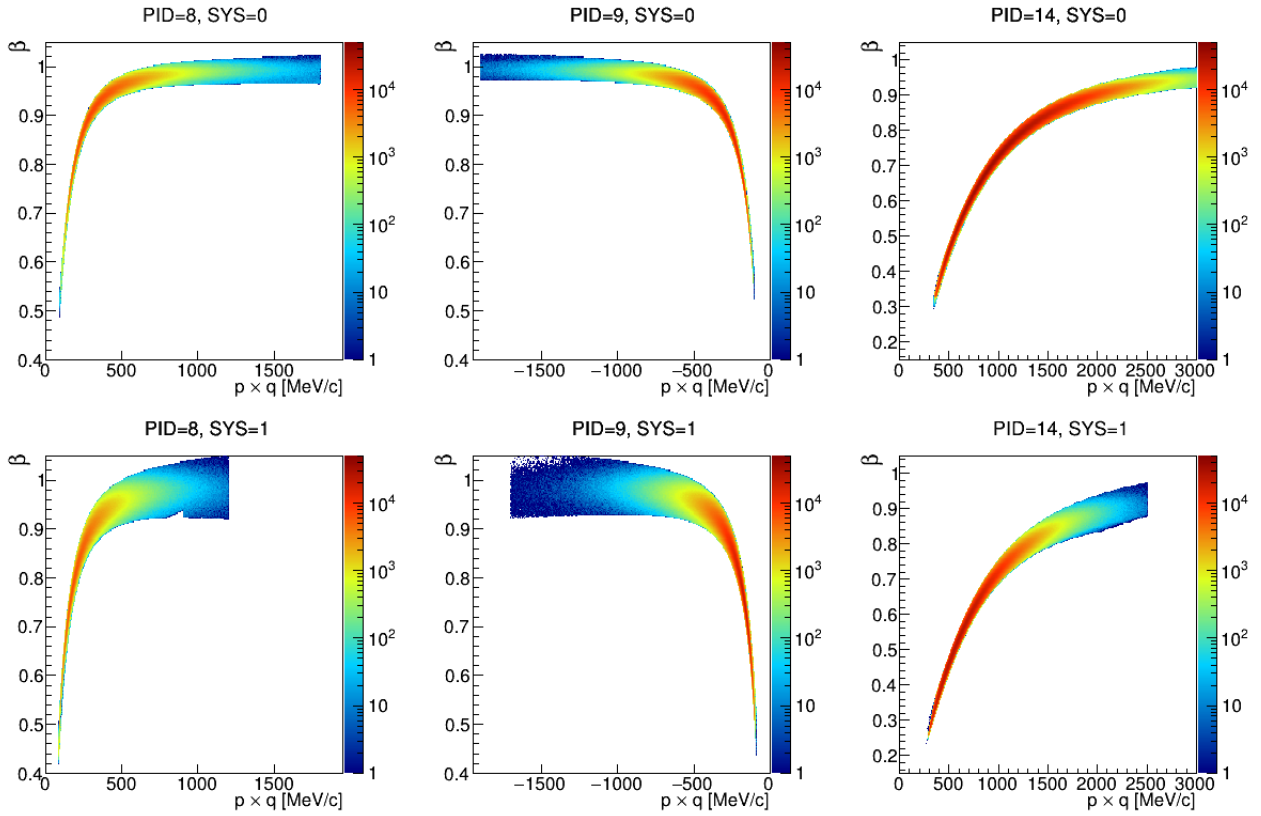

Figure 4.12: β versus momentum distributions after particle identification using probability method for particle identification plus a 2σ cut around the mean values. In the upper row this is shown for SYS $= 0$ which is RPC while in the lower row in case of SYS $= 1$ which is the TOF detector. From the left to the right, positively charged pions (pid $= 8$), negatively charged pions (pid $= 9$) and protons (pid $= 14$) are shown.

5 Analysis

After the event selection and the particle identification have been performed, it is usefull to study the particle directed flow before studying the two-particle correlations. This is important when analyzing integrated observables, for example the correlator $\gamma_{\alpha\beta}$ as a function of centrality. This means that the correlator has been integrated over rapidity and p_t. Since both observables, the flow as well as the two-particle correlations depend on the reaction plane angle, the resolution from the reconstruction of the event plane has to be taken into account.

5.1 Correction for EP resolution

As known from section 1.5 the flow is considered with respect to the event plane. The event plane is reconstructed from the spectators and hence it has a certain resolution. Therefore, this has to be taken into account. For a detailed description of the method see [63], [64], [56].
The resolution of the measured event plane is limited due to the finite amount of particles. For the flow related observables this means that the measured value is always smaller than the real one, since the flow is at maximum in the reaction plane frame. Therefore, it was proposed to correct the final values by scaling them with the event plane resolution R_n. The resolution is given by

$$R_n = \langle \cos[n(\Psi_n - \Psi_{RP})] \rangle \,, \tag{5.1}$$

where n is the n-th harmonic used in the Q-vector analysis and Ψ_n is the corresponding event plane angle. Then the real flow values v_n can be obtained by

$$v_n = \frac{v_n^{\text{obs}}}{R_n}, \tag{5.2}$$

taking into account that the procedure is very sensitive to the centrality. Using the fact that the resolution is estimated by calculating the event plane angle for two subevents A and B separately, the resolution can be obtained in a different way. Taking the $\Psi_{AB} = \Psi_A - \Psi_B$ distribution one can calculate a ratio r defined as

$$r = \frac{\int_{-180^\circ}^{-90^\circ} d\Psi_{AB} + \int_{90^\circ}^{180^\circ} d\Psi_{AB}}{\int_{-180^\circ}^{180^\circ} d\Psi_{AB}}. \tag{5.3}$$

The Ψ_{AB} distribution is calculated for each centrality percentile to obtain the corresponding resolution for this centrality. A typical distribution including the edges of the integrals is shown in figure 5.1. Using the resolution parameter $\chi = \sqrt{-2\ln(2r)}$ the resolution of the event plane can be calculated from

$$R_n(\chi) = \frac{\sqrt{\pi}}{2} \chi e^{-\chi^2/2} \left(I_{\frac{n-1}{2}}\left(\frac{\chi^2}{2}\right) + I_{\frac{n+1}{2}}\left(\frac{\chi^2}{2}\right) \right), \tag{5.4}$$

where I is the modified Bessel function. The event plane resolution as a function of the centrality is shown in figure 5.2.

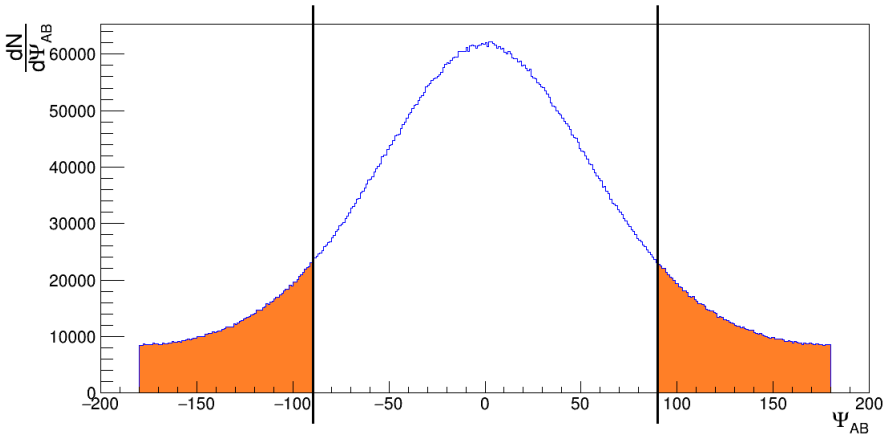

Figure 5.1: Distribution of $\Psi_{AB} = \Psi_A - \Psi_B$ for the 6 % centrality bin. The marked area divided by the whole spectrum gives the ratio r as a measure for the quality of the event plane resolution.

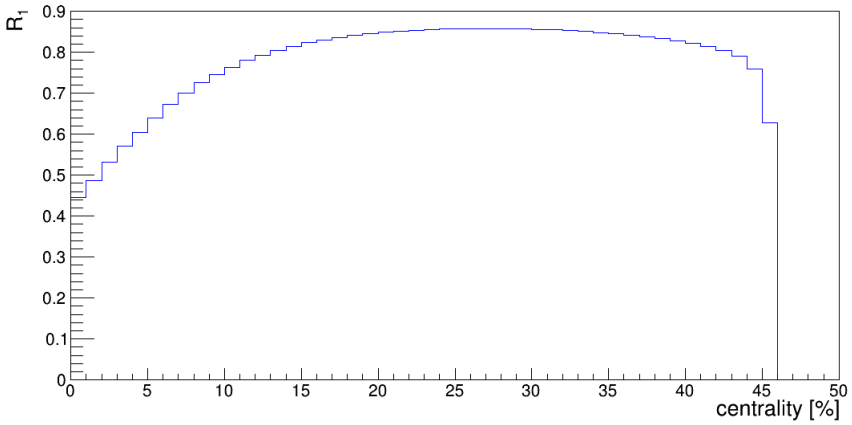

Figure 5.2: Event plane resolution as a function of the centrality. The reconstruction is worst in the most central events where only few spectators hit the FW. Then it increases towards the semi-central events and drops slowly towards the most peripheral events. This is due to the fragmentation of the spectators.

Then the flow coefficients can be corrected according to equation 5.2 while for the two-particle correlations the correction

$$\gamma_{\alpha\beta} = \frac{\gamma_{\alpha\beta}^{\text{obs}}}{R_1^2}, \tag{5.5}$$

is used, since $\gamma \propto v_1^2$. The correlator $\delta_{\alpha\beta}$ is not corrected because it does not depend on the event plane angle.
To correct the two-particle correlator γ for the event plane resolution requires further investigations and another method will be tried.

5.2 Flow studies

The directed flow is known to have an asymmetric shape around mid-rapidity which means that an integral over the directed flow in a symmetric window around mid-rapidity must be zero. The results obtained for the proton directed flow have a clear asymmetry. This can be seen by looking to figure 5.3. The different colors indicate different rapidity bins while the closed cirles result from the negative rapidity range and the open circles from the corresponding positive rapidity bin. The positive rapidity bins are then scaled by -1 to see the overlap as a function of the transverse momentum p_t for the four different centrality classes. Each bin is chosen to cover a rapidity range of $\Delta y = 0.1$.

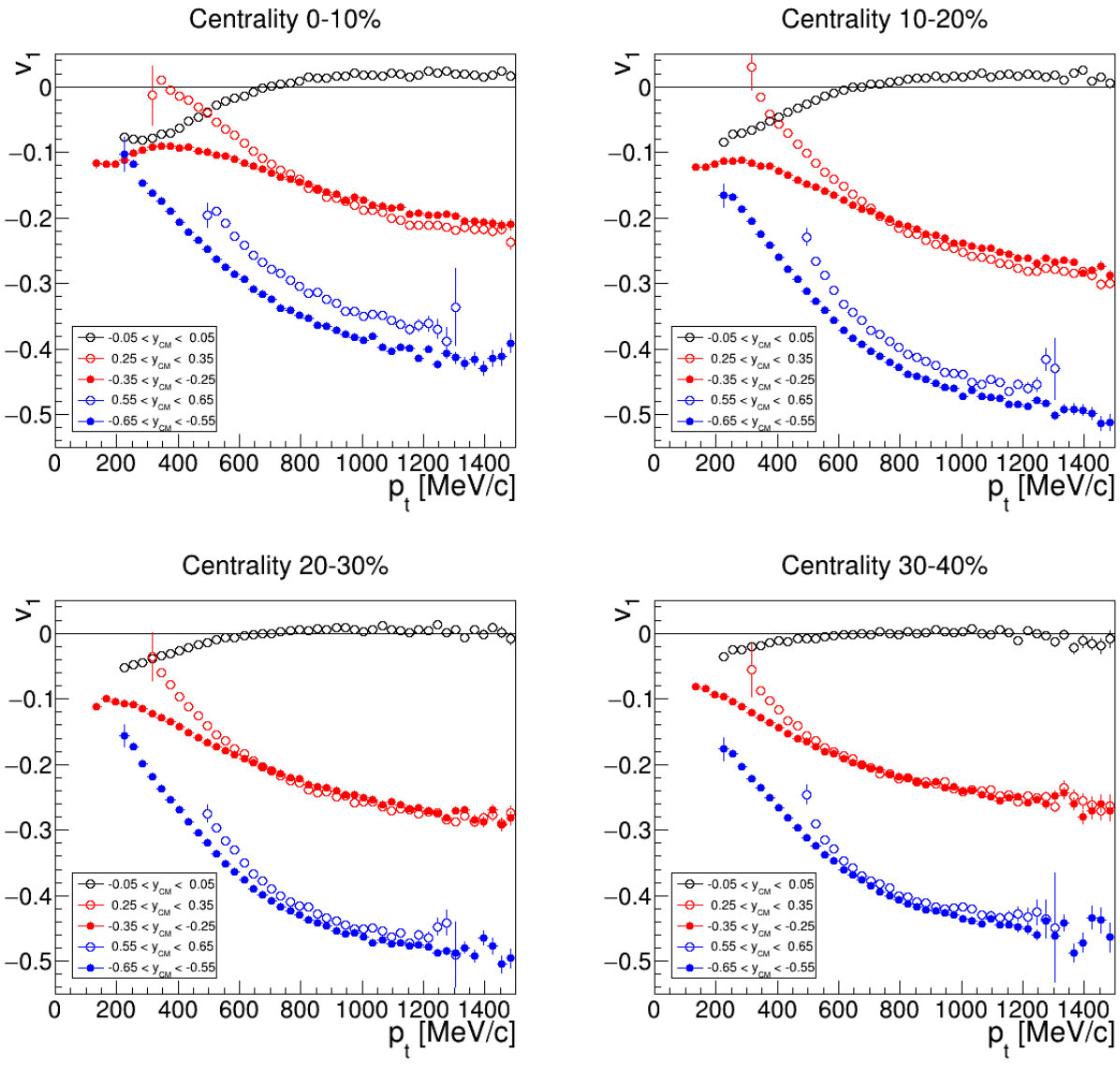

Figure 5.3: Directed flow of protons as a function of the transverse momentum p_t. Each panel corresponds to one centrality class. The different colors indicate different rapidity bins, while the positive y bins (open circles) are scaled by -1 to emphasize the symmetry.

The bin around mid-rapidity (black symbols) should be zero over the whole p_t range. As seen in figure 5.3 this does not seem to be the case. Assuming a mean deviation of about $\Delta v_1 \sim 0.02$ this would contribute to the two-particle correlations already by $(\Delta v_1)^2 \sim 0.004$ which is of the same order as the expected signal. For the other rapidity bins the situation is worst for the two most central bins. Especially for the most backward and forward rapidity ranges the deviation become very large.
For pions the situation is similar (see figure 5.4 and 5.5). The difference is: for the most backward and forward rapidity ranges the two curves qualitively lie on top of each other (blue points) while the deviation in the rapidity range of $0.25 < |y_{CM}| < 0.35$ is large (red points).
Therefore, this effect has to be corrected for. The correction must include a centrality dependence but must also account for this deviations in the rapidity space.

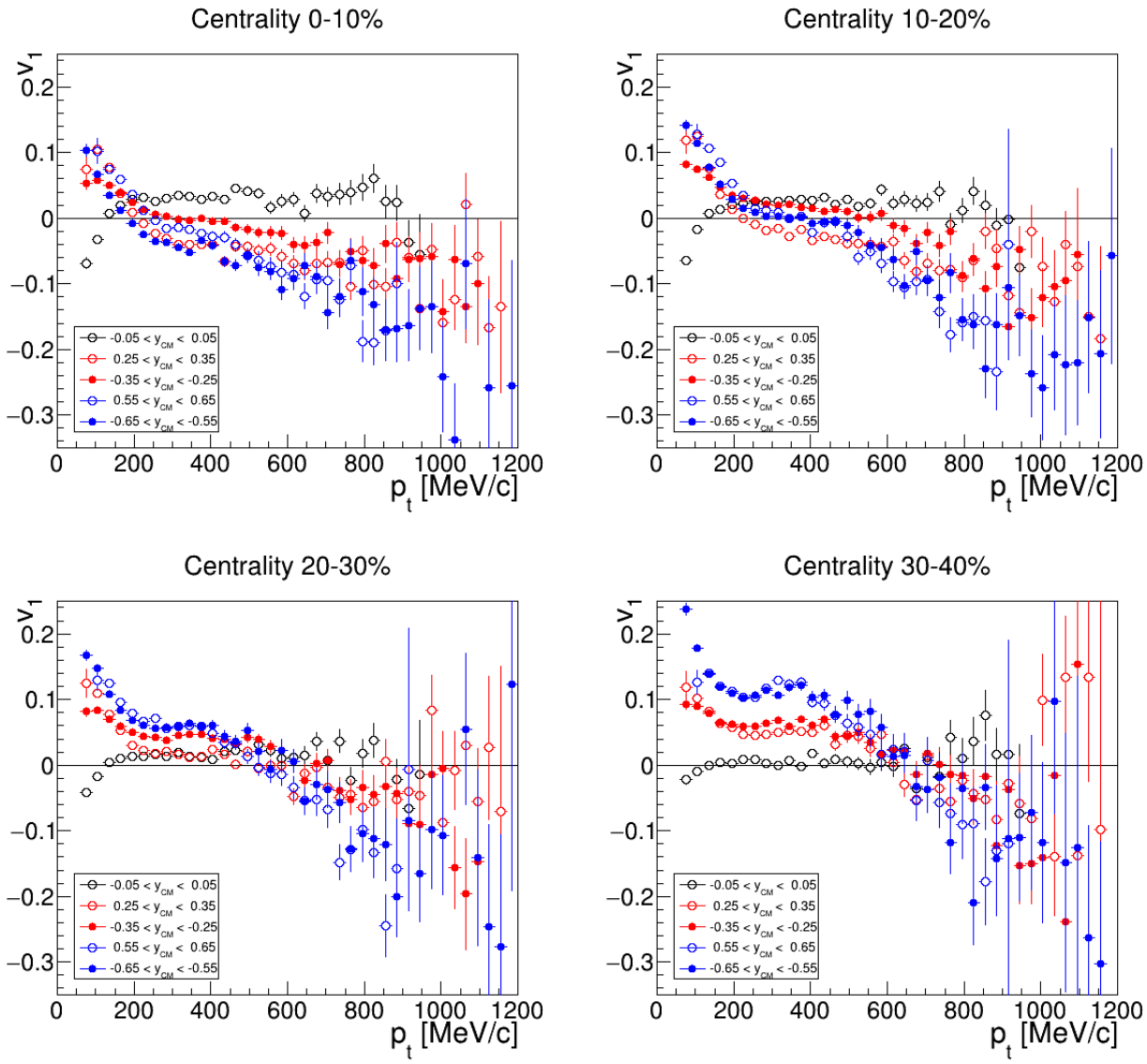

Figure 5.4: Directed flow of positively charged pions as a function of the transverse momentum p_t. Each panel corresponds to one centrality class. The different colors indicate different rapidity bins, while the positive y bins (open circles) are scaled by -1 to emphasize the symmetry.

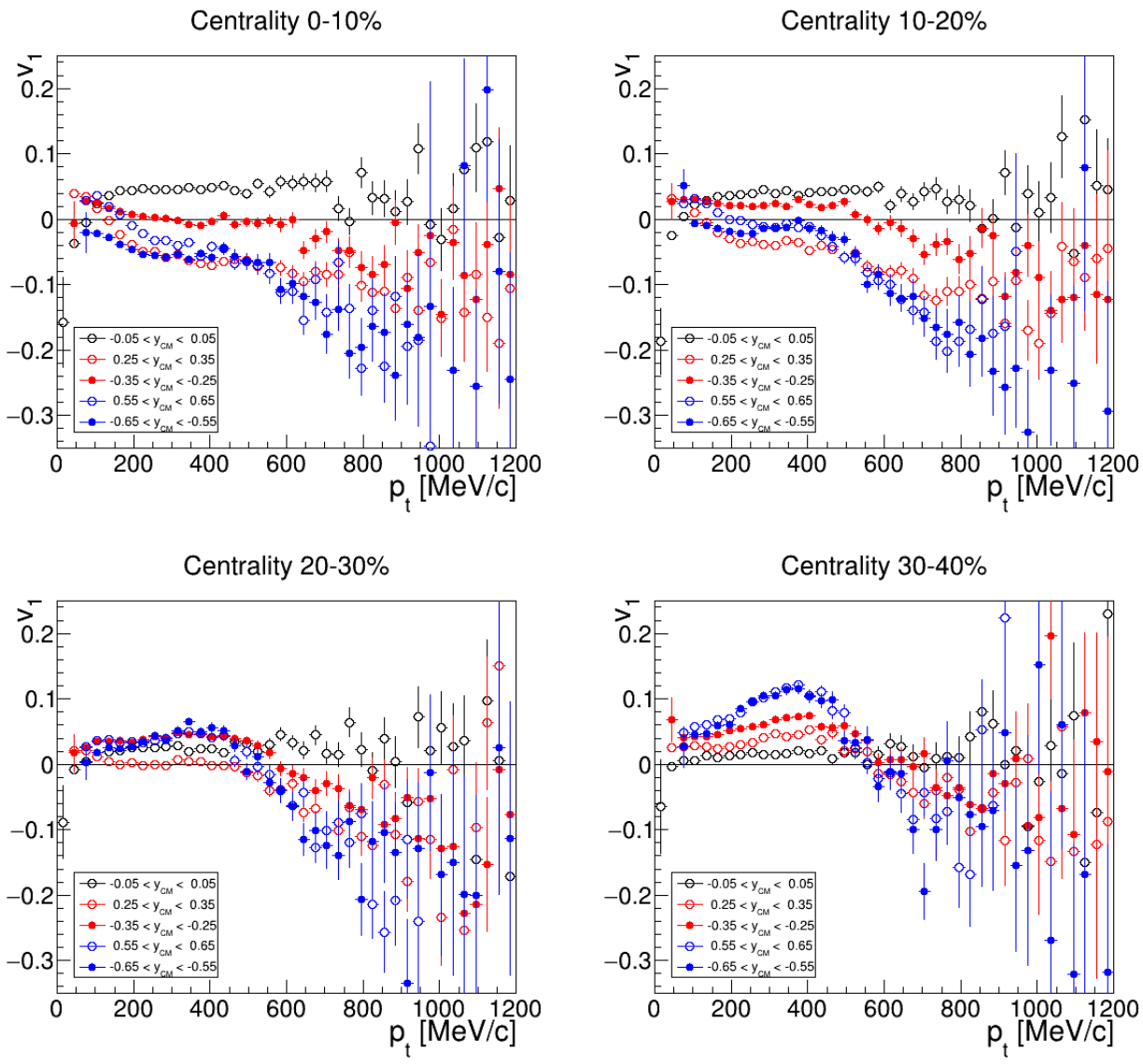

Figure 5.5: Directed flow of negatively charged pions as a function of the transverse momentum p_t. Each panel corresponds to one centrality class. The different colors indicate different rapidity bins, while the positive y bins (open circles) are scaled by -1 to emphasize the symmetry.

5.3 Efficiency corrections based on simulated data

The efficiency correction is done in four dimensions: the polar angle θ, the azimuthal angle ϕ, the momentum p and the sector multiplicity N_{sec}. The number of bins in each dimension is chosen to be large enough to have resonable statistic in each bin and to obtain a smooth correction function. On the other hand the bin size must be small enough to reproduce certain θ, ϕ, p or N_{sec} dependencies. Finally, to handle this trade-off the binning is chosen to be as summarized in table 5.1. For observables having a strong efficiency dependence the binsize is smaller while for observables where the efficiency has only small variations over a large range the binsize is set to be larger.

Coordinate	θ [°]	ϕ [°]	p [MeV/c]	N_{sec}
Number of bins	15	72	30	12
Min. value	0	0	0	0
Max. value	90	360	3000	24

Table 5.1: Bin setting for the efficiencies calculated based on simulations.

According to this binning the efficiency matrix is calculated by dividing two four-dimensional histograms. The first histogram is filled inside a loop over all particles generated by UrQMD. These tracks are transported through HGEANT resulting in a particle candidate (PCandSim). For each particle the physical observables θ, ϕ, p are asked from the PCandSim as well as the multiplicity of the sector in which this particles has been detected. Then the corresponding bin is incremented by one, but only if the corresponding particle was not inside the critical ranges of the MDC (see section 4.2).
The second histogram is then filled within the particle candidate loop. The tracks are reconstructed and the particle candidates are selected as describes in section 4.2, 4.3. Afterwards, the particles are filled to the corresponding θ, ϕ, p and N_{sec} bin while these variables are again the kinematical values generated by the UrQMD model. By this, the arbitrary shifting of the deviation between ideal and reconstructed values is avoided. In figure 5.6 the diviation is displayed for the momentum. The difference between ideal and reconstructed momentum is lying around the line where $p_{kine} = p_{reco}$ but there are also some cases where the deviation is large. The distribution overall seems to be shifted to the left side meaning, on average, that the reconstucted values tend to be larger then the real ones. Therefore, it is useful to chose only the ideal values such that the efficiency matrix is not affected by the large deviations between ideal and reconstructed momentum.

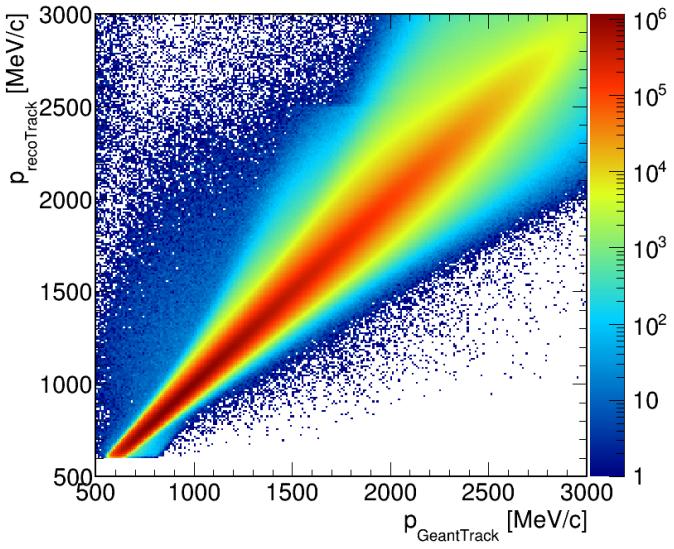

Figure 5.6: The reconstructed momentum compared to the ideal values. For the simulation the UrQMD model is used.

The efficiency matrix is calculated by dividing the two four-dimensional histograms bin-by-bin. The efficiency is then nothing else but the number of reconstructed tracks divided by the total amount of tracks within this four-dimensional space:

$$\epsilon(\theta,\phi,p,N_{\text{sec}}) = \frac{N_{\text{recoTracks}}(\theta,\phi,p,N_{\text{sec}})}{N_{UrQMDTracks}(\theta,\phi,p,N_{\text{sec}})}. \tag{5.6}$$

The distribution of the efficiency for the different particles π^+, π^-, p are shown in figure 5.7. The mean efficiency for a particle to be well[1] reconstructed is $\bar{\epsilon} \approx 52\,\%$ for π^+, $\bar{\epsilon} \approx 51\,\%$ for π^- and $\bar{\epsilon} \approx 63\,\%$ for p. The mean efficiencies are lower compared to the standard analysis because the requirements for the particle identification are set to be strong in order to achieve a high purity sample needed for the two-particle correlations. The efficiency distributions show a long tail towards low efficiency values. This can bias the results since the flow values are weighted in the analysis by $1/\epsilon$ which would lead to large contributions from particles having very low reconstruction efficiency. Therefore, an efficiency of at least $\epsilon > 25\,\%$ is required.

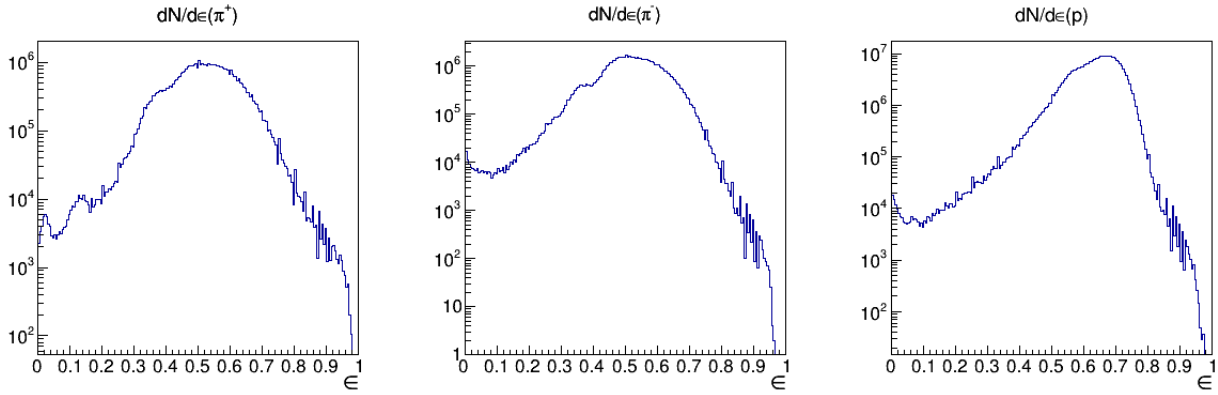

Figure 5.7: Efficiency distributions for the different particles: π^+ (left); π^- (middle); p (right). The efficiencies are obtained from simulations by appliying the same cuts used in data.

Figure 5.8 displays the efficiency in one of the four dimensions for protons, positively and negatively charged pions. The efficiency is then averaged over the other three space coordinates.
The efficiency as a function of θ increasing towards higher θ values. But overall the efficiency change by less then 10 % with the obvious drops at the edges. The ϕ-dependence is also quite constant within each sector, while the reconstruction efficiency is highest at the edges and drops a bit toward the center of each sector. This is quite interesting since for both pions this is excatly the opposite. Clearly, between the sectors no particles are reconstructed.
As a function of the momentum there is a broad peak for lower momenta and then the efficiency stays constant until $\sim 2500\,\text{MeV/c}$ and then drops significanty. One also has to mention that the efficiency dependence for the three analyzed particles is very different as a function of momentum, while the shape for all other three variables is approximately the same. This is related to the original momentum distributions and the bending in the magnetic field.
For the sector multiplicity the efficiency is higher when there are less tracks in the sector. Then efficiency drops remarkably when increasing the number of tracks. Interesting is the small rise

[1] "Well" means that the reconstructed particle candidate satisfies all conditions which are applied in the analysis (see section 4.3).

for the highest sector multiplicities. The trend, as expected, is the same for all particle species. Afterwards the efficiency matrix has been used to calculate the particle directed flow, applied on the track level by weighting with the corresponding efficiency. As has been seen by comparing the reconstructed momenta with the simulated ones there can be large differences. Nevertheless, when analyzing data one can only rely on the reconstructed values. Hence it is not excluded that this reconstruction uncertainty leads to systematic contributions of the final results.
The results for the directed flow of protons, positively and negatively charged pions after efficiency correction are shown in figure 5.11, 5.12 and 5.13. Unfortunately the situation improved only a little bit. For the two central bins the deviations around midrapidity are still large. For the midrapidity bin the corrections at higher p_t even seem to overshout such that the proton directed flow is now $v_1 > 0$ while it was $v_1 < 0$ without any corrections. As can be seen, the improvement by this approach has turned to be not sufficient.

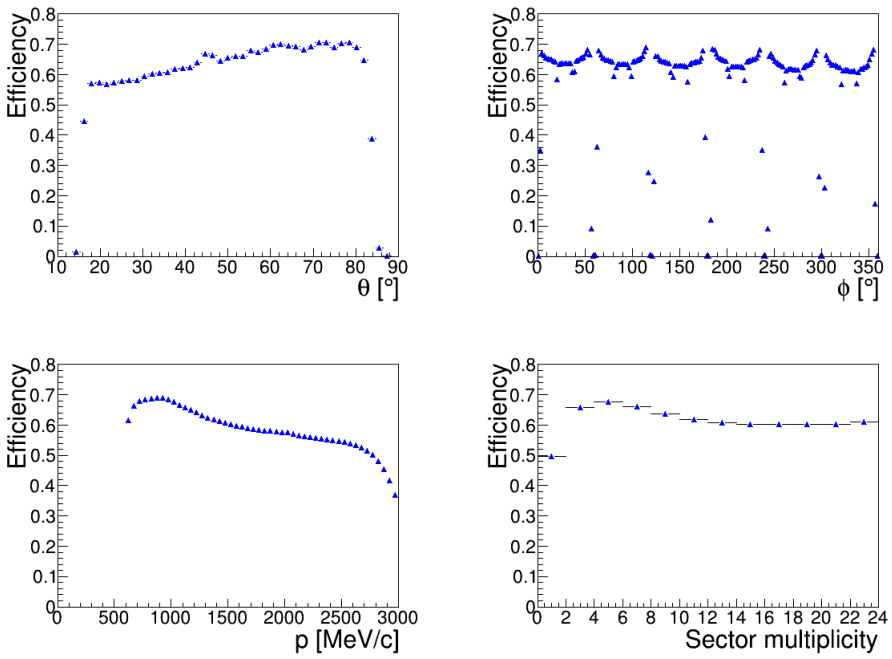

Figure 5.8: Efficiency dependencies for reconstructed protons. Upper row: as a function of polar angle θ (left) and azimuthal angle (right). Lower row: as a function of momentum (left) and sector multiplicity (right). The binning is the same as used to calculate the efficiency matrix.

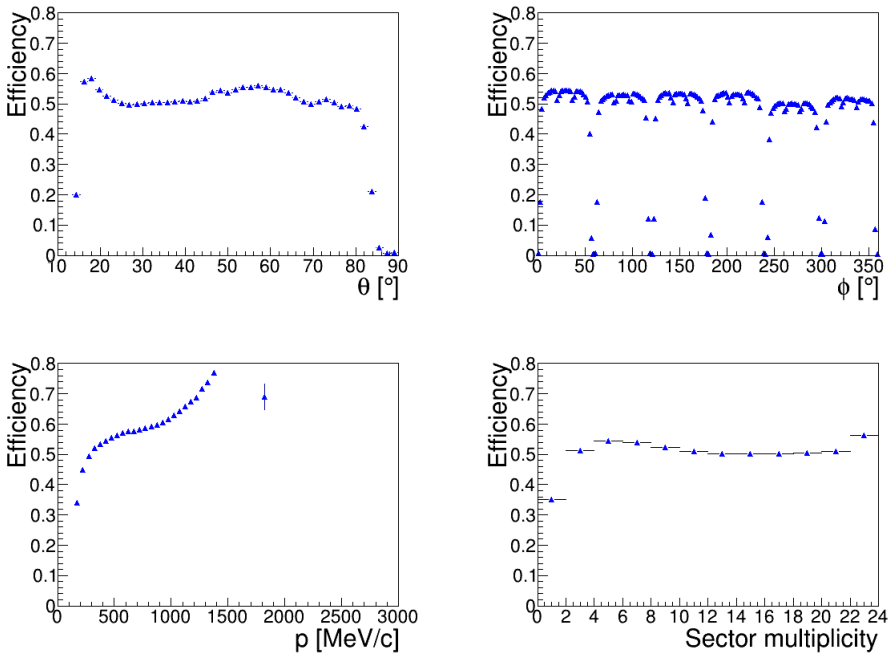

Figure 5.9: Efficiency dependencies for reconstructed π^+. Upper row: as a function of polar angle θ (left) and azimuthal angle (right). Lower row: as a function of momentum (left) and sector multiplicity (right). The binning is the same as used to calculate the efficiency matrix.

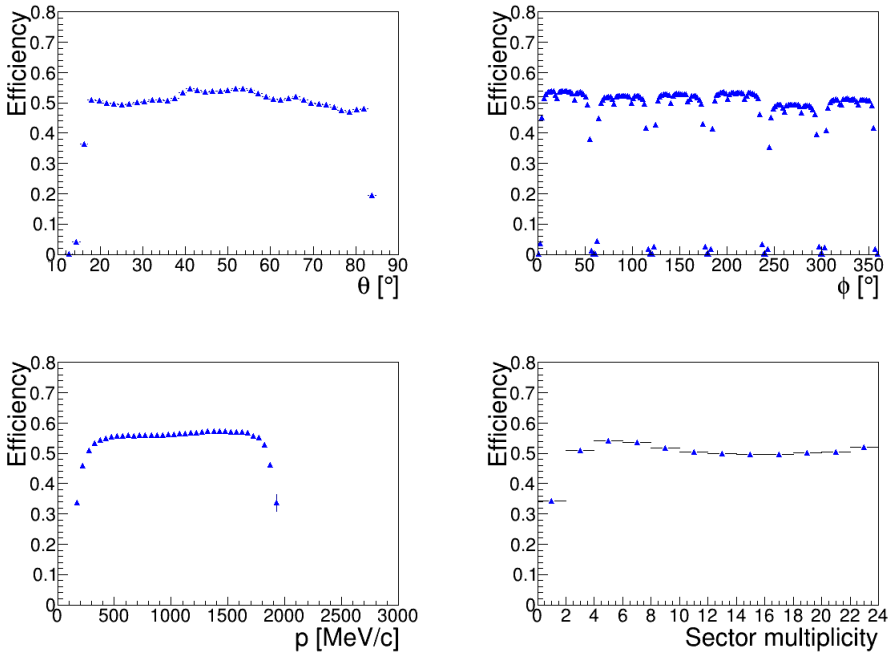

Figure 5.10: Efficiency dependencies for reconstructed π^-. Upper row: as a function of polar angle θ (left) and azimuthal angle (right). Lower row: as a function of momentum (left) and sector multiplicity (right). The binning is the same as used to calculate the efficiency matrix.

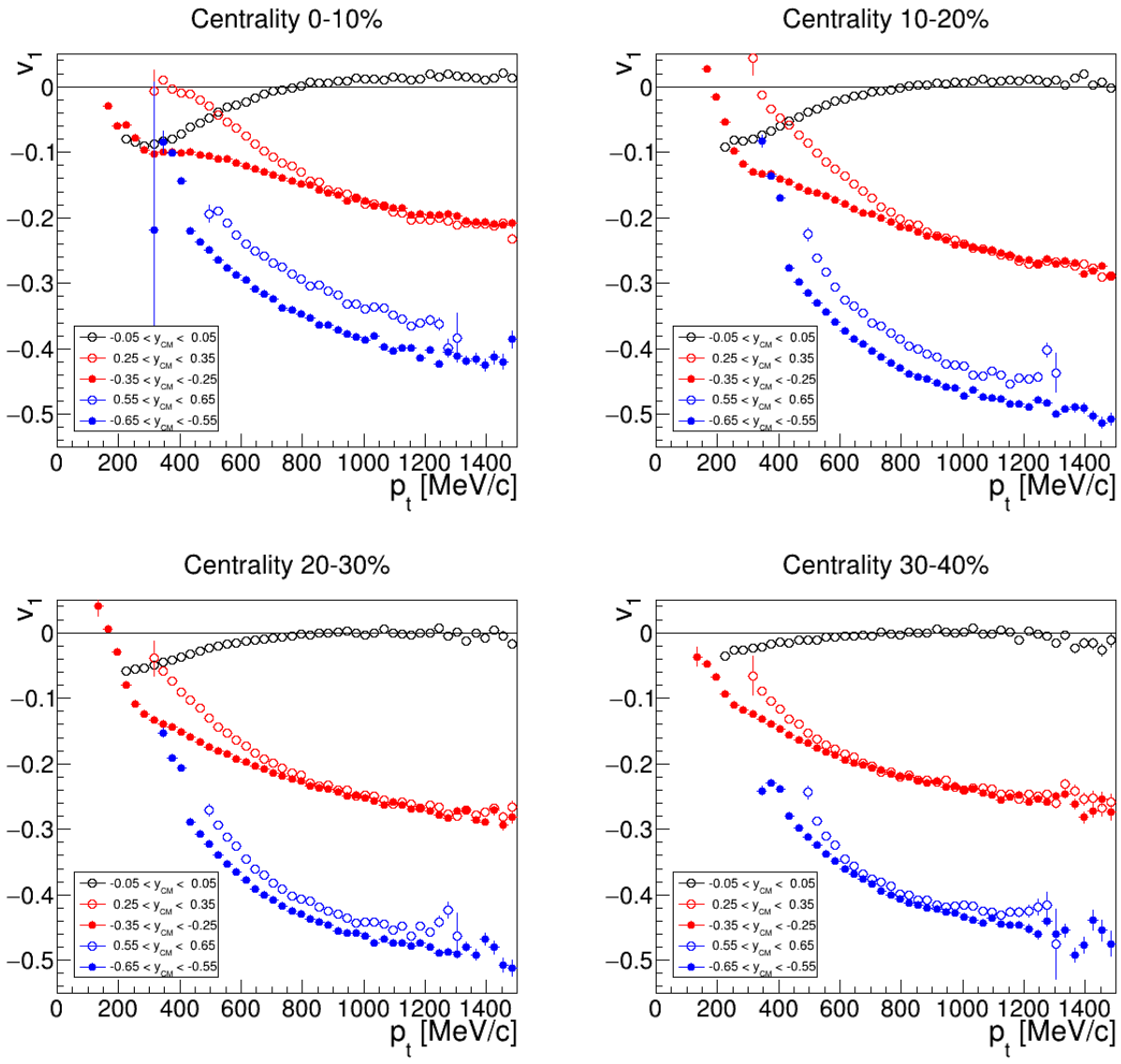

Figure 5.11: v_1 of protons as a function of p_t. The data is corrected for efficiency based on Monte-Carlo simulations using the UrQMD model. Each panel corresponds to one centrality class. The different colors indicate different rapidity bins, while the positive bins (open circles) are scaled by -1.

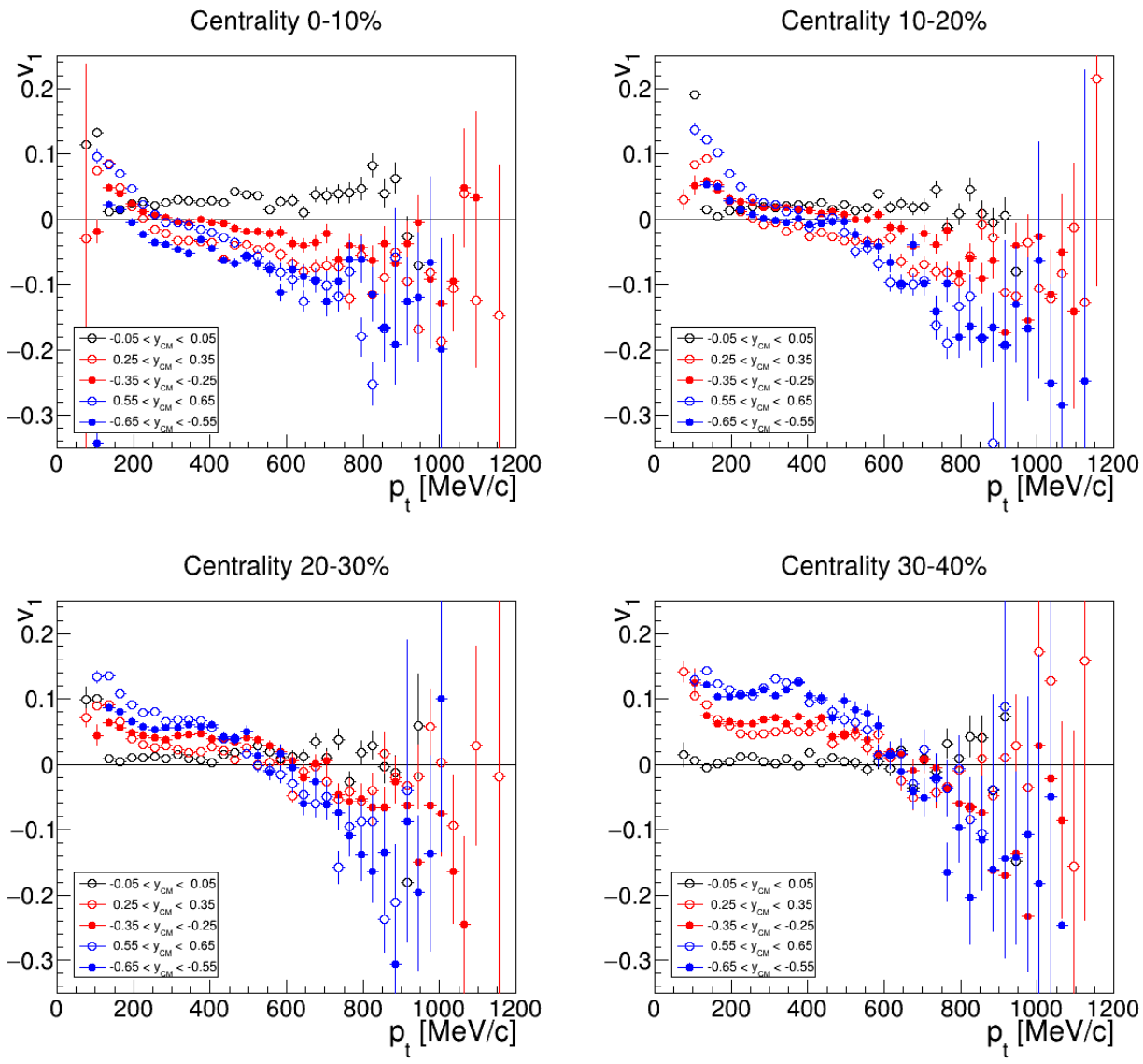

Figure 5.12: v_1 of positively charged pions as a function of p_t. The data is corrected for efficiency based on Monte-Carlo simulations using the UrQMD model. Each panel corresponds to one centrality class. The different colors indicate different rapidity bins, while the positive bins (open circles) are scaled by -1.

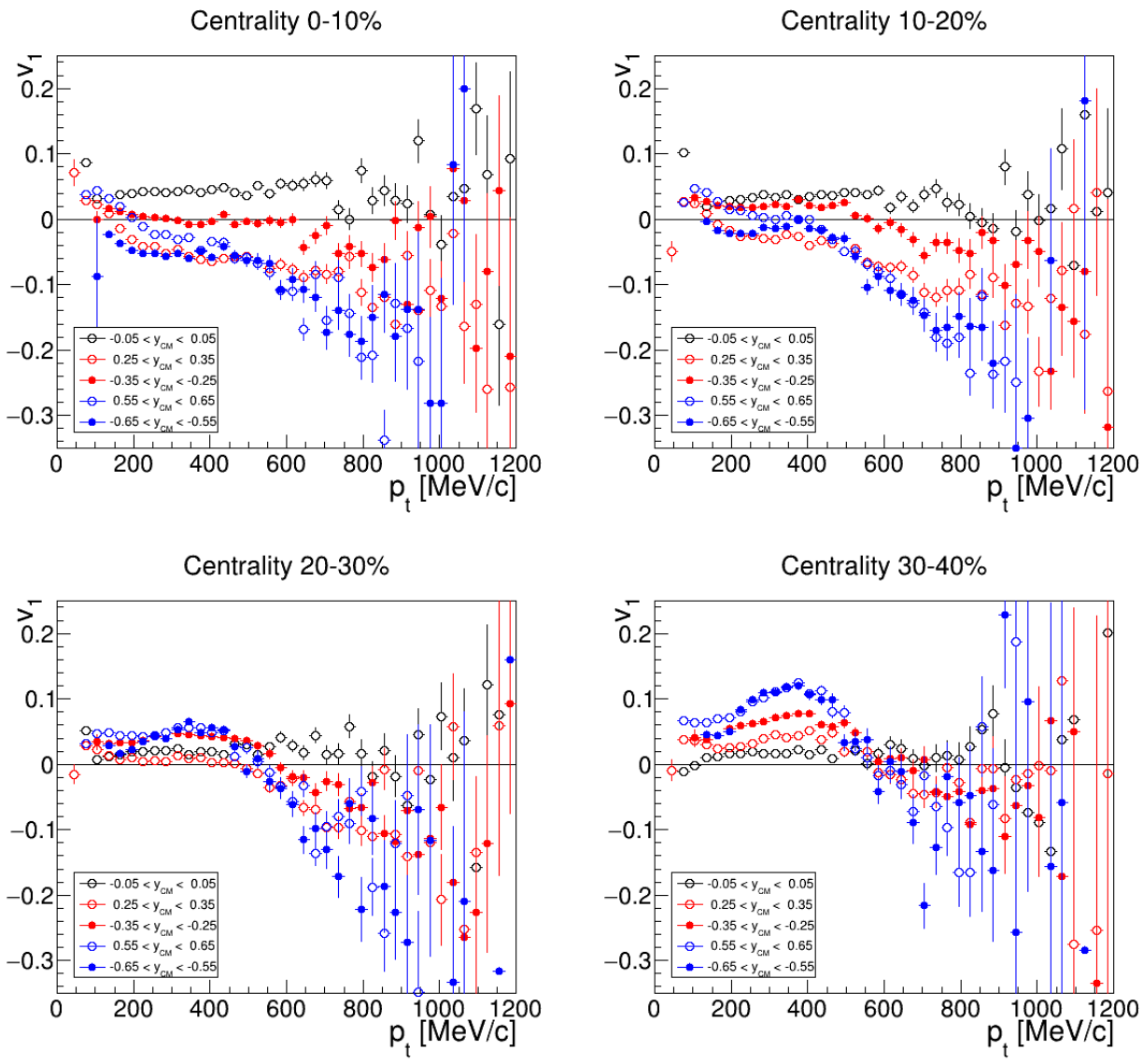

Figure 5.13: v_1 of negatively charged pions as a function of p_t. The data is corrected for efficiency based on Monte-Carlo simulations using the UrQMD model. Each panel corresponds to one centrality class. The different colors indicate different rapidity bins, while the positive bins (open circles) are scaled by -1.

5.4 Efficiency correction based on experimental data

To correct for the rapidity asymmetry detector effects another method has been proposed [65]. The idea is to correct for the efficiency loss as a function of the track density in the given phase space. A high track density will bias the track reconstruction which results in an efficiency loss. Therefore, the procedure is done for four different centrality classes in the dimensions of the polar angle θ and the azimuthal angle in the event plane frame $\Phi = \phi - \Psi_{EP}$. Extracting corrections with respect to the event plane could bring up systematics which is currently under investigation.

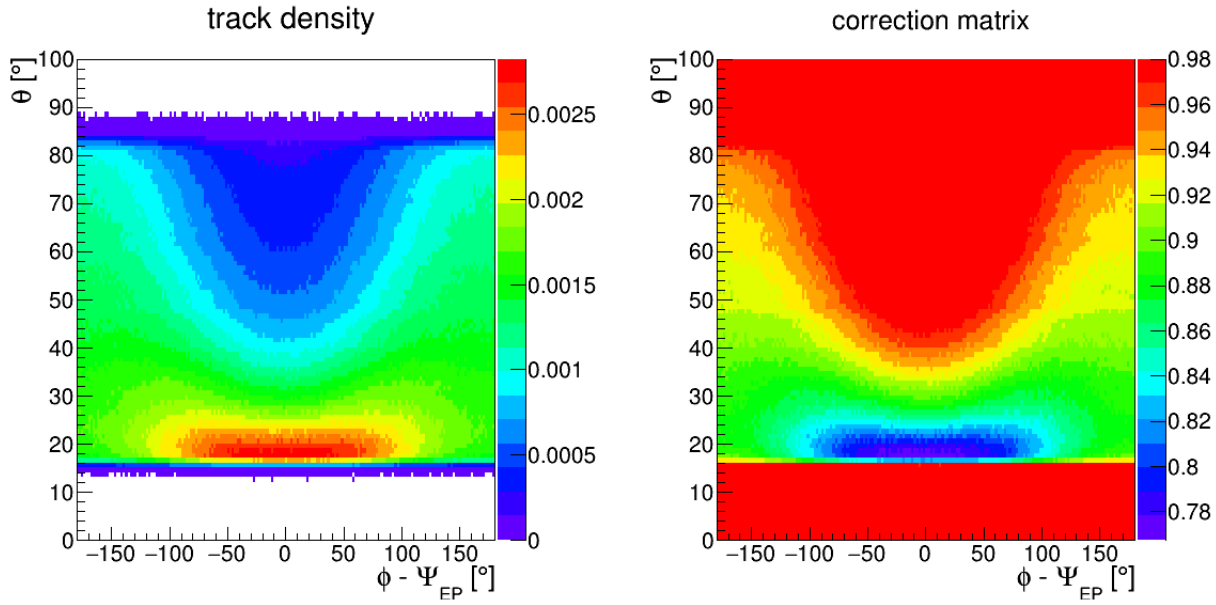

Figure 5.14: Left panel: Track density as a function of the polar angle θ and the azimuthal angle in the EP frame Φ. The distribution is normalized to one event. Right Panel: Correction factor as a function of the polar angle θ and the azimuthal angle in the event plane frame Φ [65].

The distribution of the track multiplicity in the θ vs. Φ space in show in figure 5.14 (left panel) for a centrality from $21-31\,\%$ and normalized to one event. For the same centrality the correction matrix is shown in the right panel of figure 5.14 in case of negatively charged pions. The efficiency as a function of θ has approximately a linear dependence which is also the case for the track density. Therefore, the dependence of the efficiency as a function of the track multiplicity N_{track} is estimated by

$$\epsilon(N_{\text{track}}) = \epsilon_0(1 - k \cdot N_{\text{track}}), \tag{5.7}$$

where $\epsilon_0 = 0.98$ is based on simulations and the constant k is set such that pion flow at midrapidity vanishes.
This method was applied to the experimental data and the measured flow was corrected accoring to this procedure. The results for pions and protons can be seen in the figures 5.16, 5.17 and 5.15. The first what catches the eye is the fact that the pion flow at mid-rapidity is still significantly different from zero. Especially for the positively charged pions in the two central bins the

deviation is significant. Even if the situation improved a lot, for the $0.25 \leq |y_{CM}| \leq 0.35$ bin the asymmetry is still very large, basically for all centralities. For the negative pions the corrections improve the situation remarkably.
The comparison of π^+ and π^- flow behavior hints for possible impurities in the distribution of positively charged pions caused by the tail of the protons. Nevertheless, deviations are still present for the negatively charged pions.
For the protons the best improvement is achieved. For most part of the distribution the anti-symmetry around mid-rapidity is recovered. In the lower p_t region the asymmetry is still present.

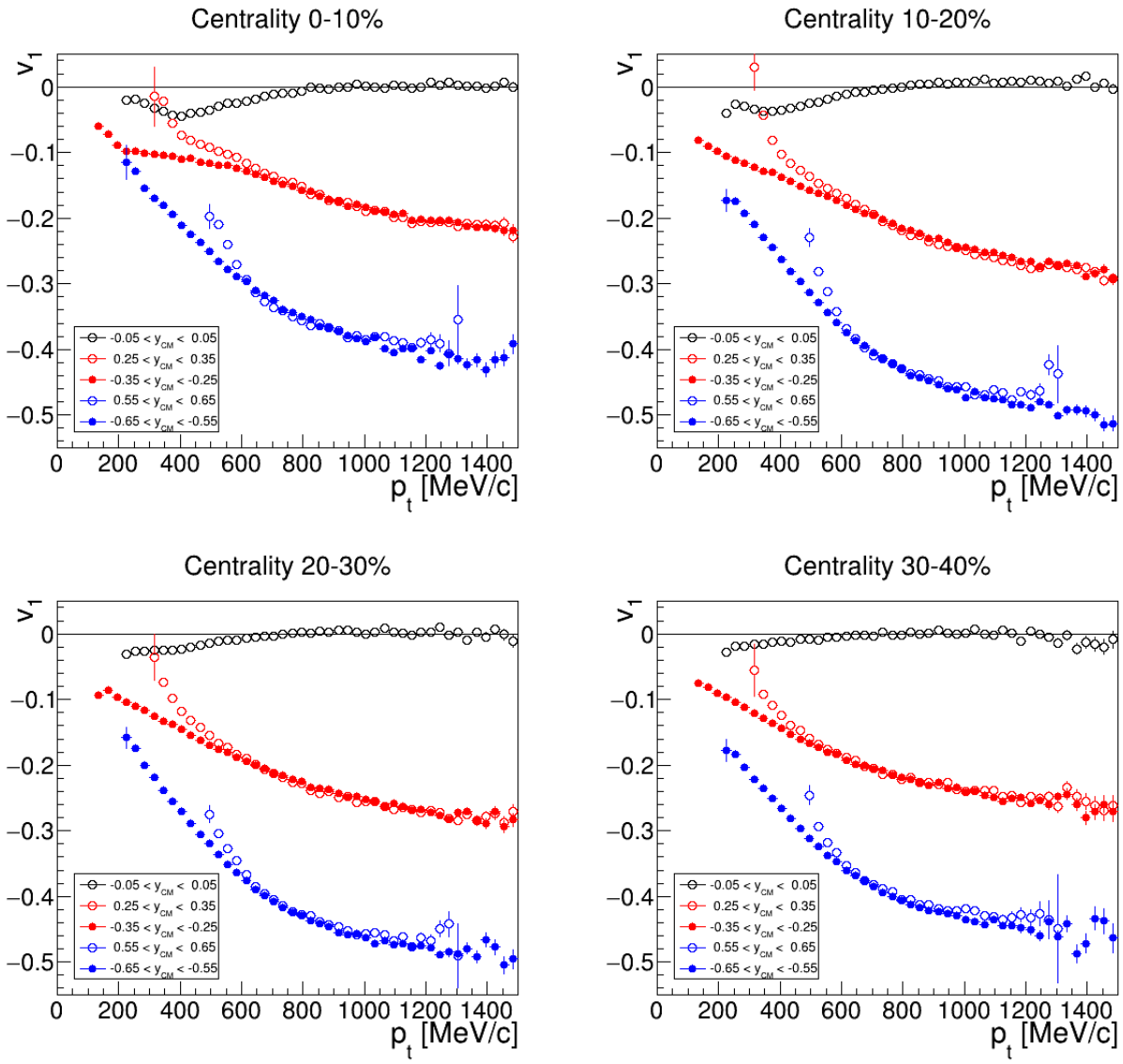

Figure 5.15: v_1 of protons as a function of p_t. The data is corrected for efficiency based on the track density. Each panel corresponds to one centrality class. The different colors indicate different rapidity bins, while the positive bins (open circles) are scaled by -1.

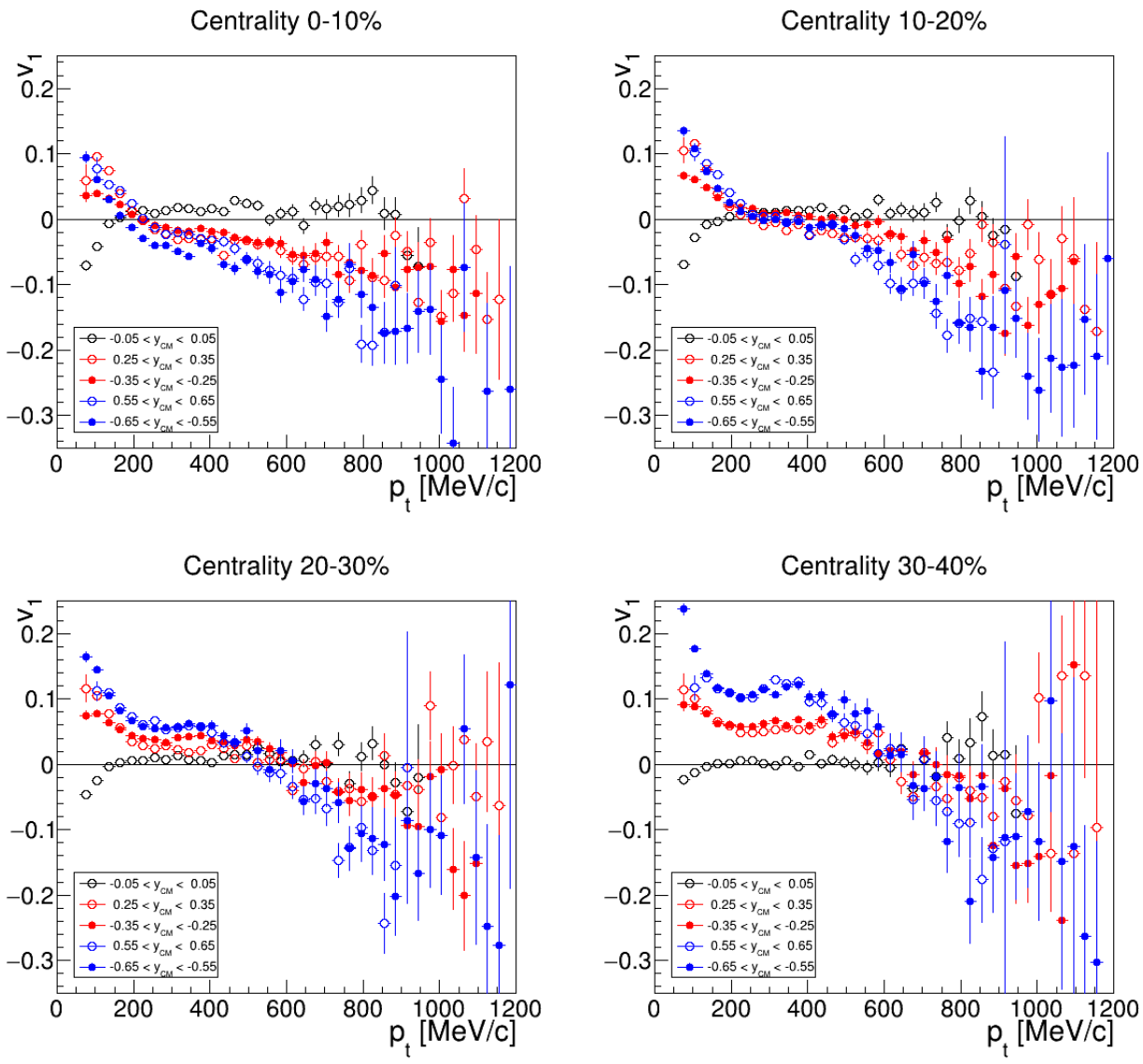

Figure 5.16: v_1 of positively charged pions as a function p_t. The data is corrected for efficiency based on the track density. Each panel corresponds to one centrality class. The different colors indicate different rapidity bins, while the positive bins (open circles) are scaled by -1.

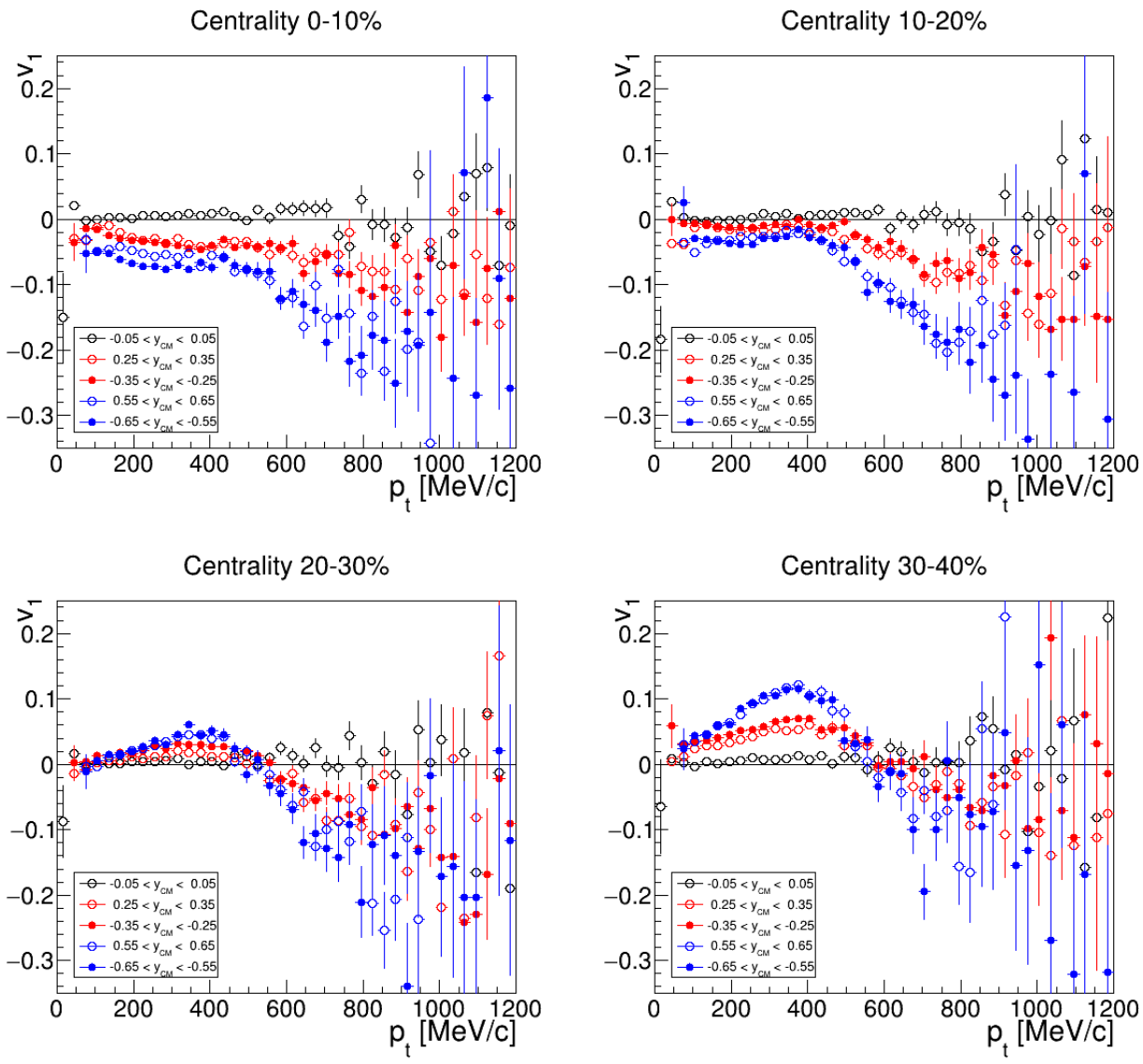

Figure 5.17: v_1 of negatively charged pions as a function of p_t. The data is corrected for efficiency based on the track density. Each panel corresponds to one centrality class. The different colors indicate different rapidity bins, while the positive bins (open circles) are scaled by -1.

In calculations of the charge dependent correlations only the p_t regions having the best symmetry around mid-rapidity are selected. This leads to the following phase space cuts summarized in table 5.2. The anti-symmetry seem is present in all different rapidity windows, therefore the correlations are considered over the full rapidity range.
The fact that the flow at mid-rapidity is non-zero even if the method itself force it to be zero results from a different cut setting used to calculate the efficiency matrix. The detailed analysis to identify from where the differences come from is still ongoing. Within the chosen p_t ranges, the situation looks solid in case of the protons. The proton distribution in the phase space of p_t vs. y_{LAB} (figure 5.18) show that p_t cut of $p_t > 600\,\mathrm{MeV/c}$ removes most of the statistics. For the pions (figure 5.19 and 5.20) we chose $150 < p_t < 600\,\mathrm{MeV/c}$. The situation is not better (i.e. large sample of pions is removed), especially for negatively charged pions a main part of the statistic is located around mid-rapitiy but below $p_t < 150\,\mathrm{MeV/c}$.

Particle	$p_{t,\mathrm{min}}$ [MeV/c]	$p_{t,\mathrm{max}}$ [MeV/c]
$\pi^{\pm}$	150	600
p	600	-

Table 5.2: Selected regions in the transverse momentum range used for charge correlations analysis.

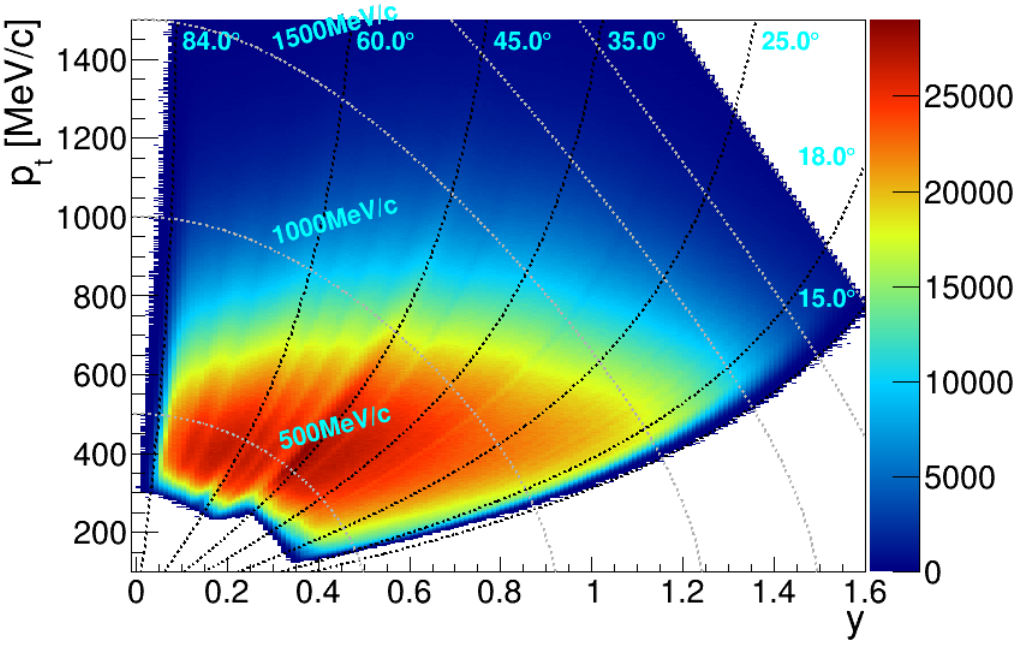

Figure 5.18: Phase space distribution of protons. The grey shaded lines indicated the lines of constant total momentum while the black shadded lines represent constant θ values.

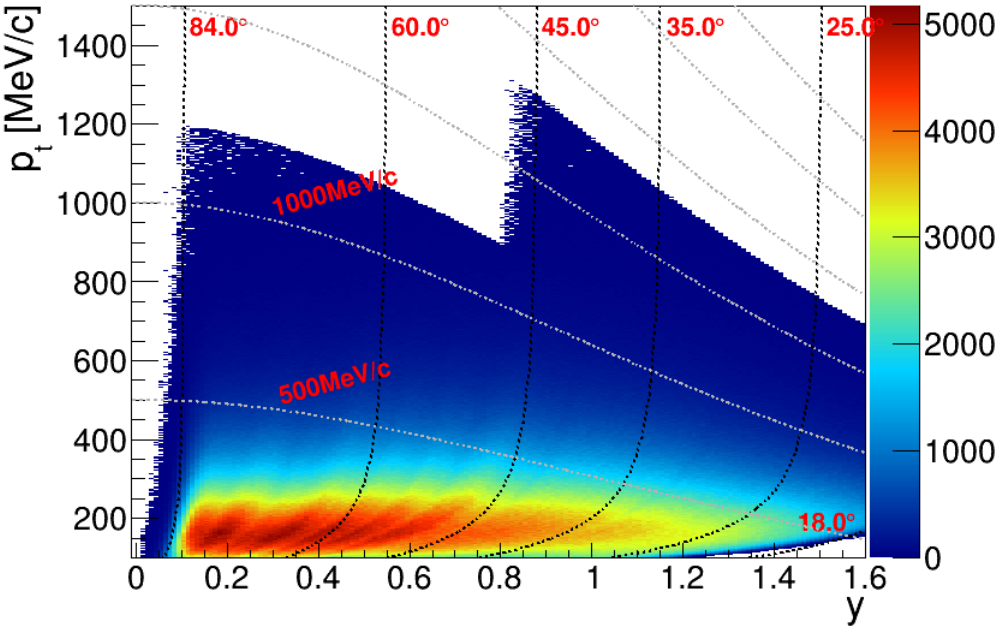

Figure 5.19: Phase space distribution of positive pions. The grey shaded lines indicated the lines of constant total momentum while the black shadded lines represent constant θ values.

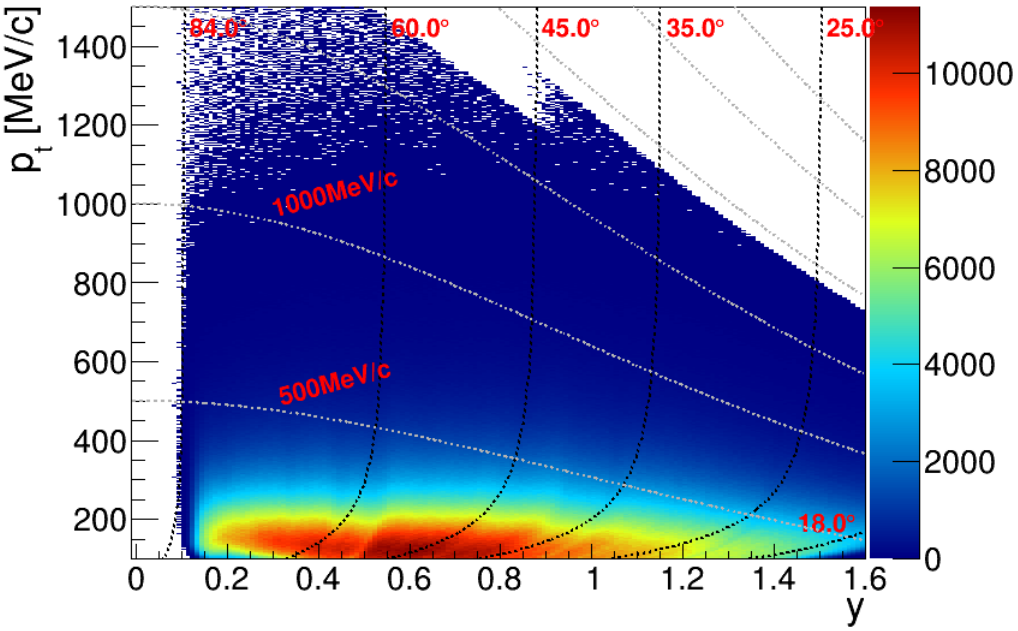

Figure 5.20: Phase space distribution of negative pions. The grey shaded lines indicated the lines of constant total momentum while the black shadded lines represent constant θ values.

6 Results

In this chapter the current results for the two-particle correlators, both γ and δ, will be presented (see definitions in section 1.6). The full event and particle selection is performed and the data is corrected for efficiency based on experimental data to account for the efficiency loss due to local high track densities. The data is also corrected by the event plane resolution in the corresponding centrality bin to include also the impact from the finite mutliplicities available in the Forward Wall detector to reconstruct the event plane.
Besides the γ and δ correlators to measure a possible charge separation, there are different correlation functions very useful to study possible detector effects. Based on the correlators γ and δ the following observables are used:

$$\gamma^*_{\alpha\beta} = \langle \sin(\Phi_\alpha + \Phi_\beta) \rangle = \langle \sin(\Phi_\alpha)\cos(\Phi_\beta) \rangle + \langle \cos(\Phi_\alpha)\sin(\Phi_\beta) \rangle \tag{6.1}$$

$$\delta^*_{\alpha\beta} = \langle \sin(\Phi_\alpha - \Phi_\beta) \rangle = \langle \sin(\Phi_\alpha)\cos(\Phi_\beta) \rangle - \langle \cos(\Phi_\alpha)\sin(\Phi_\beta) \rangle \,. \tag{6.2}$$

When averaging over many particles in many events, both correlators should vanish since the $a_1 = \sin(\Phi)$ coefficients are zero. In other words the correlators γ^* and δ^* are P-odd observables which yield zero when averaged over many events. Thus, these are good observables to look for possible detector effects which, when coupled to flow, could bring up large contributions to the measured signal.

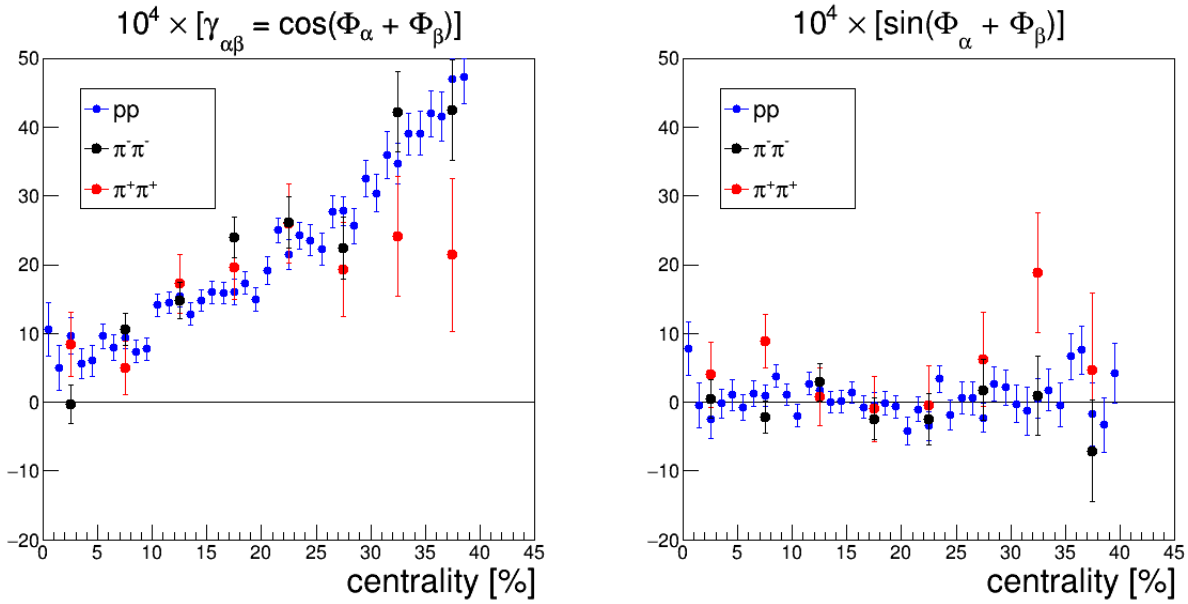

Figure 6.1: Two-particle correlator γ for $\pi^+\pi^+$, $\pi^-\pi^-$ and pp. The results are scaled up by 10^4. There is a clear rise of the signal towards peripheral events (left panel) while the background is small (right panel). For the protons $p_t > 600\,\text{MeV/c}$ and for the pions $150 < p_t < 600\,\text{MeV/c}$ are required.

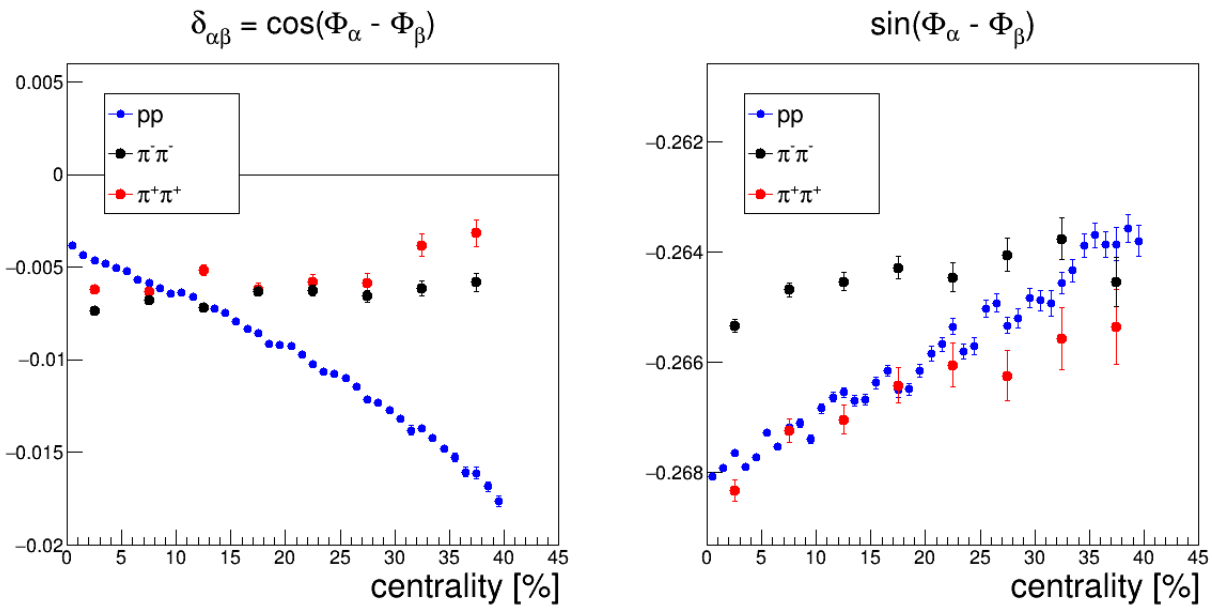

Figure 6.2: Two-particle correlator δ for $\pi^+\pi^+$, $\pi^-\pi^-$ and pp. For the protons $p_t > 600\,\text{MeV/c}$ and for the pions $150 < p_t < 600\,\text{MeV/c}$ are required. The values are substantial especially for the contribution from detector effect (right panel).

The measured correlators for same-charged pairs, i.e. $\pi^+\pi^+$, $\pi^-\pi^-$ and pp correlations are shown in figure 6.1 and 6.2. In the left panel the measured signal, i.e. γ and δ is displayed while in the right panel the contribution due to detector effects is shown through the correlators γ^* and δ^* respectively.
First of all the γ correlator shows a clear rise towards peripheral collisions while it approaches zero in the most central events. For the protons having the largest statistic the enhancement is significant since the statistical error bars are small compared to the absolute value of the signal. In the shape of the distribution there are small jumps, this is due to the fact that the efficiency correction is available in 10 % centrality bins of the centrality while the measured signal is displayed for each centrality percentile. For the pions the correlators have been rebinned to centrality classes of 5 % bin width. The enhancement for the negative pions is stronger and seem to follow the trend from the protons. For the positive pions the signal is a bit flattened in the peripheral bins but the statistical error are large.
In the right panel the correlator γ^* is displayed and is consistent with zero. Hence, the contribution to the signal due to detector effects is negligible. For the most peripheral bins in the $\pi^+\pi^+$ correlation there could be some impact from detector effects which could explain the flattening of the signal in this region.
Considering the correlator δ the situation changes. The correlator does not seem to converge to zero, there even seem to be an enhancement for the most central bins for the pions (which is in contrast to any expectations). Only in case of the protons the shape shows the expected behavior, while the offset from zero could be explained by the background contribution not related to the reaction plane. This is the same for the correlator δ^*. This observable seems to have an offset of a value ~ -0.27 and then rises for the most central events in case of pp and $\pi^+\pi^+$. The non-zero results for δ^* suggest that the signal for δ is strongly biased by detector effects. It has to be checked where this enhancement comes from. Additional contributions could originate from in- and out-of-plane background and from detector effects when coupled with flow.

Also interesting is to look to the proton-pion correlations, especially in case of the opposite-charged correlations, i.e. $\pi^- p$ and $\pi^- \pi^+$. The correlators are displayed in figure 6.3 and 6.4. For $p_t > 600\,\text{MeV/c}$ the $\pi^+\pi^-$ corralation is not shown since the statistics is to low leading to large statistical errors.

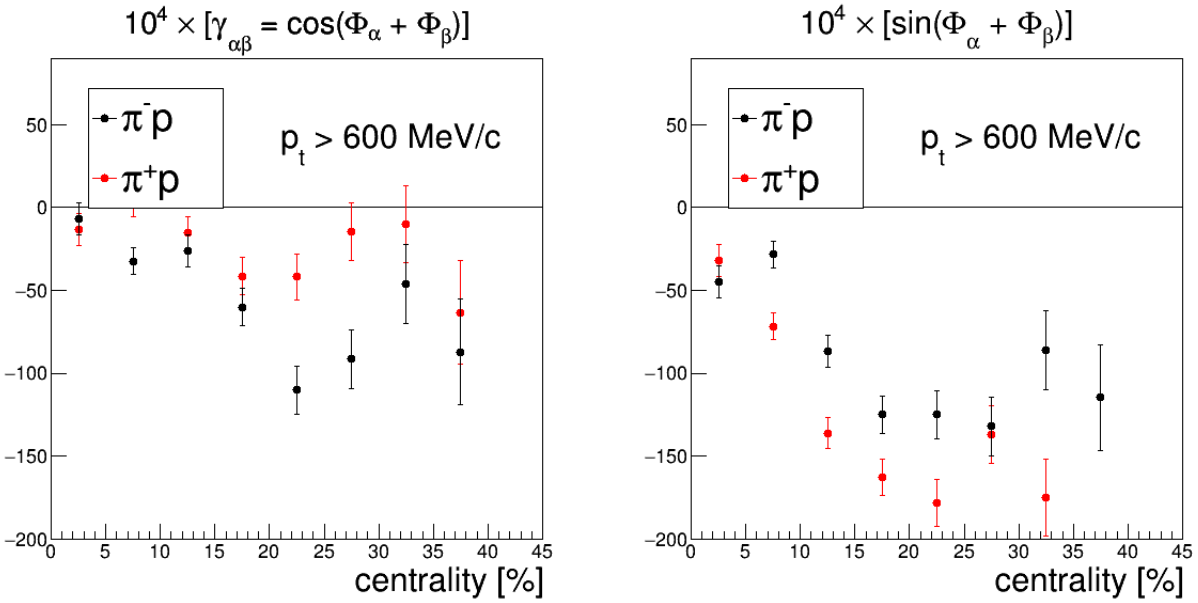

Figure 6.3: Two-particle correlator γ (left panel) and γ^* (right panel) for $\pi^+ p$ and $\pi^- p$ in the range of $p_t > 600\,\text{MeV/c}$. The values are very large especially for the contribution from detector effect (right panel).

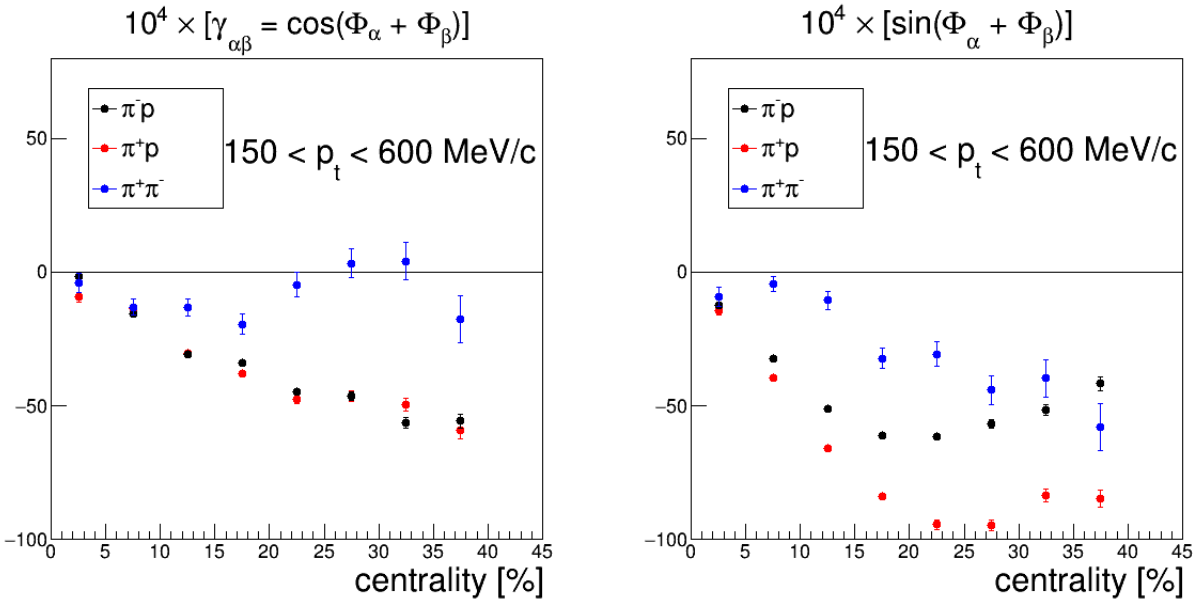

Figure 6.4: Two-particle correlator γ (left panel) and γ^* (right panel) for $\pi^+ p$, $\pi^- p$ and $\pi^+\pi^-$ in the range of $150 < p_t < 600\,\text{MeV/c}$. The values are very large especially for the contribution from detector effect (right panel).

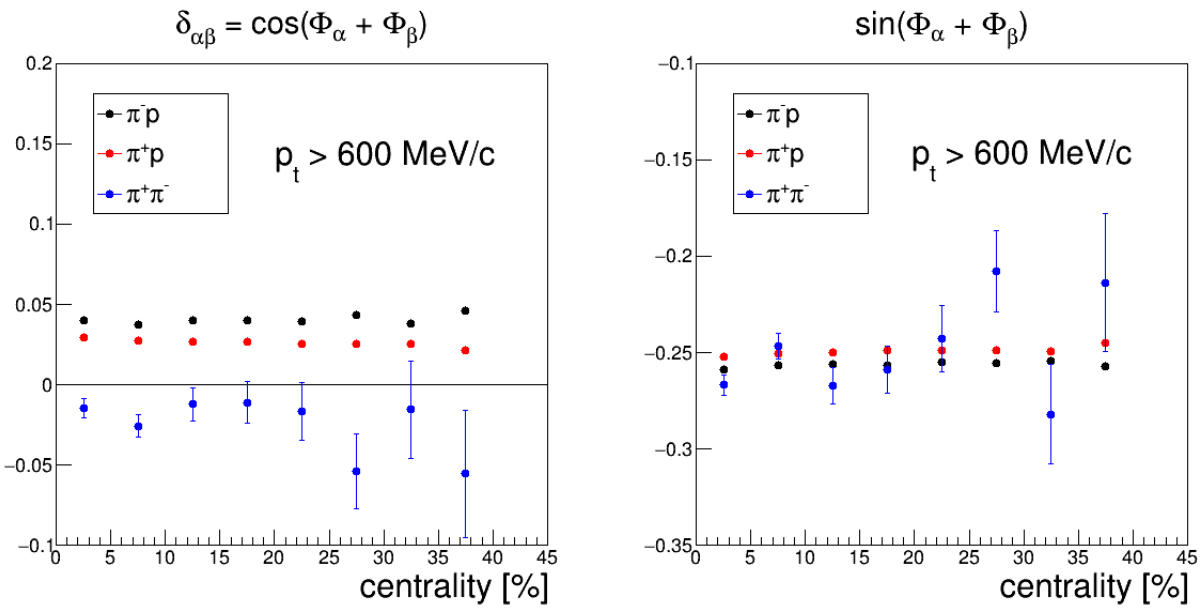

Figure 6.5: Two-particle correlator γ (left panel) and γ^* (right panel) for π^+p, π^-p and $\pi^+\pi^-$ in the range of $p_t > 600$ MeV/c. The values are very large especially for the contribution from detector effect (right panel).

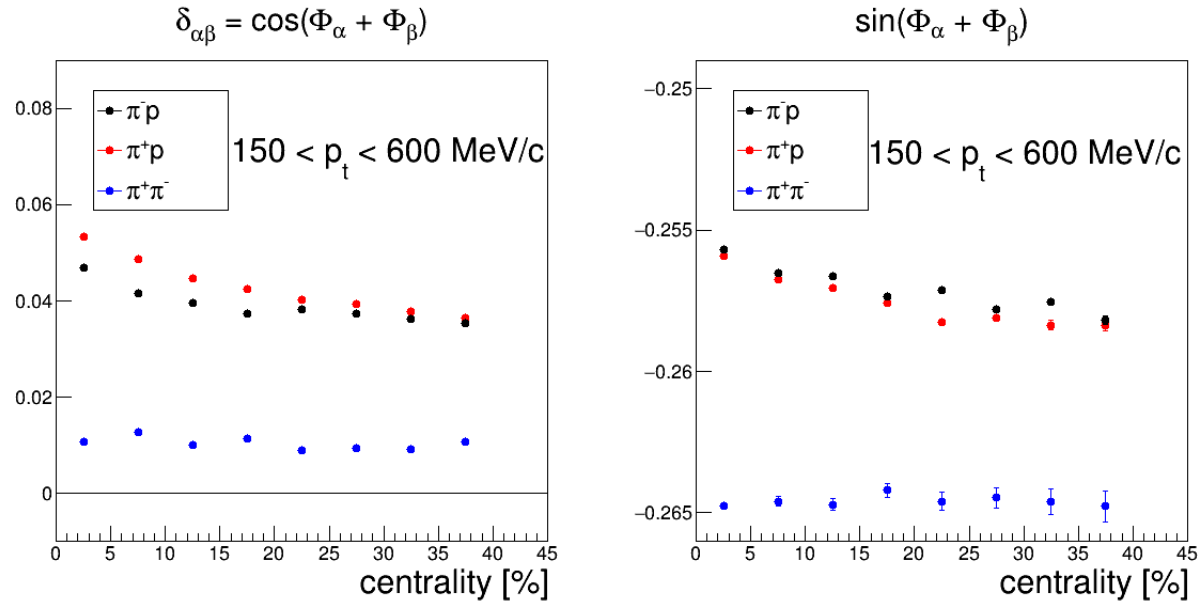

Figure 6.6: Two-particle correlator δ (left panel) and δ^* (right panel) for π^+p, π^-p and $pi^+\pi^-$ in the range of $150 < p_t < 600$ MeV/c. The values are very large especially for the contribution from detector effect (right panel).

In both cases the contribution is at least of the same order as the measured signal also showing an enhancement towards peripheral collisions. For $p_t > 600$ MeV/c the pion statistics is to low to conclude something from the measured signal but the background due to detector effects or even the pion flow is significant in this region. In the lower p_t range statistics is much higher. The proton-pion correlator γ has the expected shape but for both cases the measured signal is nearly the same. This is not predicted by the CME since for opposite-charged pairs the

signal should be lowered due to the interactions with the medium. Yet looking to the impact of detector effects, the contribution seems even to be larger for the same-charged pairs compared to the opposite ones. Nevertheless, further analysis of detector induced correlations is needed to disantangle the origin of this contributions.
The results for the δ and δ^* correlator are displayed in figure 6.5 for $p_t > 600\,\text{MeV/c}$ and 6.6 for $150 < p_t < 600\,\text{MeV/c}$. Interesting is that the sign for both proton-pion correlations δ has changed compared to figure 6.2 while the contribution from detector effects stays the same, $\delta^* \sim -0.027$. There is a centrality dependence for the most central bins in δ^* but compared to the absolute scale this dependence is rather small. Whatever is the origin of this contribution is more or less the same for all measured correlators δ. Remarkably is the fact that the correlator δ does not seem to have a strong centrality dependence, for most of the correlations it is practicaly flat.
To study possible background contributions the mixed-event (ME) method has been used (see figure 6.7 and 6.8). The idea behind is to correlate particles from different events which by definition cannot have a physical correlation. Hence, if the results are non-zero this would point to systematics arising from detector effects. Thus this method can be used to estimate the background contribution. Note that the results from the ME technique are also corrected for event plane resolution and efficiency according to their centrality percentile.
First of all the calculated correlators γ_{ME} and γ^*_{ME} show a comparable behavior (see figure 6.7) and are both consistent with zero. This is a good sign since the measured signal can not be explained by pure background (this is also true for the correlator δ_{ME}). Also the correlator δ_{ME} is close to zero and can not explain the measured same event result. This point to the fact that there could be some correlated detector effects which creates the significant values.

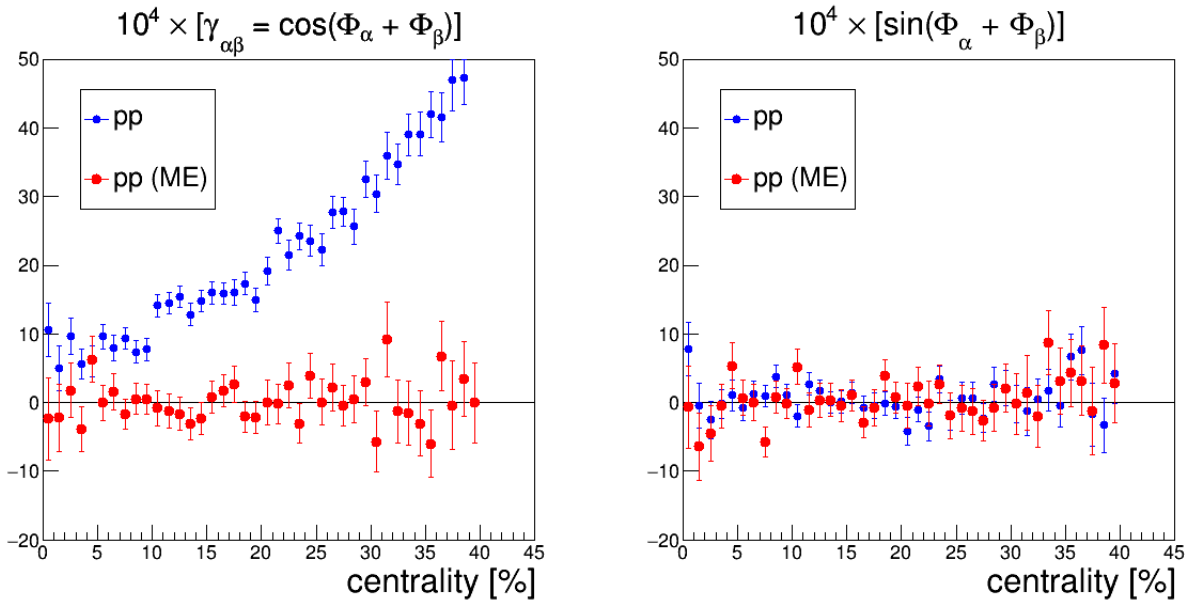

Figure 6.7: Proton-proton correlators γ (left panel) and γ^* (right panel) as a function of the centrality for $p_t > 600\,\text{MeV/c}$. Red circles: the results obtained from the mixed-event technique.

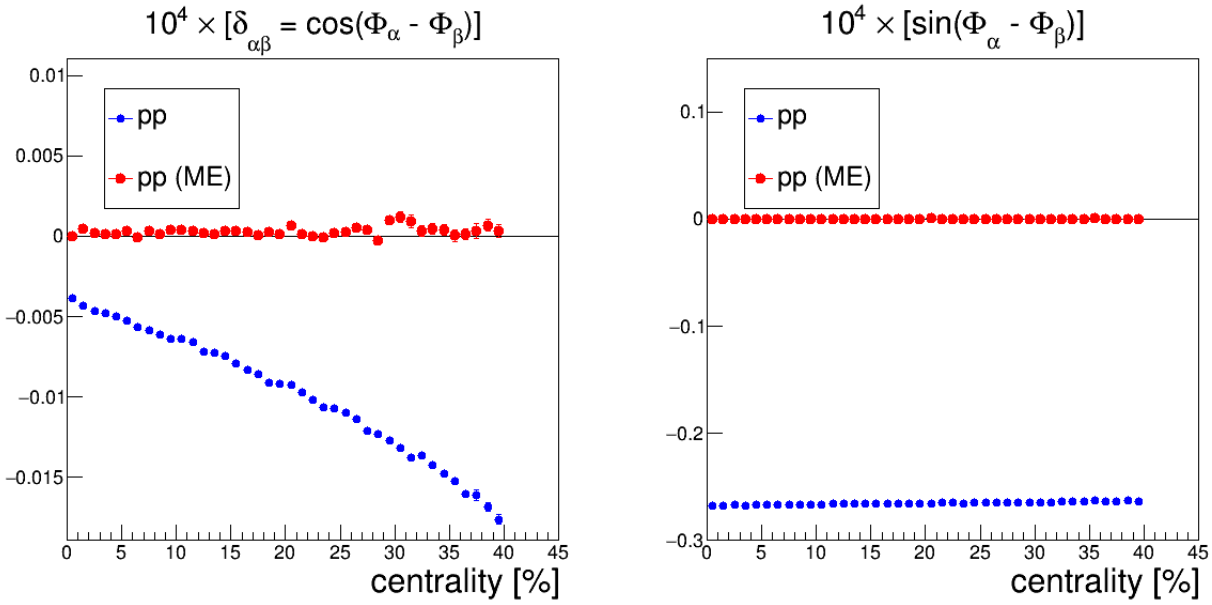

Figure 6.8: Proton-proton correlators δ (left panel) and δ^* (right panel) as a function of the centrality for $p_t > 600$ MeV/c. Red circles: the results obtained from the mixed-event technique.

As a last step the correlators have also been calculated from Monte-Carlo simulations. The comparison is displayed in figure 6.9 and 6.10. It is calculated using the ideal values but also the reconstructed ones. For the ideal values this means that the track reconstruction and particle identification is done as described below but than for a reconstructed particles the input values from the simulation (Geant Kine) are asked in addition. The realistic particle identification is used together with the realistic ϕ angle and the true reaction plane angle. Additionally, only primary particles are considered. For the values reconstructed from the simulations it is not asked explicitely for primaries so these results can be directly compared to the data. To do so, they are also corrected by efficiency and event plane resolution.
From figure 6.9 one can clearly see that the contribution from detector effects is small, comparable with zero. The simulated signal itself shows also an enhancement towards peripheral events but not as strong as observed in the experimental data. UrQMD does not include any CME or CVE hence if at least one of these effect is measured for sure it will not appear in the simulations. Another reason for the stronger rise in the data could be due to regeneration of resonances.
In figure 6.10 the simulated correlator δ^* shows no centrality dependence but a clear offset of the same order as in the experimental data ($\delta^* \sim -0.27$). This further points to the strong contribution from the correlated detector effects. For the correlator δ both results from simulation basically overlay. Comparing with the data the shape seems to be the same while the difference in magnitude could be due to the difference in the correlator δ^*.

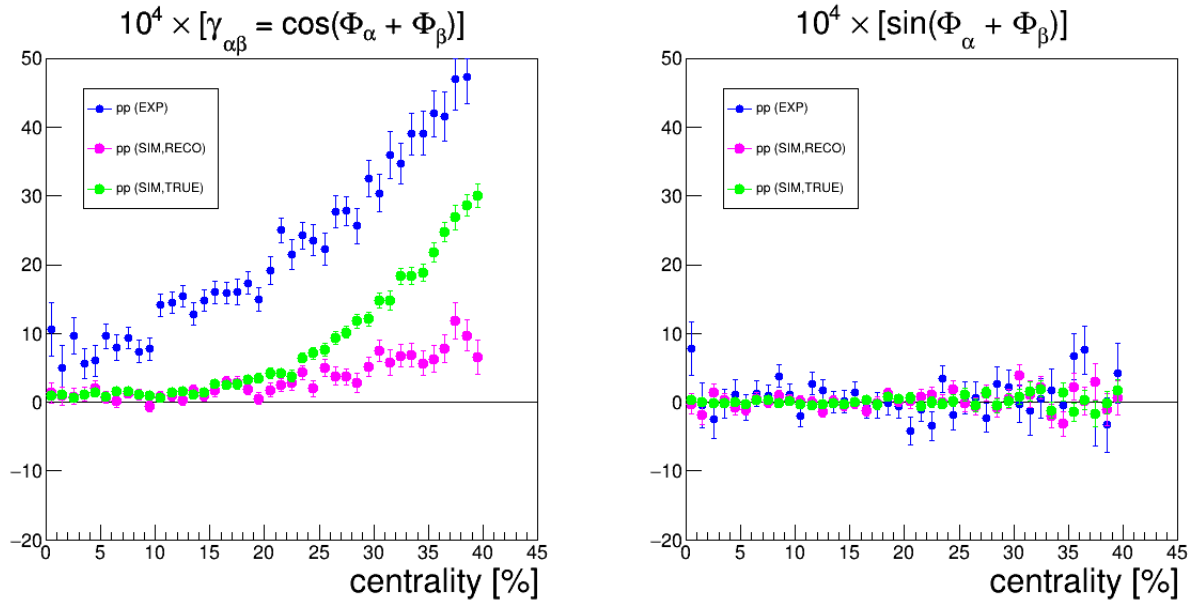

Figure 6.9: Proton-proton correlators γ (left panel) and γ^* (right panel) as a function of the centrality for $p_t > 600\,\text{MeV/c}$ (blue circles) compared to the UrQMD simulation (magenta and green circles). The simulated correlator are calculated using the true values (green circles) and the reconstructed ones (magenta circles) both for reconstructed particles only.

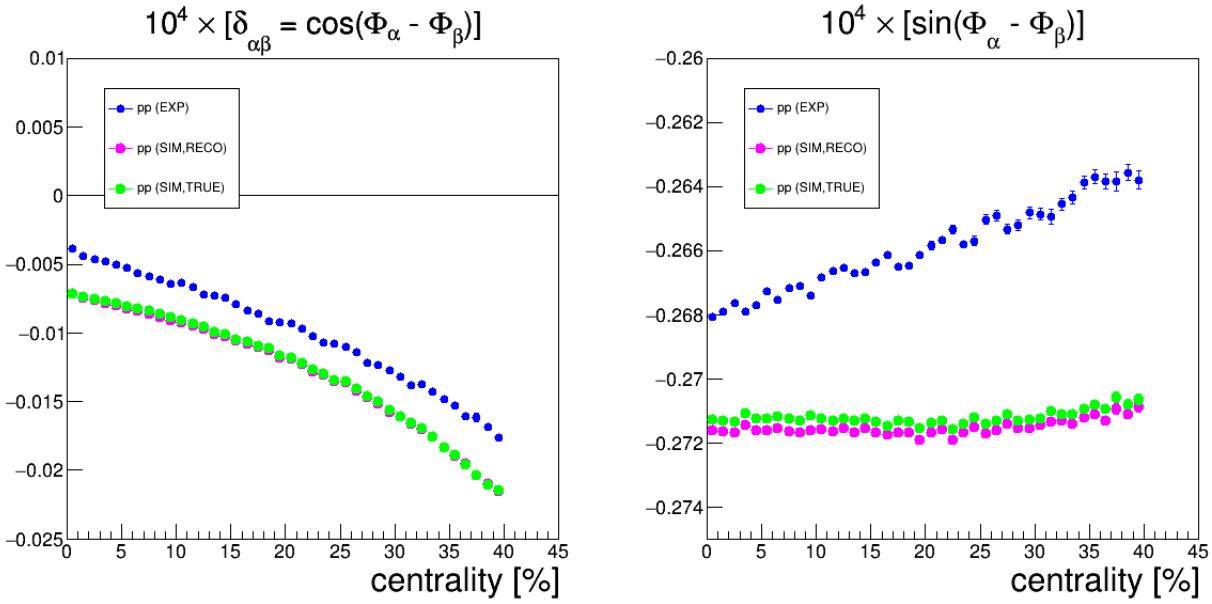

Figure 6.10: Proton-proton correlators δ (left panel) and δ^* (right panel) as a function of the centrality for $p_t > 600\,\text{MeV/c}$ (blue circles) compared to the UrQMD simulation (magenta and green circles). The simulated correlator are calculated using the true values (green cirlces) and the reconstructed ones (magenta circles) both for reconstructed particles only.

7 Conclusions and outlook

The Au+Au collisions at a center-of-mass energy of $\sqrt{s_{NN}} = 2.42\,\text{GeV}$ taken in april 2012 with HADES have been analyzed concerning two-particle correlations. The correlators $\gamma_{\alpha\beta} = \langle\cos(\Phi_\alpha + \Phi_\beta)\rangle$ and $\delta_{\alpha\beta} = \langle\cos(\Phi_\alpha - \Phi_\beta)\rangle$ are calculated for all combinations of protons and charged pions as a function of the centrality. The results are corrected for event plane resolution as well as for the efficiency losses due to the local high track densities.
For the proton-proton correlation the correlator γ showed a clear enhancement towards the peripheral events which could not be described neither by detector effects nor by Monte-Carlo simulations based on UrQMD. Also the mixed-event method cannot reproduce the excess in γ. The results have been taken in a transverse momentum region of $p_t > 600\,\text{MeV/c}$ where the flow contribution is small. The comparison of the HADES results to the one obtained by the STAR collaboration in the beam energy scan phase 1 are shown in figure 7.1. The enhancement of γ in the HADES data is much stronger. This could be due to a number of reasons, in particular physical background rising up for lower energies, also the HADES analysis is done for different kinematics cuts (both p_t and y) than the STAR analysis. Note, also the STAR BES results showed more prominent enhancement towards lower beam energies. Additional contributions to the HADES data could come from resonances.

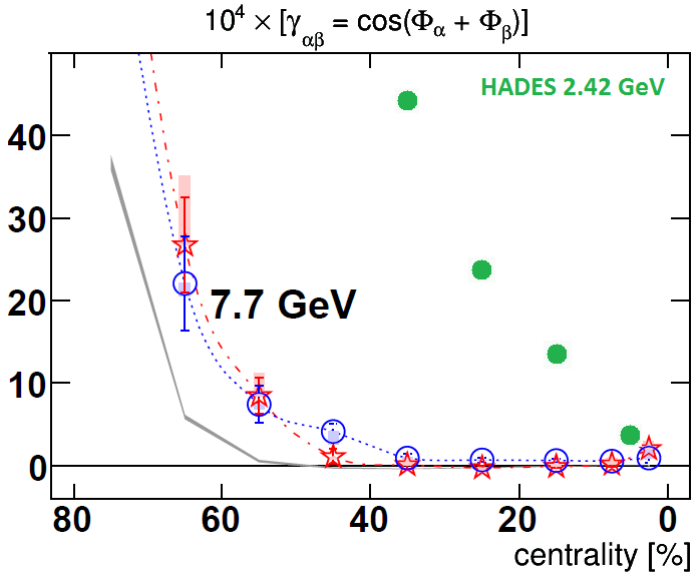

Figure 7.1: Comparison of the recent results of the correlator γ_{pp} measured in Au+Au collisions with $\sqrt{s_{NN}} = 2.42\,\text{GeV}$ by the HADES spectrometer (green circles) to the data of the lowest energy of $\sqrt{s_{NN}} = 7.7\,\text{GeV}$ from the STAR BES [40]. Only statistical errors are ploted for the HADES points. Red stars: same charged pairs. Blue open circles: opposite charged pairs.

For other particle correlations, like proton-pion, the contribution from detector effects is significant, while the shape is different for different particle correlations. This has to be checked in more details.
Again, for some of the correlations there is an enhancement for the most central collisions. In

the Monte-Carlo simulation using the UrQMD model this enhancement is not seen. Moreover, for the correlator δ which is strongly affected by background contributions there is a large offset to about $\delta \sim -0.27$ but without any centrality dependence (present in both simulated and experimental data).
The measured signal in proton-proton correlations calls for further analysis to identify the origin of its centrality dependence. Since at HADES energies a QGP is not expected to occur a large contribution from the chiral magnetic effect is questionable. However, in peripheral collisions the total angular momentum is large and could lead to a spin alignment of vector mesons and hyperons. Coupled to the underlying topology of the QCD vacuum this could also results in a charge separation perpendicular to the reaction plane known as the chiral vortical effect [42]. Therefore, it will be very interesting to study the particle polarization especially for the Λ hyperon.

Bibliography

[1] https://home.cern/about/physics/standard-model 12/2016.

[2] http://www.scinexx.de/wissen-aktuell-20528-2016-08-22.html 01/2017.

[3] ATLAS collaboration, G. Aad et al., "Observation of a new particle in the search for the standard model Higgs boson with the ATLAS detector at the LHC", Phys.Lett. B712 (2012) 1-29, arXiv:1207.7214 [hep-ex].

[4] CMS collaboration, S. Chatrchyan et al., "Observation of a new boson at a mass of 125 GeV with the CMS experiment at the LHC", Phys.Lett. B716 (2012) 30-61, arXiv:1207.7235 [hep-ex].

[5] B. Povh, K. Rith, C. Scholz, F. Zetsche, W. Rodejohann, Teilchen und Kerne - Eine Einführung in die physikalischen Konzepte, Springer Verlag, 9. Auflage (2014).

[6] HADES collaboration, T. Galatyuk et al., "HADES overview", Nucl.Phys. A931 (2014) 41-51.

[7] A. Adams et al., "Strongly correlated quantum fluids", N. J. Phys. 14 (2012).

[8] Review of particle physics, Particle Data Group, Chin. Phys. C38 (2014).

[9] P. Braun-Munzinger et al., "The phase diagram of strongly-interacting matter", Rev.Mod.Phys. 81 (2009) 1031-1050, arXiv:0801.4256 [hep-ph].

[10] Y. Aoki, Z. Fodor, S. D. Katz and K. K. Szabo, "The QCD transition temperature: results with physical masses in the continuum limit", JHEP06(2009)088, arXiv:hep-lat/0609068.

[11] M. A. Stephanov, "QCD phase diagram and the critical point", Prog.Theor.Phys.Suppl. 153 (2004) 139-156, Int.J.Mod.Phys. A20 (2005) 4387-4392, arXiv:hep-ph/0402115.

[12] L. McLerran, "Quarkyonic matter and the QCD phase diagram", (2008) arXiv:0808.1057[hep-ph].

[13] R. J. Glauber, W. E. Britten et al. (eds.), High-enery collision theory, in Lectures in Theoretical Physics, Vol.1 (Inter-Sciene, New York, 1959), pp. 315-414.

[14] B. Kardan, "Centrality determination at 1.23 AGeV Gold-Gold collisionsand readout-electronics for the HADES electromagnetic calorimeter", Goethe University Frankfurt, Diploma 2015.

[15] C. Hartnack, H. Oeschler and J. Aichelin, "What determines the K multiplicity at energies around 1 AGeV-2 AGeV", Phys.Rev.Lett. 90:102302 (2003).

[16] S. A. Bass et al., "Microscopic Models for Ultrarelativistic Heavy Ion Collisions", Prog.Part.Nucl.Phys. 41 (1998) 225-370, arXiv:nucl-th/9803035.

[17] M. Bleicher et al., "Relativistic Hadron-Hadron Collisions in the Ultra-Relativistic Quantum Molecular Dynamics Model", J.Phys.G:Nucl.Part.Phys. 25 (1999) 1859-1896.

[18] https://urqmd.org/ 12/2016.

[19] V. Skokov, A. Illarionov and V. D. Toneev, "Estimate of the magnetic field strength in heavy ion collisions", Int. J. Mod. Phys. A24 (2009) 5925-5932, arXiv:0907.1396 [nucl-th].

[20] V. Skokov, "Magnetic field effect on photon production", Western Michigan University, 2014.

[21] D. Kharzeev, R. D. Pisarski and M. H. G. Tytgat, "Possibility of spontaneous parity violation in hot QCD", Phys. Rev. Lett. 81, 512 (1998), arXiv:hep-ph/9804221.

[22] G. t'Hooft, F. Bruckmann, "Monopoles, Instantons and Confinement", arXiv:hep-th/0010225.

[23] D. Kharzeev, L. McLerran and H. Warringa, "The effects of topological charge change in heavy ion collisions: 'Event by event *P* and *CP* violation", Nucl.Phys. A803, 227 (2008), arXiv:0711.0950.

[24] A. Bzdak, V. Koch and J. Liao, "Charge-Dependent Correlations in Relativistic Heavy Ion Collisions and the Chiral Magnetic Effect", Lect. Notes Phys. 871 (2013) 503-536, arXiv:1207.7327 [nucl-th].

[25] N. Borghini et al., "A new method for measuring azimuthal distributions in nucleus-nucleus collisions", Phys.Rev. C63 (2001), arXiv:054906 [nucl-th].

[26] D. E. Kharzeev, "The chiral magnetic effect and anomaly-induced transport", PNP 75 (2014) 133-151.

[27] STAR collaboration, I. Selyuzhenkov et al., "Azimuthal charge particle correlations as a probe for local strong parity violation in heavy-ion collisions", arXiv:0910.0464 [nucl-ex].

[28] S. Voloshin and Y. Zhang, "Flow Study in Relativistic Nuclear Collisions by Fourier Expansion of Azimuthal Particle Distributions", Z. Phys. C 70 (1996) 665, arXiv:hep-ph/9407282.

[29] S. Voloshin, "Parity violation in hot QCD: how to detect it", Phys.Rev. C 70, 057901 (2004), arXiv:hep-ph/0406311.

[30] A. Bzdak, V. Koch and J. Liao, "Remarks on possible local parity violation in heavy ion collisions", Phys. Rev. C81 (2010) 031901, arXiv:0912.5050 [nucl-th].

[31] http://aliceinfo.cern.ch/Public/Welcome.html 02/2017.

[32] https://www.star.bnl.gov/ 02/2017.

[33] STAR collaboration, B. I. Abelev et al., "Azimuthal charged-particle correlations and possible local strong paritiy violation", Phys.Rev.Lett. 103 (2009) 251601, arXiv:0909.1739 [nucl-ex].

[34] STAR collaboration, B. I. Abelev et al., "Observation of charge-dependent azimuthal correlations and possible local strong parity violation in heavy-ion collisions", Phys.Rev. C81 (2010) 054908, arXiv:0909.1717 [nucl-ex].

[35] STAR collaboration, J. Adams et al., "Azimuthal anisotropy in Au+Au collisions at $\sqrt{s_{NN}} = 200\,\text{GeV}$", Phys.Rev. C72 (2005) 014904.

[36] F. Wang, "Effects of cluster particle correlations on local parity violation observables", Phys.Rev. C81 (2010) 064902, arXiv:0911.1482 [nucl-ex].

[37] S. Schlichting and S. Pratt, "Charge conservation at energies available at the BNL Relativistic Heavy Ion Collider and contributions to local parity violation observables", Phys.Rev. C83 (2011) 014913, arXiv:1009.4283 [nucl-th].

[38] ALICE collaboration, B. Abelev et al., "Charge separation relative to the reaction plane in Pb-Pb collisions at $\sqrt{s_{NN}} = 2.76\,\text{TeV}$", Phys.Rev.Lett. 110 (2013) 012301, arXiv:1207.0900 [nucl-ex].

[39] J. Onderwaater for the ALICE collaboration, "Charge dependence of identified two-hadron correlation relative to the reaction plane in Pb-Pb collisions measured with ALICE", J.Phys.Conf.Ser. 612 (2015) no.1, 012044.

[40] STAR collaboration, L. Adamczyk et al., "Beam-energy dependence of charge separation along the magnetic field in Au+Au collisions at RHIC", Phys. Rev. Lett. 113 (2014) 052302, arXiv:1404.1433 [nucl-ex].

[41] STAR collaboration, L. Adamczyk et al., "Fluctuations of charge separation perpendicular to the event plane and local parity violation in $\sqrt{s_{NN}} = 200\,\text{GeV}$ Au+Au collisions at the BNL Relativistic Heavy Ion Collider", Phys.Rev. C88 (2013) no6., 064911, arXiv:1302.3802.

[42] D. E. Kharzeev et al., "Chiral magnetic and vortical effects in high-energy nuclear collisions - A status report", Prog.Part.Nucl.Phys. 88 (2016) 1-28, arXiv:1511.04050 [hep-ph].

[43] HADES collaboration, G. Agakishiev et al., "The High-Acceptance Dielectron Spectrometer HADES", Eur.Phys.J. A41 (2009) 243-277, arXiv:0902.3478[nucl-ex].

[44] P. Salabura et al., "HADES: A High Acceptance DiElectron Spectrometer", Nucl.Phys.Proc.Suppl. 44 (1995) 701-707.

[45] HADES collaboration, J. Pietraszko et al., "Diamonds as timing detectors for minimum-ionizing particles: The HADES proton-beam mmonitor and START signal detectors for time of flight measurements", Nucl.Instrum.Meth. A618 1-3 (2010), arXiv:0911.0337 [nucl.ex].

[46] J. Pietraszko, "Beam detectors in Au+Au run and future developments", https://indico.gsi.de/materialDisplay.py?contribId=9&sessionId=4&materialId=slides&confId=2142 (2013).

[47] T. Ypsilantis et al., "Theory of ring imaging Cherenkov counters", Nucl.Instrum.Meth. A343 (1994) 30-51 LPC-93-45.

[48] K. Zeitelhack, "The HADES RICH detector", Nucl.Instrum.Meth. A433 201-206 (1999).

[49] H. Bokemeyer et al., "Development of low-mass drift chambers for the HADES spectrometer", Nucl.Instrum.Meth. A477 (2002), 397-400.

[50] C. Agodi et al., "The HADES time-of-flight wall", Nucl.Instrum.Meth. A492 (2002) 14-25.

[51] D. Belver et al., "The HADES RPC inner TOF wall", Nucl.Instrum.Meth. A602 (2009) 687-690.

[52] A. Balanda et al., "The HADES Pre-Shower detector", Nucl.Instrum.Meth. A531 (2004) 445-458.

[53] https://hades.gsi.de/?q=node/55 04/2017.

[54] Birgit Kindler et al., "Targets for the electron-positron pair spectrometer HADES", Nucl.Instrum.Meth. A655 (2011) 95-99.

[55] J. Michel et al., "The HADES DAQ system: Trigger and readout board network", Trans.Nucl.Sci. 58 (2011) 1745-1750.

[56] A. M. Poskanzer and S. A. Voloshin, "Methods for analyzing anisotropic flow in relativistic nuclear collisions", Phys.Rev. C58, 1671 (1998), arXiv:nucl-ex/9805001.

[57] http://web-docs.gsi.de/~halo/docs/hydra/classDocumentation/dev/ 03/2017.

[58] https://root.cern.ch 03/2017.

[59] http://consult.cern.ch/writeup/geant 03/2017.

[60] J. Markert, HADES internal report, https://hades-wiki.gsi.de/foswiki/bin/view/SimAna/HadesLLDAAPionOnline 04/2017.

[61] K. Olive et al., "Review of particle physics", Chin.Phys. C38:090001, 2014.

[62] HADES collaboration, G. Kornakov et al., "Time-of-flight measurement in heavy-ion collisions with the HADES RPC TOF wall", JINST 9 (2014) no. 11, C11015.

[63] J.-Y. Ollitrault, "Reconstructing azimuthal distributions in nucleus-nucleus collisions", arXiv:nucl-ex/9711003.

[64] J.-Y. Ollitrault, "Flow systematics from SIS to SPS energies", Nucl.Phys. A638, 195 (1998), arXiv:nucl-ex/9802005.

[65] P. Tlusty, M. Gumberidze, https://indico.gsi.de/getFile.py/acces?contribId=1&resId=0&materialId=slides&confId=5389 04/2017.